MSc Thesis

An experimental and numerical investigation of the aerodynamic characteristics of a flameless combustor

M. P. Huijts

Technische Universiteit Delft

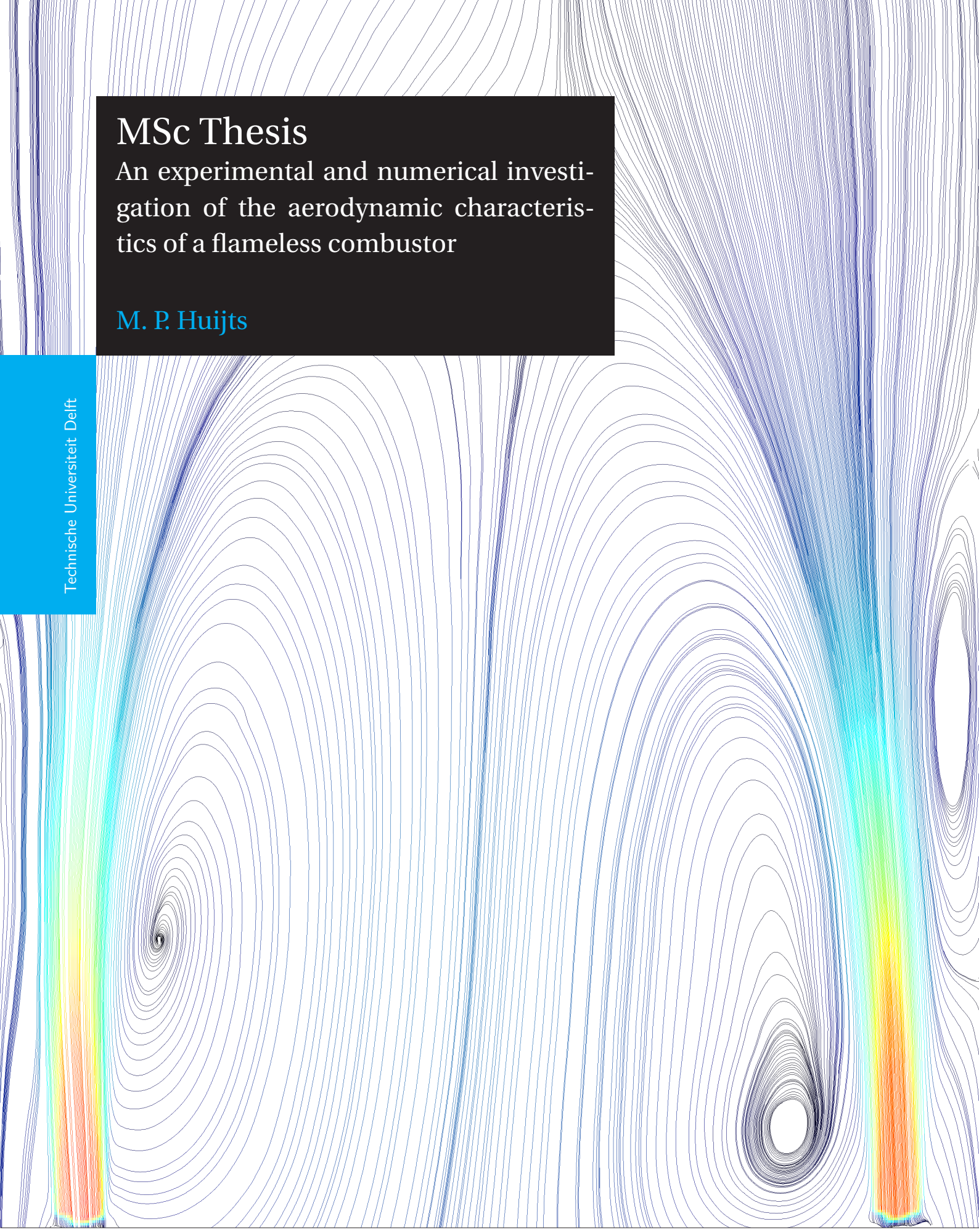

TU Delft Delft University of Technology

Challenge the future

MSc Thesis

An experimental and numerical investigation of the aerodynamic characteristics of a flameless combustor

by

M. P. Huijts

in partial fulfillment of the requirements for the degree of

Master of Science
in Aerospace Engineering

at the Delft University of Technology,
to be defended publicly on Thursday May 24, 2018 at 14:00.

Student number: 4118197

Supervisor:	Dr. A. Gangoli Rao,	
Thesis committee:	Dr. ir. G. A. Bohlin,	TU Delft
	Dr. A. Gangoli Rao (Chairman),	TU Delft
	A. A. V. Perpignan, MSc	TU Delft
	Dr. ir. F. F. J. Schrijer,	TU Delft

This thesis is confidential and cannot be made public until September 1, 2019.

TU Delft Delft University of Technology

ACKNOWLEDGEMENTS

My student time in Delft has proven to be very rich, teaching me a lot about the world and people around me, but mostly about myself. Also this MSc Thesis project has put myself in new situations, challenging me in ways I didn't know yet were possible. Much of the work you have to do yourself, but having others around you proves to be invaluable to flourish and accomplish what you want. For this reason I would like to thank a few individuals and groups that have brought this MSc Thesis to what it is right now.

Being able to perform experimental research on a combustion setup like the one in the Propulsion Lab is an amazing opportunity and has been a great experience. I wish to thank my supervisor Dr. Arvind Gangoli Rao for giving me this. Next to this, your positive and relaxed attitude have made working with you a pleasure and I am thankful that you accepted to supervise me on this journey. This thesis work also would not have been possible without the supervision of André Perpginan. I want to thank you for your input in all the meetings and your willingness to help and guide me was truly key in completing the thesis. I could stop by anytime for any question, which really helped in keeping my flow.

During the experimental PIV campaign and while processing the results I have had much help from Dr.ir. Ferry Schrijer and Dr. Andrea Sciacchitano. I want to thank you both for your time and effort and the enthusiasm with which you were always ready to help practically and theoretically.

As a student i did not have much practical knowledge about performing experiments. Therefore the commissioning of the setup, practical problem-solving, last-minute fixes and solving struggles with soft- and hardware would not have been possible without the help of Jos, Henk-Jan, Dennis, Peter, Frits and Nico from the High-Speed Laboratory technical staff. A special thanks to Jos for the great times we have had working on the setup and while taking our breaks.

Apart from the academic staff, I have had great support from my peers in the two rooms I have stayed in during this thesis period. I want to thank both 2.44 and NB1.01 for the great walks, fun lunches and rants we have had. Also my housemates have always supported me and I want to specifically thank Floris for his input on this report.

Last, but certainly not least, I want to thank both my parents and my brothers for their support in everything I do. Thank you to my parents for giving me all the opportunities I have had and creating a safe haven in times of need. Thank you to my brothers for always being there and for all the discussions in which you are always ready to share your experiences and unparalleled wisdom.

Thank you all,

M. P. Huijts
Delft, May 2018

SUMMARY

NO_x is a group of emissions originating from combustion systems using atmospheric air. These emissions affect human health, vegetation and buildings, and the chemical composition of the tropo- and stratosphere. NO_x is formed via many chemical mechanisms, where the thermal NO_x pathway is the main contributor to its emissions. The impact of NO_x emissions only becomes greater with time, because of the continuous growth expected for the aviation industry. Stringent regulations are set to decrease these emissions from aviation. Due to strict and though engineering requirements for aero engines, only few NO_x reducing solutions will be suited to meet these regulations. One promising solution is operation in a combustion regime called flameless combustion.

Operation in the flameless combustion regime requires a low oxygen concentration and high reactant temperature. Key in this is the recirculation of hot flue gases, mixing with and diluting the reactants. Low oxygen availability and a decrease in temperature peaks reduces NO_x production. The aim of this thesis is quantifying the recirculation zones and their recirculating rates and the influence of variables on them for a FLOX® design. These variables are the combustion chamber length, the nozzle diameter and the jet velocity.

The aerodynamics have been investigated experimentally using planar Particle Imaging Velocimetry and numerically using Reynolds-averaged Navier-Stokes models. One major modification made to the setup is interchanging the steel combustion chamber by an acrylic transparent one to provide a full view of the flow field. Two different plane locations have been used in the experimental analysis, allowing to see both the primary and secondary flow structures.

The research has shown that changing the combustion chamber length does not influence the flow structure if it does not interfere directly with the recirculation zone. Changing the jet velocity also does not change the flow structure for a constant nozzle diameter. The jet momentum is seen to influence the recirculation behaviour the most. Increased jet momentum increases the reynolds shear stresses, increasing the momentum exchange perpendicular to and parallel to the jet. This increases entrainment, leading to more recirculation. As such, smaller nozzle diameters cause an increase entrainment and the recirculation of the flue gases, for equal inlet mass flows. Comparison with the numerical results has shown that the peripheral recirculation zone contributes for almost 30% to the recirculation of gases and should not be neglected. However, this zone is hard to quantify experimentally due to optical distortion along the sides of a transparent cylinder.

The numerical analysis has shown that using the approach of Reynolds-average Navier-Stokes models does not yet provide an accurate solution. Specifically the jet outlet conditions need improvement with regards to turbulence levels and velocity profile. Promising results came from the Standard k-ϵ model using c1ϵ = 1.44, with respect to c1ϵ = 1.3 or 1.6. The k-ω SST model did not show improvements over the Standard k-ϵ model. The Realizable k-ϵ model and the Reynolds Stress Model of the k-ϵ model both show worse results than the Standard k-ϵ model, but are thought to be promising with adjustments. The Realizable k-ϵ model could be improved by decreasing the c2ϵ parameter and the Reynolds Stress Model is thought to benefit the most from improved jet outlet conditions.

Previous research and current results on recirculation show that these conditions are sufficient to obtain the flameless combustion regime. From this research it can be concluded that for equal mass flows, smaller nozzle diameters improve the aerodynamics for increasing the range of the flameless combustion regime. This will come at a pressure loss cost though, meaning optima will have to be sought. Designs that open or close nozzles during operation could aid in this, allowing for optimal jet momentum with minimal pressure losses. The numerical Reynolds-averaged Navier-Stokes approach still shows room for improvement and a possibility of accurate modelling. If this succeeds it is perhaps not needed to switch to the Large eddy simulation approach, meaning great savings in computational time.

CONTENTS

List of Figures

LIST OF TABLES

NOMENCLATURE

LIST OF ABBREVIATIONS

AFR	Air-to-Fuel Ratio
CFD	Computational Fluid Dynamics
CRZ	Central Reciruclation Zone
DAQ&C	Data Acquisition & Control
DUT	Delft University of Technology
ER	Entrainment Rate
EWT	Enhanced Wall Treatment
FAR	Fuel-to-Air Ratio
FC	Flameless Combustion
FLOX	Flameless Oxidation
FOV	Field of View
GWP	Global Warming Potential
IWS	Interrogation Window Size
LBO	Lean-Blow-Out
LDI	Lean Direct Injection
LES	Large Eddy Simulation
LPP	Lean Premixed Pre-Vaporized Combustion
MFC	Mass Flow Controller
MN, SN, MSN	Multi Nozzle, Single Nozzle, Multi-Single Nozzle
PIV	Particle Imaging Velocimetry
PLIF	Planar Laser-Induced Fluorescence
PRZ	Peripheral Recirculation Zone
PTV	Particle Tracking Velocimetry
RANS	Reynolds-averaged Navier-Stokes
RMS	Root mean squared
RQL	Rich Burn Quick Quench Lean Burn
RR	Recirculation Ratio
RSS	Reynolds shear stress
RZ	Recirculation Zone
SP	Stagnation Point
SST	Shear-stress Transport
SWF	Standard Wall Function
TDR	Turbulent Dissipation Rate
TI	Turbulence Intensity
TKE	Tubulent Kinetic Energy
UHC	Unburned HydroCarbons
UV-A, -B, -C	Ultraviolet-A, -B, -C radiation

LIST OF SYMBOLS

Latin		**Unit**
a	acceleration	$[m/s^2]$
d	diameter, distance	$[mm]$, $[mm]$
D	aperture, diameter	$[m]$
dl	fuel-jet nozzle distance	$[m]$
f	focal length	$[mm]$
$f\#$	f-stop	$[-]$
g	body acceleration	$[m/s^2]$
k	turbulent kinetic energy, digital image resolution	$[J/kg]$, $[pixels/mm]$
K_v	recirculation rate	$[-]$
L	length	$[m]$
$l*$	normalised window size	$[-]$
L_f	flow length scale	$[mm]$
m	mass	$[kg]$
$\dot{m}$	mass flow	$[kg/s]$
M	magnification factor	$[-]$
n	moles number	$[mole]$
N	ensemble size	$[-]$
P	power, pressure	$[W]$, $[bar]$
p	momentum	$[kg \cdot m/s]$
q	normalised diameter	$[-]$
r	radius	$[mm]$
R	specific gas constant	$[J/(kg \cdot K)]$
Re	Reynolds number	$[-]$
S_k	Stokes number	$[-]$
T	temperature, time between image pairs	$[K]$, $[s]$
$u,\ v,\ w$	x, y, z velocity components	$[m/s]$
U	velocity	$[m/s]$
u'	velocity fluctuation	$[m/s]$
y^+	dimensionless wall distance	$[-]$

Greek		**Unit**
δy_p	half-height of the first mesh cell	$[m]$
δt	time difference	$[s]$
δz	focal depth	$[m]$
ΔU	velocity difference	$[m/s]$
ϵ	turbulent dissipation rate, error	$[J/(kg \cdot s)]$, $[-]$
λ	equivalence ratio (AFR), wavelength	$[-]$, $[m]$
μ	dynamic viscosity	$[kg/(m \cdot s)]$
ρ	density	$[kg/m^3]$
τ	characteristic time, viscous stress tensor, friction force	$[s]$, $[N/m^2]$, N
ϕ	equivalence ratio (FAR)	$[-]$
ω	specific turbulence dissipation rate	$[1/s]$

Subscripts	
f	fluid
i	image
n	number of nodes
o	object
p	particle
rec	recirculation
rms	root-mean-square
st	stoichiometric

1

INTRODUCTION

In this chapter, the reader is introduced to the problem at hand and the research that is proposed. Section 1.1 shows the relevance of the problem and the role of the aviation sector. Section 1.2 briefly points out prior work that has been done on handling the problem. Section 1.3 states the contribution of the current work. Finally, Section 1.4 explains the structure of this report.

1.1. CONTEXT AND RELEVANCE

The issue of air pollution started already during the industrial revolution. Although processes have become cleaner and more efficient since then, the immense scale of modern industry has made the problem more relevant. Specifically, high-temperature processes that involve the combustion of fuels contribute to this. One of the main pollutants is NO_x, a common emission gas that causes acid rain and changes the ozone levels in the atmosphere with harmful consequences. One of the contributors to NO_x emissions are aircraft and the combustion processes in their aero engines. Acid rain effects, ozone level disturbances and the way the aviation sector plays a role in NO_x production shall be highlighted in this section.

1.1.1. EFFECTS OF NO_x

NO_x is a collective noun for two different mono-nitrogen oxide emissions, namely nitric oxide (NO) and nitrogen dioxide (NO_2) [17, 18]. When NO_x comes into contact with water it reacts to nitric acid, acidifying the water and causing acid rain[19]. This is harmful for vegetation, wildlife, the quality of open waters and it also affects our buildings and statues.

Next to this, NO_x is involved in chemical reactions with ozone in the atmosphere in multiple ways. In the troposphere and lower stratosphere it leads to the creation of ozone or *tropospheric ozone*, in the upper stratosphere it depletes *stratospheric ozone* [20, 21]. Tropospheric ozone is formed from UV-A radiation reacting with NO_x in the vicinity of species such as CO and unburned hydrocarbons (UHC's), which are also products of combustion processes. Ozone has a global warming potential (GWP) that increases greatly for higher altitudes (see fig. 1.1) contributing to the anthropogenic global warming problem. The figure shows that the greenhouse effect of ozone is more than 250 times stronger at aircraft cruise altitudes than CO_2. Tropospheric ozone is also a main agent in smog, present in many cities. Smog is a very reactive and aggresive substance that causes eye and lung irritation, respiratory problems and damage to vegetation.

Stratospheric ozone is present in large quantities (up to 11 $\mu mole/m^3$[21]) in the middle part of the stratosphere (see fig. 1.2). In this ozone layer, ozone is broken down under the influence of UV-B and UV-C radiation, as such blocking this harmful radiation from reaching the earth's surface. NO_x acts as a catalyst in this reaction mechanism, increasing its reaction rate [22], decreasing the amount of ozone available to stop this radiation. Due to the atmospheric stability of the stratosphere the effect of any addition of NO_x will be present for many years after [23, 24], increasing its impact.

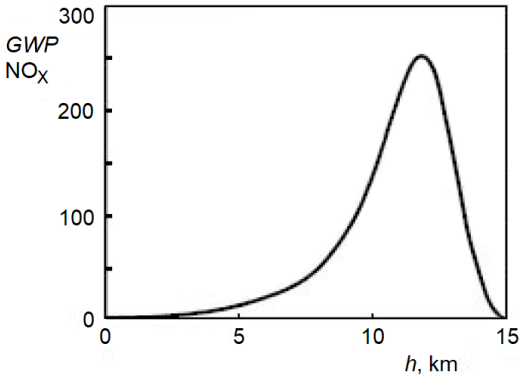

Figure 1.1: GWP of NO_x versus altitude, where the GWP of CO_2 is set as 1. Edited from [1].

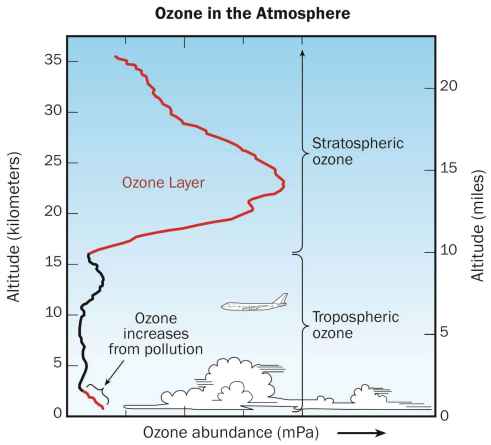

Figure 1.2: Atmospheric ozone abundance versus altitude [2]

It is clear that both in the tropo- and in the stratosphere, NO_x has direct and indirect unwanted effects on global warming, vegetation and human health. It is thus desired to reduce its emissions.

1.1.2. NO_x FROM AVIATION

Aero engines are very restricted to their size and weight, and need to operate in many conditions and power settings. Incorporating new technologies to such engineering marvels is therefore complicated. However, as has been shown in the previous paragraph aero engines should not remain unchanged. The harmful effects of the aviation sector are almost certain to grow in the future. The average annual growth of aviation passenger traffic has been 5.3% between 2000 and 2007, yielding a total 38%. Airbus expects that the aviation market is to grow an annual 4.5% between 2015 and 2035, meaning it will more than double in these 20 years. As such, over 33000 new aircraft will be needed in the next 20 years, which will all need a mode of propulsion [25]. In 2005 it was estimated that the total radiative forcing by aviation was 4.9% of the total anthropogenic radiative forcing. Due to increased NO_x emissions, the radiative forcing of O_3 has increased between 2000 and 2005 with 11.1% and this will continue to increase [17]. Figure 1.3 shows the problematic impact of the emissions on O_3 in 2006. It is evident from this data that NO_x emissions will become an even larger problem in the future if we do not act against it. In order to motivate aero engine manufacturers, the European Union has set up goals via the ACARE Flightpath 2050 project to "decrease NO_x emissions by 90% in 2050, relative to the capabilities of typical new aircraft in 2000.", as is shown in fig. 1.4.

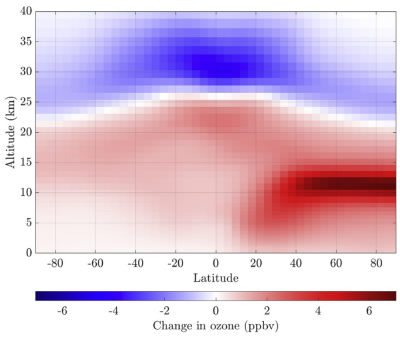

Figure 1.3: Annual average zonal ozone perturbation due to full-flight aviation emissions versus pressure altitude [3]

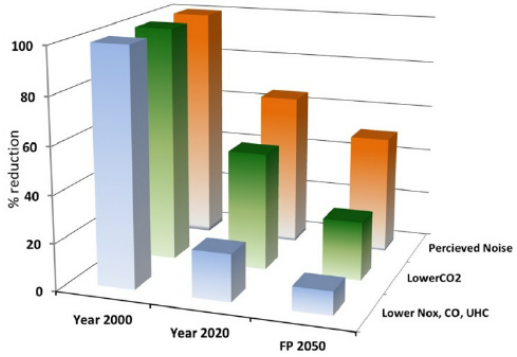

Figure 1.4: The ACARE 2050 flight path for Europe [4]

1.2. PRIOR WORK

One of the main ways to reduce NO_x emissions is by lowering the combustion temperature. This has led to the development of different combustion technologies that operate under low equivalence ratios (ϕ) or in the lean regime. Figure 1.5 shows the different emitted species versus equivalence ratio for a conventional combustor. It can be seen that for $0.25 < \phi < 0.75$ a low emission window exists, where NO_x values decrease for lower values of ϕ. A problem that arises here is that too low values of ϕ cause blow-out[9]. Another way of reducing the NO_x emissions is by lowering the availability of oxygen, it is therefore also tried to recirculate the (inert) combusted or so-called flue gases back to the combustion zone and mix with the fresh fuel-air mixture. This lowers the oxygen concentrations creating a distributed flame zone and also lowers the energy needed to reach the activation energy, reducing chances of blow-out.

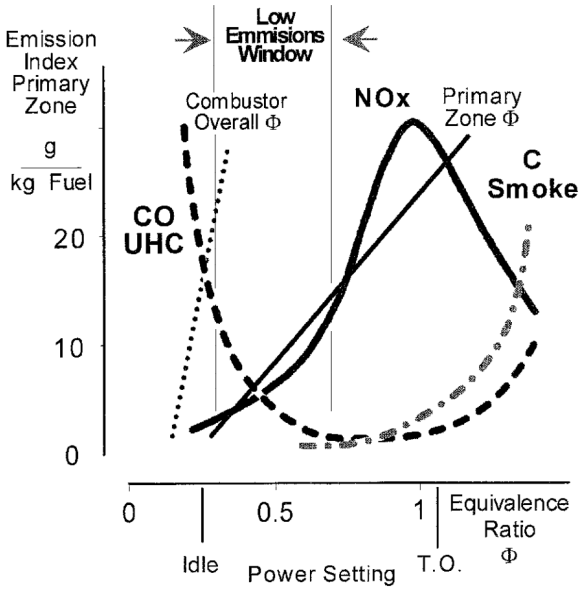

Figure 1.5: Equivalence ratio and power setting versus emitted species in conventional combustion [5]

One combustion regime that combines both ways to reduce NO_x emissions is called **flameless combustion** (FC). In flameless combustion, the reactants are diluted brought to auto-ignition temperature. This is done by using large recirculation regions that supply hot flue gases to the burner zone. Here it mixes with the incoming air and fuel such that a diluted and homogeneous combustion mixture is created. This zone has a low O_2 concentration and high temperatures, minimising NO_x formation while enabling combustion at these lean conditions[26].

Flameless combustion with low NO_x emissions is difficult to establish and maintain in the high heat density environment of gas turbines [27]. As one can see from the explanation of operation in this combusion regime, the mixture should not ignite too early, but also not too late to prevent incomplete combustion [28]. Still, it is a promising reasearch area and its challenges should be investigated. Ways to tackle these disadvantages are establishing strong recirculation zones and ensuring high enough mixing of the recirculating air and incoming air-fuel mixture.

In 2007, Dr. Daniel Cardoso Vaz has obtained his PhD degree by designing, building and performing research on a flameless combustion setup at the Delft University of Technology (DUT) [9]. This setup is now in use by the research section of Flight Performance & Propulsion at this faculty and is stationed in the Propulsion Lab in the High Speed Laboratory. This setup, as well as his already obtained results, have been used in this thesis to further investigate the application of flameless combustion in gas turbines.

1.3. CURRENT CONTRIBUTION

This thesis concentrates on investigating ways to obtain strong recirculation zones and mixing of the recirculated air and the combustion gases. To investigate these properties, the inner aerodynamics of the combustion chamber have been visualised. This has been done experimentally using Particle Imaging Velocimetry (PIV). Planar vector images of the velocity field inside the chamber have been made, showing the recirculation zones, jet development and turbulence characteristics. This has not been done before for a flameless combustor similar to the DUT setup and will therefore present unique findings. Also, since the DUT setup is designed to have flexibility in its geometrical parameters, the impact of these variables on the aerodynamic flows are characterised and quantified.

In addition to this experimental investigation, the aerodynamics of the combustion chamber have been modelled numerically using Computational Fluid Dynamics (CFD). This allows for better comprehension of the PIV data in 3-D and has identified the first main discrepancies between CFD and PIV for this setup. This can later be improved upon until a completely validated CFD model exists of the combustion chamber. Once achieved, quicker and cheaper preliminary experiments can be run using CFD, giving insights that are sometimes hard or expensive to acquire from the real setup.

1.4. REPORT STRUCTURE

The structure of this thesis report is as follows. First, Chapter 2 discusses the details of NO_x production in combustion processes and how to reduce its emissions with different technologies. It is followed by an analysis of the flameless combustion research that has already been performed around the world on different setups. The chapter ends with the knowledge gap present and how this thesis research fills this gap, stating the research question and objectives. Chapter 3 presents the DUT FLOX® setup and how it works and its limitations. Chapters 4 and 5 describe the PIV and CFD methodology, respectively, used by this research to come to answers to the research question. This includes the way the error analysis is performed. Chapter 6 displays the results from the experimental runs, including the quantification of the errors and a verification of results. It is logically followed by Chapter 7 in which these results are analysed and discussed. The thesis report is brought to an end in Chapter 8, where the conclusions are presented, including the assumptions made and the limitations of the research. This chapter also gives recommendations for future research on flameless combustion and the DUT setup.

2

Theoretical Background

This chapter presents the theoretical background behind the thesis. This starts by explaining how NO_x is formed on a chemistry level and then identifies solutions and respective design approaches to reduce these emissions, all in section 2.1. One area of combustion research that is most promising is identified. The experimental research that has been done up to now in this area is summarised in section 2.2. Using this foundation of knowledge and a clear overview of the possibilities and challenges, section 2.3 identifies the research that is needed and defines the research objective and question of this thesis.

2.1. NO_x Reduction

NO_x can be reduced in many ways and some design approaches already exist to achieve this. To understand their working ways, the chemical pathways of NO_x creation are first investigated.

2.1.1. NO_x Formation

Mainly four mechanisms that create NO_x can be identified: Thermal NO_x, fuel-bound NO_x, prompt NO_x and N_2O-intermediate NO_x [9, 29, 30].

Thermal NOX_x

The formation of thermal NO_x is described by the Zeldovich mechanism (see eq. (2.1)), where dissociated oxygen or nitrogen atoms react with nitrogen molecules or oxygen molecules and form NO_x [30]. Nitrogen molecules are abundantly present in any air-breathing processes, because it makes up 78.1% (volume-based) of the atmospheric air [31], making it an emission that is hard to eradicate.

Oxygen starts to dissociate at high temperatures of approximately 1600°C, with an exponential increase of the reaction rates for increasing temperatures. The required residence time to form NO_x changes from seconds for 1600°C to milliseconds for 2000°C [32]. Due to the search for higher (thermal) efficiencies in the thermodynamic cycle of industrial applications, temperatures have been pushed to the region where thermal NO_x production becomes the main source of the emission [18]. For this mechanism the oxygen concentration in the combustion chamber has a larger influence on the NO_x emissions, than the nitrogen concentration. This is due to the oxygen being a more limited source and the reaction rate for fuel oxidation being higher than for the formation of NO_x. Meaning that the available oxygen shall be used more quickly for oxidation of fuel and lowering the concentration of oxygen shall first impact NO_x formation. Furthermore, the dissociation temperature of oxygen is lower than for nitrogen, making it the more dominant reaction for thermal NO_x production around the threshold.

Fuel-bound NOX_x

Some fuels have fuel-bound nitrogen that can react to NO_x when it binds to O-radicals. Thus, even when pure oxygen is used as an oxygen supply to the combustion process instead of air, NO_x emission can arise. Please note that some gaseous fuels do not have fuel-bound nitrogen, but have pure nitrogen as an impurity (such as Dutch natural gas), also giving NO_x emissions [9].

PROMPT NOX_x

Prompt NO_x was discovered by Fenimore in 1971, noticing higher NO_x emissions than predicted by the previous two mechanisms. This would only occur in hydrocarbon-air flames, where an H-C molecule part reacts with molecular nitrogen to create atomic nitrogen and consequently form NO (see eq. (2.2))[9, 33].

N_2O-INTERMEDIATE NO_x

In the N_2O-intermediate mechanism, nitrous oxide (N_2O) is acting as an intermediate species in the creation of NO_x in an elaborate series of reactions (see a simplified version in eq. (2.3)). This mechanism is the dominant creator of NO_x at lower combustion temperatures, meaning below 1500 - 1600°C[9, 33].

$$O_2 + M \leftrightarrow O + O + M \qquad O + N_2 \leftrightarrow NO + N \qquad N + O_2 \leftrightarrow NO + O \tag{2.1}$$

$$CH + N \leftrightarrow HCN + N \tag{2.2}$$

$$N_2 + O + M \leftrightarrow N_2O + M \qquad N_2 + O \leftrightarrow NO + NO \tag{2.3}$$

In eqs. (2.1) and (2.3) M is a third-body species to stabilize the reaction, this can be any inert molecule [34]. Because this is a third-body reaction, it has a low activation energy [30]. The Fenimore mechanism will also contribute more to NO_x emissions, when high mixing rates between fresh reactants and burned gases are present [35].

2.1.2. SOLUTIONS FOR NO_x REDUCTION

By eliminating some of the requirements for the NO_x formation mechanisms presented in section 2.1.1, ways can be sought to reduce NO_x emissions. The following ways can be distinguished, including important comments after each statement [10]:

1. **Lowering the availability of nitrogen;** is hard to establish when using atmospheric air as oxidizer.
2. **Lowering the availability of oxygen;** can be established in different ways as will be shown.
3. **Lowering the combustion temperature;** an effective way of reducing NO_x, since the rate of thermal NO_x production reduces quadratically with a temperature decrease.
4. **Lowering the residence time at high temperatures;** reducing the time available for NO_x production.
5. **Handling NO_x creation post combustion;** chemically taking away NO_x emissions from the exhaust gases often presents the need for bringing extra substances or heavy and costly systems on-board.

These ways affecting the NO_x reaction mechanisms can be applied in practical solutions. These solutions are listed below, including the corresponding number(s) of the way(s) as mentioned above.

Low N2-fuel (1) Usage of fuel with low concentrations of nitrogen reduces fuel-bound NO_x.

Water Injection (3) Injecting water, increases the heat capacity of the flow, lowering the temperatures. This is applied in industrial gas turbines, but not feasible for aircraft engines [9, 32].

Leaner (premixed) mixture (3) Increasing the percentage of air entering the combustor gives a leaner mixture, hence lower temperatures. Unfortunately this will reduce the flame stability, give higher concentrations of UHC's and CO (indicating incomplete combustion) and increase the possibility of blow-out or backfire [9]. See fig. 1.5 for a clear representation of these consequences.

Homogeneous air-fuel mixture (3) Combustion of a homogeneous mixture avoids peak temperatures.

Staged combustion (2)(3) Either fuel or air is entered in a staged fashion to operate in the very lean or rich region of combustion, both lowering the NO_x emissions [9].

Quenching (4) When the combusted gases are quenched immediately after combustion, stopping the reactions by cooling them, high temperature residence times can be minimised. Having complete combustion before quenching is necessary, if combustion is not present afterwards again.

Flue gas recirculation (2)(3) When (inert) flue gas is taken from the end of the combustion chamber and entered back into the primary zone, this will lower the concentration of the reactants. As such, lowering the heat release rate and the oxygen concentration. It also enables a more homogeneous combustion and lowers the energy needed to be added to reach the activation energy [9].

Chemical addition (5) Ammonia can be injected into the burnt mixture to react with NO_x. Or using a secondary stream of fuel downstream can be used to form CHN and reduce NO_x emissions [29].

Use of non-HC fuels (1) This will reduce the prompt mechanism and also will be less likely to have nitrogen bound to it, reducing the fuel-bound mechanism [10].

2.1.3. DESIGN APPROACHES FOR NO_x REDUCTION

The solutions presented in section 2.1.2 can be applied both individually as well as together with others. This section presents and elaborates upon the design approaches and combustion regimes that use these solutionsm, listing them below. Before doing so, the term 'equivalence ratio' is first discussed, as it is crucial for understanding the theory behind these technologies and regimes.

The ratio between the mass of fuel with respect to the mass of air present can be defined. This is called the fuel-to-air ratio (FAR) or the air-to-fuel ratio (AFR). Comparing these ratios with to the stoichiometric ratio gives the equivalence ratio, where the stoichiometric ratio is the ratio where the reactants are present in exact proportions. Two versions of the equivalence ratio exist depending on the usage of FAR or AFR, namely the fuel-air equivalence ratio and the air-fuel equivalence ratio. These are depicted by ϕ and λ and represented by eq. (2.4) and eq. (2.5), respectively. In their formulation, m is the mass, n corresponds to the number of moles and the subscript st is short for stoichiometric.

$$FAR = \frac{\dot{m}_{fuel}}{\dot{m}_{air}} \quad (2.4a) \qquad AFR = \frac{\dot{m}_{air}}{\dot{m}_{fuel}} \quad (2.5a)$$

$$\phi = \frac{FAR}{FAR_{st}} \quad (2.4b) \qquad \lambda = \frac{AFR}{AFR_{st}} \quad (2.5b)$$

$$\phi = \frac{\dot{m}_{fuel}/\dot{m}_{air}}{(\dot{m}_{fuel}/\dot{m}_{air})_{st}} = \frac{\dot{n}_{fuel}/\dot{n}_{air}}{(\dot{n}_{fuel}/\dot{n}_{air})_{st}} \quad (2.4c) \qquad \lambda = \frac{\dot{m}_{air}/\dot{m}_{fuel}}{(\dot{m}_{air}/\dot{m}_{fuel})_{st}} = \frac{\dot{n}_{air}/\dot{n}_{fuel}}{(\dot{n}_{air}/\dot{n}_{fuel})_{st}} \quad (2.5c)$$

(fuel-air equivalence ratio) (air-fuel equivalence ratio)

Please note that in the remainder of this report the term equivalence ratio will be used to denote the fuel-air equivalence ratio ϕ.

Lean Combustion In lean combustion the equivalence ratio is less than 1. This way the temperature of the combusted gases is decreased, because more air is to be heated up with the same amount of fuel. Operation at low equivalence ratios near the lean blow-out (LBO) limit, gives rise to problems such as flame instability, unwanted emissions and acoustic instabilities.

Lean premixed (prevaporized) combustion, LP(P) LPP is similar to the previous approach, but it premixes or prevaporises the fuel before entering the combustion chamber. This reduces the presence of high temperature zones during combustion. Prevaporisation is done for liquid fuels resulting in a mixture with similar characteristics as a gaseous one. This enables the use of liquid fuels in a gas-fired turbine, with the same emission behaviour as a gas, resulting in cleaner combustion. Another advantage of LPP is that soot is reduced, giving less radiation to the combustor walls. Drawbacks of this design are chances of flashback and of autoignition for operation in aero engines [6, 9].

Lean Direct Injection, LDI LDI is an alternative to LPP, for which the fuel is not premixed with the air, but both are directly injected into the combustion chamber. Because there is no premixing, there is less chance of auto ignition or flashback. It does operate near the LBO limit, giving stability issues. To prevent high temperature regions, the fuel is atomised and mixed with the air before ignition occurs. This is established by injecting the fuel through a venturi and the air through a swirler (see figure fig. 2.1). This way, the droplet breakup process can be influenced and optimised, the fuel is atomised well and the fuel and air are mixed well before ignition [6].

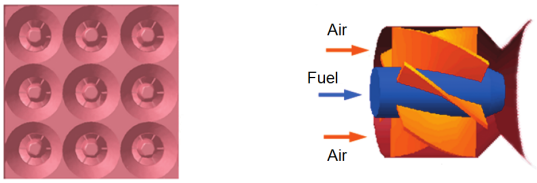

Figure 2.1: Nine-element LDI outlet configuration and lay-out of a single air swirler-fuel injector, (modified from [6])

.

Rich burn quick quench lean burn combustor, RQL This design approach operates first at rich conditions ($\phi > 1.6$), then quenches the flame and afterwards finishes combustion in lean conditions. Thus both combustion zones operate in the low-NO_x regime. In rich conditions, too little oxygen is available for NO_x formation and in lean conditions the temperature is too low for thermal NO_x formation. The lean region is less stable, but the rich region anchors the flame. During the transition from rich to lean conditions, stoichiometric conditions are encountered increasing peak temperatures, so the quenching process should happen swiftly [9]. A schematic representation of an RQL combustion chamber can be seen in fig. 2.2.

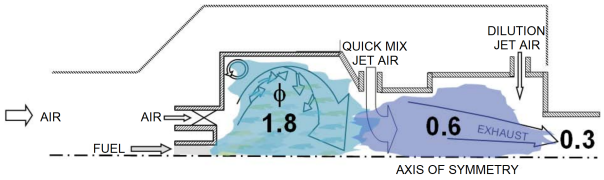

Figure 2.2: Schematic drawing of RQL with the respective equivalence ratios of the zones. Modified from [7].

Flameless Combustion Flameless combustion exist under low oxygen concentrations with the reactants being at auto-ignition temperature. Recirculation zones are needed to supply hot flue gases back to the burner zone and mix with the incoming air and fuel. The diluted mixtures yields a more distributed heat release in a larger volume, minimizing thermal NO_x formation. The increased temperature of the reactants helps in overcoming the activation energy in the reactions. Due to the uniformly well distributed combustion zone, the acoustic oscillations are small, yielding a silent flame [9, 32]. The uniform temperature pattern and lower acoustic oscillations also decrease the wear of the materials and as such decrease the mean time between failure and increase reliability of operation [10]. Flameless combustion is also investigated with the use of hydrogen(-mixtures) as a fuel, reducing prompt NO_x, fuel-bound NO_x, CO_2 emissions and the use of fossil fuels [27, 30]. As this paragraph shows, flameless combustion is not that much of a design approach, but more of a specific combustion regime. Operation in this regime can be established using different designs, as will be explained in section 2.2. These designs are all potential applications of flameless combustion, but are not yet incorporated in gas turbines.

Flameless combustion is more promising than solely lean combustion, LPP, LDI or RQL, because it combines advantages of these designs.

- Operation at oxygen-deprived conditions without peak temperatures, reduces NO_x emissions.
- The fuel is non-premixed, giving less flashback and this allows for better dilution with the flue gases before auto-ignition occurs in these high overall temperatures.
- Operation without temperature peaks and lower acoustic oscillations lowers the material requirements of the combustion chamber and the high pressure turbine.
- Has the potential to meet the stringent ACARE goals.

Therefore, flameless combustion is chosen as a research area that deserves more attention. General problems to overcome are stability issues, establishing the auto-ignition temperature and adequate recirculation ratios and mixing of the flue gases, since these are all important requirements for flameless combustion operation. All this should be achieved in a limited volume and over a wide range of operations [11].

2.2. DESIGN APPROACHES FOR FLAMELESS COMBUSTION

Flameless combustion is a promising combustion regime to operate in, but it is yet unclear what the concept behind it exactly is and how it can be applied in designs. This section shall explain this and summarise the relevant research that has been performed to understand this regime.

2.2.1. FLAMELESS COMBUSTION CONCEPT

Flameless combustion can only be obtained with low oxygen oncentration in the combustion zone. It can be combined with lean conditions as well, however this is not a necessity for flameless combustion and the increased oxygen levels could also make it harder to obtain. Operation in these low oxygen concentrations or in very lean conditions, requires the reactants to be at auto-ignition temperature, overcoming the activation energies. The diluting flue gases bring the reactants to elevated temperatures because they have a high enthalpy from the combustion zone. These flue gases are mostly inert gases such as CO_2 and H_2O which have higher heat capacities than the reactants, also reducing the temperature peaks [36].

Figure 2.3 presents a good overview of the flameless combustion regime with respect to other types of flame regimes. It also clearly shows the need for operating at higher reactant temperatures for conditions with low oxygen concentrations. To prevent thermal NO_x from being produced, it is best to operate under approximately 1800K, however, if the oxygen concentration is low enough and all available oxygen is used by the combustion reactions, one can go above this threshold. Since oxidation of fuel has higher reaction rates than the production of NO_x, most oxygen molecules available will be used to oxidize the fuel in this case.

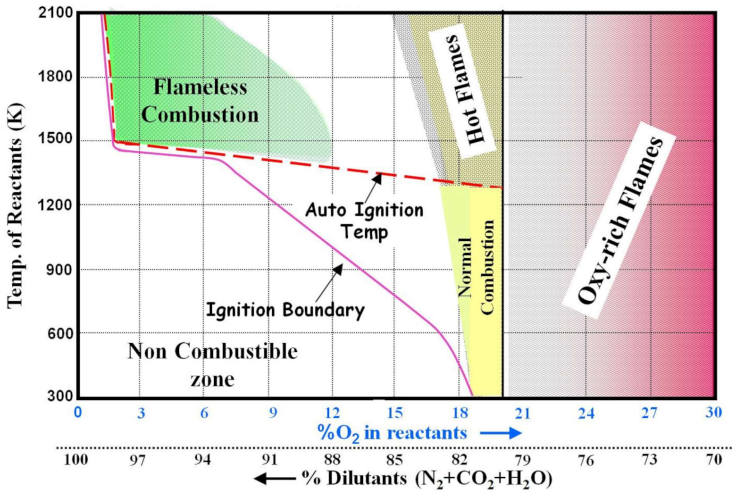

Figure 2.3: Different combustion regimes [8]

To quantify recirculation, eq. (2.6) has been defined [32], where K_V is the recirculation ratio, $\dot{m}_{rec}$ the recirculated mass flow, $\dot{m}_{fuel}$ the fuel mass flow and $\dot{m}_{air}$ the total air mass flow being put into the system.

$$K_V = \frac{\dot{m}_{rec}}{\dot{m}_{fuel} + \dot{m}_{air}} \tag{2.6}$$

A large challenge of flameless combustion is preventing the recirculated hot flue gases from combusting the reactants too early. One way is to dilute the oxidizer and the fuel mixture enough before reaching the auto-ignition temperature. Another way is by mixing the air or the fuel with the flue gases before the other one is introduced, to prevent concentrated combustion zones.[32]. To control this, the recirculation zones need to be understood well and the way the flue gases then mix with the flow of reactants coming from the jets.

2.2.2. DIFFERENT DESIGNS

Flameless combustion has been obtained in experimental setups using a number of design approaches that have been developed over time. The main distinction that can be made between these approaches is that some have jet induced recirculation, others geometry induced recirculation and a few supply the air in a staged manner [8]. Of these three approaches, the most known names of designs are FLOX®, FLOXCOM and COSTAIR, respectively. Next to these designs, experimental setups have also been built with just single simple burners, not giving rise to a patented technique. The designs mostly differ in geometry and the way air and fuel are added. They all try to accomplish the needed recirculation ratios, low oxygen levels and timely mixing, in their own way.

FLOX®

FLOX® can be an acronym for flameless oxidation, a synonym for flameless combustion, but has also been used to depict a certain patented design approach by WS Wärmeprozesstechnik GmbH in Renningen (Germany). These designs can be seen in fig. 2.4. The single nozzle design can be seen on the left in this picture, which first mixes the air and fuel and then aspirates the flue gas. In the middle, the multi air-nozzle is depicted where first mixing of air and flue gas is performed and then fuel is aspirated, using multiple air nozzles and a single fuel nozzle. On the right a combination of multiple single fuel and air nozzle is used [9, 32]. The FLOX®-burner design has been incorporated successfully in industrial furnaces showing extremely low NO_x emissions [32]. Research has not matured enough to apply flameless combustion to gas turbines and it is thus not yet operative there.

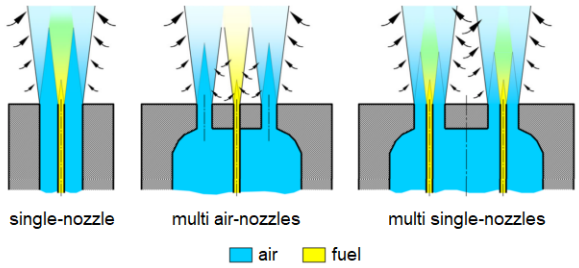

Figure 2.4: Schematic representation of FLOX® burner designs, modified from [9]

FLOXCOM

FLOXCOM is a design approach of which the principle can be seen in fig. 2.5. In this concept the inlet position of the stirring air and of the fuel can be given a different position along the circular design. One can see such an alteration in fig. 2.6. As can be seen, also in this design, (stirring) air is mixed with flue gases up to the auto-ignition temperature, then fuel is added and oxidized. Part of the combustion products are led to the exhaust and diluted by another (dilution) air outlet. When done correctly, with the different mass flows in correct proportions and inlets at the right locations, flameless combustion can be established. Although not always operating in the exact same way, multiple research setups are present around the world [37, 38].

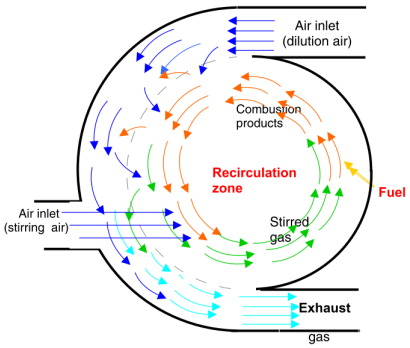

Figure 2.5: General scheme of the FLOXCOM burner[10]

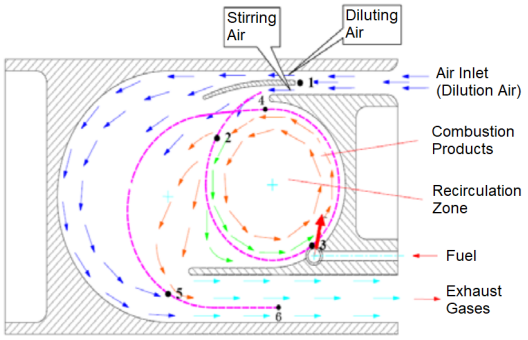

Figure 2.6: FLOXCOM burner design, modified from [11]

COSTAIR

Continuous staged air combustion, or its acronym COSTAIR, is a design approach where the air is supplied in multiple stages. This can be done from a long tube with multiple holes extending from the burner axis (as depicted in fig. 2.7), or from multiple holes (in the axial direction) along the liner length. Meaning for the latter that air is added from the wall and not the centreline. This approach spreads out the flame front [12]. Fuel is supplied either trough a circle around the tube, or trough a jet in the centre of the liner circle. In the COSTAIR design the combustion air is not all supplied directly, which is in contrast to the FLOX® design. As such, in the beginning the equivalence ratio is slightly higher, yielding higher temperatures, which could yield more NO_x, but also provides more stability. The COSTAIR design allows operation at not only a full diffusion flame, but also partially premixed fuel. However, in both conditions, the combustion air may never contain any fuel [12].

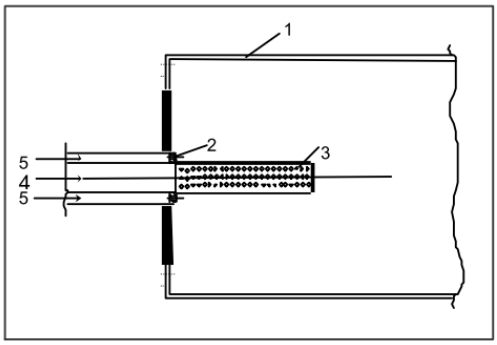

1 combustion chamber wall
2 fuel nozzles
3 combustion air distributor
4 combustion air supply
5 fuel supply

Figure 2.7: COSTAIR burner for flameless oxidation [12]

OTHER DESIGNS AND COMPUTER MODELS

Next to these three distinguished design approaches, some researchers develop their own method and experimental setup to investigate flameless combustion [15, 28, 39–47]. Others use one of the three design approaches but use different names than have been presented here [48]. Next to experimental setups computer models are also intensively used to try describing the working ways of flameless combustion and test the influence of the different variables [10, 11]. Many others write about doing both [9, 12, 26, 30, 32, 37, 38, 42, 43, 45, 47, 49].

VARIABLES

Important to keep in mind when comparing different flameless combustors is that not only different design approaches exist, but also within the designs there can be differences. This differentiation is important to know since a different burner design approach with equal conditions can yield very different outputs and hidden research gaps might be present. Important variables to distinguish the design on are:

- Burner type
- Chamber shape
- Dimensions
- Cooling channel
- Nozzle type
- Thermal power
- Operating pressure
- Preheat temperature
- Jet nozzle velocity
- Fuel composition
- Thermal intensity

2.2.3. RELEVANT / DIFFERENT SETUPS

As discussed earlier many different experimental setups exist. However, at the faculty of Aerospace Engineering of the DUT, a FLOX® burner is present. Therefore this setup is most relevant for this literature study. As such, only other setups from around the world that also use a FLOX® burner and have a largely circular combustion chamber, are investigated and portrayed in a clear overview in table 2.1. This limits the relevant setups greatly with respect to, for instance, the ones given by Arghode et al. [50]. Afterwards, overviews of the different setup characteristics and their respective investigations are individually described as well. The variables that have been investigated, parameters that have been measured, results that have been obtained and which possible uncertainties are left are all identified.

Table 2.1: Overview of the flameless combustion experimental setups using the FLOX® design approach

Shape	Dimensions $[mm]$	Cooling channel	Nozzle type	$P_{max,thermal}$ $[kW]$	Pressure $[bar]$	ϕ	T_{air} $[^oC]$	Fuel	NO_x $[ppm]$	CO $[ppm]$	Source
Delft University of Technology (DUT), Netherlands											
Can	156-156-468	Yes	MSN	464	4.74	0.57 - 0.8	15 - 300	NG	10	3000	[9, 26]
Can	-	Yes	MSN	464	4.75	0.59 - 0.83	15 - 300	NG	4	10	[51]
WS Wärmeprozesstechnik GmbH (WS), Germany											
Can	300-300-1000	Yes	MSN & SN	250	1.01	0.91	800 - 1050	NG	0 - 160	-	[32]
Gas- und Wärme- Institut Essen e.V. (GWI), Germany											
Can	100-100-300	No	MSN	30	1.01	0.4, 0.5	420	NG	10	10	[12]
University of Cincinnati (UC), USA											
Can	100-100-100	No	MSN	-	1.01	0.3 - 0.6	250 - 550	NG	25	25	[15]
Can	100-100-100	No	MSN	-	1.01	0.3 - 0.6	823	Propane	30	30	[42]
German Aerospace Centre (DLR), Germany											
HX Can	100-100-200	Yes	MSN	475	20	0.38 - 0.54	588 - 714	NG, NG&H_2	37	3	[27]
HX Can	100-100-200	Yes	MSN	500	20	0.38 - 0.54	703	NG, NG&H_2	37	3	[30]

Clarification: CSTR = COSTAIR, FLCM = FLOXCOM, HX Can = Hexagonal can, MSN = Multi single-nozzle, SN = Single-nozzle, NG = Natural Gas

DELFT UNIVERSITY OF TECHNOLOGY (DUT), NETHERLANDS

Vaz [9, 26]

Daniel C. Vaz has designed the flameless combustion chamber at the DUT with the FLOX® burner and has run experiments with it. This combustor has been designed with future experiments in mind, meaning that it is flexible in its use (e.g. it can change its L-D ratio) and has optical ports that allow for visual assessment. Using a cooling channel around the liner, the wall temperature of the combustion chamber (T_{wall}), can be regulated and as such regulate the degree to which adiabatic operation is obtained. Note that this cooling air isn't mixed with the combustion air until the exhaust.

Experimental variables

P, bar	$P_{thermal}$, kW	ϕ	T_{wall}, ^oC	T_{air}, ^oC	L-D ratio	Nozzle d, mm	U_{jet}, m/s
1 - 4.75	50 - 465	0.57-0.80	620-870	20 - 300	1.5, 2.25, 3.0	8.37, 11.0	40 - 80

Measured parameters

O_2, CO_2, CO, NO_x species centreline profiles	using a quenched gas sampling probe
O_2, CO_2, CO, NO_x species gas temperatures	using a suction pyrometer
Radial profiles of the gases' temperature	using a thin-wire thermocouple
Acoustic pressure fluctuations	using acoustic sensors
Mean flow patterns	using tufts in non-reacting flow

Results

- Increasing T_{wall} to 870^oC lowers the CO concentration by 30%
- Increasing T_{wall} increases T_{gas}
- A low T_{wall} with a high ϕ yields higher CO values, due to a too cold mixture
- An increase of 100^oC in T_{air} yields only a T_{gas} increase of 60^oC maximum to 30^oC minimum
- Extinction happens if U_{jet} < $37 m/s$, for T_{wall}=785^oC and U_{jet} > $65 m/s$, for T_{wall}=775^oC and U_{jet} > $80 m/s$, for Twall=721^oC
- A smaller nozzle diameter enables burning at lower ϕ, a larger one at lower T_{wall}
- A smaller nozzle diameter yields larger CO concentrations due to smaller residence times, there is hardly an influence on NO values (within the measurement error)
- At a thermal power input of only 80 kW, T_{wall} should be at least 850^oC
- Higher thermal power inputs yield higher CO concentrations
- Shorter combustion chamber yields fourfold lower CO concentration values, with higher CO_2 values, this could indicate more complete combustion
- Higher pressure yield a higher power density and as such also lower CO and NO emission values
- A strong central recirculation zone can be seen with smaller peripheral zones next to it between the jet and the liner (see fig. 2.8

Uncertainties

- Lower CO concentration could be from lower T_{wall} or different reaction zone structure
- A higher T_{wall} with a lower ϕ yields a lower T_{gas}, but a lower T_{wall} with a lower ϕ also yields a lower T_{gas}, but a lower T_{wall} with a lower ϕ also yields a lower T_{gas}

de Groot et al. [51]

For the 'New Combustion Systems for Gas Turbines' (NGT) project of the European Commission, M. C. de Groot has been responsible for the flameless combustion research performed at the DUT [51]. It should be noted that this information is not taken from a reviewed or published paper but the final technical report of the NGT project, dated the 31st of January 2005.

Experimental variables					
Pressure	Thermal Power	ϕ	T_{wall}	T_{air}	L-D ratio
1 - 4.75 bar	50 - 465 kW	0.59-0.83	550-860^oC	20 - 300^oC	1.5, 2.25, 3.0

Measured parameters	
O_2, CO_2, CO, NO_x species centreline profiles	using a quenched gas sampling probe
O_2, CO_2, CO, NO_x species gas temperatures	using a suction pyrometer
Radial profiles of the gases' temperature	using a thin-wire thermocouple

Results

- The combustion zone is approximately 1D long
- Sound pressure levels are lower for flameless combustion than flame mode
- NO and CO values of 4 and 10 ppm, respectively

Uncertainties

- Lower sound pressures cannot be exclusively related to the flameless combustion regime, but possibly also the ϕ stability limit

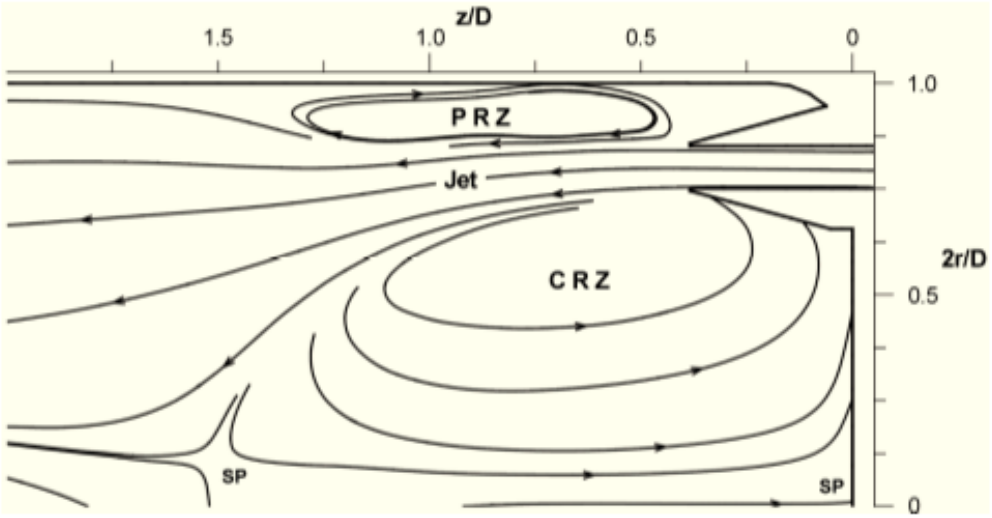

Figure 2.8: Computer modeled representation of the Peripheral Recirculation Zone (PRZ) and the Central Recirculation Zone (CRZ) [9]

WS WÄRMEPROZESSTECHNIK GMBH (WS), GERMANY

The original inventor and manufacturer of the FLOX® burner, the company WS Wärmeprozesstechnik GmbH in Germany, has published a paper in 1997 describing their first results [32].

Wünning et al. [32]

Experimental variables			
$P_{thermal}$	T_{air}	No. of nozzles	Modes
6 - 250 kW	800 - 1050^oC	1, 6	Flame / Flameless (FC)

Measured parameters	
Axial profiles of the gases' temperature	using a 0.05 mm thermocouple
Flow velocity	using the dynamic pressure*
Noise levels	*not stated*

Results

- The near burner temperature field becomes significantly cooler in FC mode
- The postcombustion zone temperature field shows similar behaviour for both modes
- Flame mode noise is at 100 dB(A) w.r.t. 80 dB(A) for base and FC mode noise
- Flame mode produces 160 ppm NO w.r.t. 6 ppm and < 2 ppm in FC mode, for $T_{chamber}$ of 1000^oC and 900^oC, respectively
- At $T_{chamber}$ = 850^oC, FC mode is attained
- At the best conditions, FC is attained with no visible or audible detection
- FC requires high circulation rates

**It is not stated how this dynamic pressure is measured*

GAS- UND WÄRME- INSTITUT ESSEN E.V. (GWI), GERMANY

The setup presented here is of a smaller size and $T_{thermal}$ than the one from the DUT and does not operate at elevated pressure levels. This research was also part of the EU NGT project, supervised by Flamme, who is one of the co-authors as well of this paper of Al-Halbouni.

Al-Halbouni et al. [12]

Experimental variables			
$P_{thermal}$	ϕ	T_{air}	Type of nozzles
15 - 25 kW	0.33, 0.4, 0.5	400 - 550^oC	1 SN, several MN and MSN

Measured parameters	
O_2, CO, NO_x, UHC species exhaust emissions	*not stated*
T_{air}, T_{fuel}, T_{wall}, $T_{fluegas}$	using thermocouples
Combustor inlet and outlet pressure	*not stated*
Flame pictures and OH-self radiation	using a CCD (charge coupled device) camera

Results

- MSN burners yield the shortest reaction rate and lowest NO_x and CO values
- The MSN burner yields near 1 ppm and 10 ppm NO and CO values, respectively
- These lowest values were obtained for ϕ=0.4 as well as ϕ=0.5

UNIVERSITY OF CINCINNATI (UC), USA

Li et al. [15]

Experimental variables				
ϕ	T_{air}	U_{jet}	Combustor diameter	Outlet diameter
0.3 - 0.55	250 - 550^oC	10 - 25 $[m/s]$	100, 150 mm	50, 100 mm

Measured parameters	
Gas temperatures	using thermocouples
Combustion chamber pressures	using pressure transducers
Exhaust acoustic signal	using a microphone
OH* levels	using a fiber optic with an OH* filter
Emission NO_x, CO, CO_2, O_2, UHC species	using an emissions sampling probe and chemiluminescence
2D velocity field on the streamwise plane	using Particle Imaging Velocimetry (PIV)

Results

- A greater $\dot{m}_{air}$ promotes the formation of FC and lower NO_x emissions for equal T_{flame}
- High preheat temperature and flow rate help establishing stable combustion and as such FC
- Jet strength and distance between jets and the wall directly influence recirculation strength
- A higher T_{air} extends the LBO limit, from ϕ=0.41 at 250^oC to ϕ=0.28 at 550^oC
- The smaller outlet diameter hardly affects NO_x emissions, but increases CO values due to increased flow velocity and reduced residence times
- The larger combustor diameter allowed for larger vortices and mixing structure to develop, reducing NO_x levels twofold and more
- The larger combustor diameter decreased stability, shifting the LBO limit from ϕ=0.28 to ϕ=0.42, by reducing the central recirculation zone strength, crucial for FC stability
- Low CO values are obtained even near the LBO limit, in contrast to normal lean combustion

Duwig et al. [42]

Since this setup is the same as for the publication of Li et al, only new results are given.

Experimental variables	
ϕ	U_{jet}
0.31 - 0.63	10 - 35 $[m/s]$

Measured parameters

Equal to the setup stated above

Results

- Decreasing ϕ from 0.6 to 0.3, gradually shifts the combustion mode from flame to FC, to LBO at 0.31
- For lower equivalence ratios, the reaction is more distributed and shifts downstream, until all burners produce one merged reaction zone
- Despite low emission values, around ϕ=0.42, acoustic fluctuations are measured rendering it non-FC
- Maximum strength of the recirculation zone is established at X/D=0.5 approximately
- The jet and recirculation zone shapes are similar between the reactive and non-reactive case
- The reactive case reduces the recirculation rate w.r.t. the non-reacting case
- The present stability range is limited, making it yet unsuited for gas turbine operations

GERMAN AEROSPACE CENTRE (DLR), GERMANY

Lückerath et al. [27]

Experimental variables				
ϕ	T_{air}	Fuel	U_{jet}	P_{max}
0.38 - 0.54	327 - 462^oC	NG, NG&H_2	40 - 160 $[m/s]$	20 bar

Measured parameters	
Exhaust temperature	using a thermocouple
O_2, CO_2, NO, NO_2 species exhaust concentrations	using a suction probe
Reaction zone outline	using OH* chemiluminescence (CL) imaging
Relative temperature distribution	using planar laser-induced fluorescence (PLIF) of OH*

Results

- A large central and smaller outer recirculation zone are established
- Succesful operation of the FLOX® combustor with low emissions at high pressure
- A higher jet exit velocity increases the low emission operating range
- For the highest T_{air} and U_{jet}, NO_x emissions of <10 ppm are achieved for ϕ < 0.48, together with distributed flame and temperature zones
- CO concentrations are low as well, until the LBO limit at ϕ=0.37
- Adding H_2 to the fuel mixture increases range of stable operation, but NO_x emissions rise

Sadanandan et al. [30]

In this case U_{jet} is increased by increasing the total mass flow, increasing the thermal power of the setup too. This setup is similar to the setup of the publication of Lückerath, thus only new results are given.

Experimental variables					
$P_{thermal}$	ϕ	T_{air}	Fuel	U_{jet}	Fuel - jet nozzle distance, dl
141 - 500 kW	0.38 - 0.54	430, 600^oC	NG, NG&H_2	40 - 160 $[m/s]$	0, 12, 24 mm

Measured parameters	
Inside temperature, absolute and differential pressure	using different probes
Rest of the parameters is equal to the setup stated above	

Results

- With H_2 added to the fuel, the flame burners closer to the burner, due to increased reaction rates
- Recirculation rates of burned gases largely influence emission levels
- Heat release zones shift downwards for smaller dl, due to less premixing
- More premixing, or larger dl, leads to a too early ignition of the fuel and higher NO values
- Too high NO values from premixing can be battled using a higher U_{jet}
- A dl of 0 gives a too narrow combustion zone
- Higher U_{jet} shortens the residence times

The main conclusion of this paper on achieving optimum combustion range with low emissions is: ”the recirculation rate should be such that the ignition delay is short enough to enable a reliable flame stabilization but long enough for burned gas dilution of the fresh fuel/air mixture before the reaction zone. At the same time, the combustor residence times should be short in order to suppress (thermal-)NO formation but long enough to oxidize CO to CO_2.”

CONCLUSION

From the results of the overviews shown in the previous section the following conclusions can be drawn, structured into four main categories.

General

All papers have shown very low NO and CO values with respect to conventional combustion. Even near the LBO limit, where incomplete combustion is usually present, CO values have stayed lower than for normal lean combustion. However, the ranges of ϕ for which FC has been obtained, is still limited to a maximum of 0.3. Flameless combustion mode has also been established at high pressure, with low NO and CO values, making it more feasible for operation under gas turbine conditions. It has also been shown that operation with fuel mixtures of NG with H_2, instead of solely NG, can reach FC mode and even increase its range. However, due to the high reaction rates and burning temperatures of H_2, NO emissions do rise. FC mode also has less audible and visible detection than regular flame mode.

Lastly, it can be seen that a battle still exist in the combustion chamber between mixing time scales and reaction rate time scales. Increasing residence times increases emisisons and increasing mass flows increases mixing but decreases residence times, increasing emisisons. Inside a gas turbine combustion chamber, flameless combustion is only determined by internal aerodynamic and thermodynamic processes making it hard to control the regime and ensure low emisisons[11].

Operational temperatures

It has been shown that higher preheat (T_{air}) temperatures yield higher T_{gas} values and these give lower NO and CO values, because of more complete combustion. It is also shown that the temperature gradients decrease, rendering a significantly cooler near burner temperature field for FC mode. In addition to this, the postcombustion zone temperature field is similar for both modes.

Jet geometry

A smaller jet nozzle diameter enables burning at lower ϕ, and a larger diameter at lower T_{wall}. The larger range for smaller jet nozzle diameters does come at a cost, because it yields larger CO concentrations due to shorter residence times. It has also been shown that of the different jet configurations (SN, MN, MSN), MSN burners yield the shortest reaction rates and the lowest NO_x and CO values. If more premixing is present within the burner though, because of a larger distance between the fuel nozzle and the jet nozzle, this will lead to a too early ignition of the fuel and as such higher NO values.

Combustion chamber geometry, recirculation zones

In all papers it is shown that recirculation zones exist and that FC mode requires high recirculation rates in order to sustain. Often a strong central recirculation zone (CRZ) can be seen with smaller peripherial recirculation zones (PRZs) next to it, between the jet and the wall. A larger combustor diameter yields a weaker CRZ decreasing stability by increasing the LBO limit. However, it lowers NO_x values because of the larger mixing structures that form. The recirculation zone structure is approximately equivalent for the reactive and the non-reactive case. However, the recirculation rate is reduced in the reactive case. It has also been found that a shorter combustion chamber yields fourfold lower CO concentration due to more complete combustion. It should be kept in mind that the combustion chamber should not become smaller than the size of the combustion zone, otherwise the opposite will occur, but this zone was found to be approximately 1D long.

An important notion on the recirculation intensity is that it should be such that there is enough time for the three components (air, fuel, flue gas) to mix, but that ignition is established on time to stabilize the flame. The residence time in the flame should then again be long enough to ensure complete combustion, but suppress thermal NO-formation. As can be seen, there is a delicate balance present in flameless combustion mode, restricting the stability range. It was concluded that, at the moment, the stability range is unsuited for gas turbine operations.

General challenges that are present now in flameless combustion are understanding the regime and its boundaries of which the definitions are still not agreed upon [8]. In the end applying it in the limited volume of an aero engine, requiring high power densities, will also pose a challenge.

2.3. RESEARCH DEFINITION

This section takes a step back from literature and identifies the grey areas of interest for this research. Based on this a research proposal is written, stating the research objective and the research question, including its subquestions. The feasibility and novelty of this research are discussed at the end.

2.3.1. GREY AREAS

Grey areas are areas in the research field that are not yet fully developed and where questions and uncertainties still lie. Using the research presented in section 2.2 and with the possibilites of the DUT setup in mind, grey areas are identified that aid in realisation of flameless combustion actual gas turbines and aero engines. These are listed below. Some of these are taken from section '8.2 Suggestions for future work' from Vaz [9].

NON-FLAMELESS COMBUSTION MODE [9]

The DUT setup has only been operated using its FLOX® burner. Even at non-flameless combustion conditions, the way it burns is much different from conventional flames. Therefore it is not yet possible to put emission species values, reaction zone or flow structures of the FLOX® burner into perspective. Designing a conventional burner, with for instance a swirler for flame stabilisation, could help in this.

MEASUREMENTS OF UHC SPECIES [9]

The DUT setup cannot yet measure UHCs, and it is therefore sometimes hard to decide whether or not complete combustion has taken place. CO values are a way of identifying it, but since they are only an intermediate reaction species, they do not give decisive answers. CO_2 values combined with CO values give an indication, but UHC values are to be known in order to draw proper conclusions.

MEASURE OH* [9]

Having more information about the reaction zone structure would aid in drawing more decisive answers on the appearance of the lower CO concentration, lower sounds pressures and also the seamingly contradicting findings on the influence of T_{wall} and ϕ on T_{gas}. Next to these uncertainties, it would present a picture of the reaction zone, which is not visually detectable, and as such allow to get results on the starting and ending point of it. As can be seen from the setups, measuring the OH* cloud can be done using a fiber optic with an OH*-filter [15, 42] or by using chemiluminescence [27, 30].

PARTIAL LOAD OPERATION [9]

Aero engines need to be able to operate at many different regimes and also at partload. Operating only half of the nozzles would change the recirculation zones heavily and investigating this impact on flameless combustion would help a lot to improve its application.

INFLUENCE OF COMBUSTION CHAMBER LENGTH ON THE STABILITY RANGE

In the investigations of Vaz [9], the combustion chamber length has been adapted and its influence on the emissions has been investigated. It showed that CO values dropped dramatically, which was concluded to mean that more complete combustion was attained. However, nothing has been said on its influence on the stability range. A smaller combustion chamber length would be a competitive advantage, but one would not want to lose on stability range, makint this is a relation worth looking into.

VISUALISATION OF INNER AERODYNAMICS

The internal aerodynamics of the DUT combustor have already been investigated by Vaz [9], using computer simulations and using wool tufts. The wool tufts gave a qualitative validation of the computer simulations, but do not accurately show the exact aerodynamic flows inside the combustion chamber, nor do they display smaller vortex structures. Since recirculation has such a great influence on the working ways of flameless combustion, it would be important to understand the internal aerodynamics well. This could for instance be done using PIV as has also been done by the University of Cincinatti on their setup, which is different [15, 42]. Investigating this with PIV could first be done for a non-reactive flow, then for a reactive flow, to see if this indeed doesn't have much of an influence as Duwig et al. state [42]. This would also allow to see the change in internal flow when using a reduced combustor length. Complimenting PIV with CFD would allow for an even more complete analysis of the flow.

GREY AREA DISCUSSION

The largest influence in the trade-off of the grey areas, will be that the setup has not been used at this moment yet. It shall therefore first need to be tested and operated at cold flow. Operation at elevated temperatures or with reactive flow is not feasible within this MSc thesis. Because of this, but also amongst other reasons, only the final grey area is possible to be investigated.

Visualisation of the inner aerodynamics using PIV is something that could be performed at the combustor setup, since this diagnostics technique is already present in the laboratory. With the use of literature and linking this to any findings on the aerodynamics, perhaps part of the 5^{th} grey area could still be covered.

RESEARCH OBJECTIVE

Since PIV equipment and CFD software is present at the moment in the laboratory, this is the only possibility to use for the thesis. Therefore, the goal of this research will be to quantify the influence of the operational parameters on the flow structure and then link this to improving the application of flameless combustion operation to gas turbines. From this the following research question with its subquestions can be obtained:

How can changes in operational variables of the DUT setup improve the applicability of flameless combustion to gas turbines?

- How can the application of flameless combustion to gas turbines be improved aerodynamically?
- What is the influence of the operational variables on the flow properties in the DUT combustion chamber?

The operational parameters that can be changed for cold flow in this setup are the combustion chamber length, the nozzle diameter and the flow velocity or air mass flow. Research has already shown that quantification of influence of these parameters can be done using PIV and CFD. Since PIV is needed to validate CFD, the former should have the main focus and afterwards this can be used to see the feasibility of modeling the DUT setup using CFD. The research-objective, with its subobjectives, of this thesis is therefore:

To improve the application of FC to gas turbines, by quantifying the influence of operational parameters on the aerodynamics inside the DUT setup, using the experimental PIV technique and a numerical study.

- Understand how the flow structures inside a combustion chamber can improve the operation of flameless combustion
- Visualise the internal aerodynamics for different operational settings using PIV
- Investigate the influence of operational variables on the internal aerodynamics
- Investigate the feasibility of validating a low-cost CFD model

These four sub-objectives together will make it possible to achieve the main objective and answer the research questions. When the objective is reached, this will also have enabled a continuation into this direction, by getting the DUT setup operational again and providing insight on which numerical approaches can or cannot model the setup well.

The combustion chamber has been used before and is therefore known to work. On the other hand, the setup around it is new and has not been operated, also not in combination with PIV. Therefore problems are likely to arise along the way. The novelty and motivation behind this research, shall be that the recirculation zones inside a combustor similar to that at the DUT have not yet been visualised experimentally. Since understanding these zones is crucial for the investigation of FC, visualising them shall aid greatly in trying to make FC feasible in aircraft engines and reducing NO_x emissions as such.

3

DUT Flameless Combustor Setup

A FLOX® combustor is present in the Propulsion Lab at the High-Speed Laboratory of the DUT. The origin and goal of this research setup is first discussed in section 3.1. Section 3.2 describes all the different parts of this setup and their purpose. Lastly the operational capabilities and shortcomings are discussed in section 3.3 to complete the understanding of this setup that enables the study of flameless combustion.

3.1. Origin

In 2007 Daniel Cardoso Vaz obtained his doctorate degree in Mechanical Engineering at the faculty of Science and Technology of the NOVA University of Lisbon in Portugal. His thesis concerned the designing, building and researching a FLOX®- combustor research setup. This setup was built at the Process & Energy Department at the DUT, but not used afterwards. Therefore it was shipped to the Propulsion Laboratory of Aerospace Engineering faculty in 2015 to be commissioned and used for research again.

Dr. Vaz has designed the setup to contribute to the research towards the conception of alternative gas-turbine combustors for low pollutant-emissions. The central research objectives were to experimentally evaluate the flameless oxidation technique under conditions representative of micro-gas turbines, in terms of pollutant emissions and combustion noise, and to better understand the near-burner aerodynamic phenomena associated with this technique. To reach these goals he [9]:

- Developed a can-type combustor with features relevant to the experimental assessment of the implementation of flameless combustion to this type of combustors. Such features include, for example: optical access, control of wall temperature independently of operating conditions, variable length of the combustion chamber, and operating pressure up to 5 bar(abs.).
- Tested this combustor in the flameless regime, under operating conditions relevant to micro-gas turbines: 464 kW and 4.74 bar(abs.), power density up to 70 MW m-3, and air preheating up to 300°C.
- Performed a parametric study involving both geometrical (combustion chamber length and nozzle diameter) and operational variables (e.g., air-to-fuel ratio, wall temperature, pressure, air preheat, injection velocity of the reactants, power density). This includes measurements of relevant chemical species (O2, CO2, CO, NO), along the centreline or at the exhaust, for different operating conditions. Study of the combined effect on combustion stability of the air-to- -fuel ratio, wall temperature and jet velocity.
- Compared the combustion-generated noise between conventional flame and flameless oxidation regimes.
- Acquired insight into the flow structure associated with the multiple nozzle configuration of the FLOX® burner under consideration for gas turbine application. Derivation of design guidelines of interest to manufacturers.

As wil have become clear from section 2.3, this research is in line with what Dr. Vaz had envisioned. It will expand on the visualisation of the flow structures inside the combustion chamber and the parametric study of geometrical variables on these flow structures, and give recommendations on what parameters would yield the best results for the flameless combustion regime.

3.2. COMPONENT DESCRIPTIONS

The research setup consists of the following main parts:

- The gas supply system
- The gas conditioning system
- The combustion chamber setup
- The exhaust
- Supporting components to enable (safe) operation of the combustion chamber setup

Air flows from the gas supply system through the gas conditioning system to the combustion chamber setup. It enters the combustion chamber through the FLOX®- burner head, which has 12 concentrically placed nozzles, creating the recirculation zones in the chamber. The air then flows through the exhaust into the atmosphere.

3.2.1. GAS SUPPLY SYSTEM

The gas supply system deliveres high pressure air from the main tank outside to the inside of the facilities.

AIR

Air for the combustion chamber is supplied by the main tank of the facility. It is pressurised between 20 and 42 bar and has volume of 300 m3. Before entering the propulsion laboratory, the air enters through a pressure reducing valve, a pressure relief valve and a ball valve. These safety measures ensure inside air pressures do not exceed 12 bar, limited by the gas conditioning equipment, and that the system can be depressurised on the outside.

DILUTION GASES AND FUEL

Next to compressed air, the gas supply system can also feed the dilution gases N_2, CO_2 and the fuels CH_4 and H_2 to the setup. Since these have not been used in this thesis they will not be discussed further.

SOLENOID VALVES

The last part of the gas supply system are the solenoid valves. They are connected to the Data Acquisition and Control (DAQ&C) System, so they can be controlled remotely. They are powered using a 24 V DC power supply incorporated in the circuit and have a response time of 15 – 120 ms. They can handle air pressure of 13 bar(a) and water pressures of 10 bar (a).

3.2.2. GAS CONDITIONING SYSTEM

The gas conditioning system comprises of different components that allow for controlling, adjusting and changing the gas flow from the gas supply system before being delivered to the actual combustion chamber setup.

MASS FLOW CONTROLLERS (MFC)

Every pipe in this system has its own MFC, delivered by Bronkhorst. They are connected to the DAQ&C System to be controlled remotely. Two of them are connected to the air supply system. The single pipe from the air supply system is split into two pipes to allow for one low mass flow and one high mass flow supply. This is necessary since the MFC's have a reduced accuracy below 5% of their maximum mass flow. The rating of the two MFC's are 3000 $lnpm$ and 500 $lnpm$, for air, with a pressure loss of 2 bar at max. flow and operating temperature of 20 degrees Celsius. Important to explain here is the unit $lnpm$ or *liters normalised per minute*. Bronkhorst delivers MFC's with two different units, where the other one is $lspm$ or *liters standardised per minute*.

Normalised and standardised refer to a certain set of conditions under which the instrument is calibrated. For both cases this the same pressure, but a different temperature is taken. This is shown in eq. (3.1).

$$P = 101325\ Pa \quad (3.1a) \qquad P = 101325\ Pa \quad (3.1c)$$

$$T = 273.15\ K = 0^oC \quad (3.1b) \qquad T = 293.15\ K = 20^oC \quad (3.1d)$$

(Normalised) (Standardised)

If these are set conditions under which a certain volum flow of liters per minute occurs, this automatically implies a certain mass flow. This is explained by looking at the formula relating the volume flow, $\dot{V}$ and the mass flow, $\dot{m}$ in eqs. (3.2) to (3.4) and incoporating the ideal gas law.

$$m = V \cdot \rho \quad (3.2)$$

$$\dot{m} = \dot{V} \cdot \rho \quad (3.3)$$

$$\dot{m} = \dot{V} \cdot \frac{P}{R \cdot T} \quad (3.4)$$

Since R is known, and through either the normalised or the standardised way, also P and T are known, allowing for the calculation of the mass flow, when the volume flow is given in $lnpm$ or $lspm$.

MIXER, HEATER, SEEDING PARTICLES INPUT

Behind the mass flow controllers, the air pipes and dilution gas pipes are united in a manifold and pass through a mixer. The effect of this SMI-W mixer is to create a homogeneous gas. The gas mixture then flows through the 48 kW heater, that can heat a volume flow of approximately 3500 lspm up to 900 K at a maximum static pressure of 10 bar. This heater has not been used in these experiments. After the heater the gas flows through a bend and then passes the seeding-flange. This flange has an input that leads to the seeding system, to allow the seeding particles to mix with the dilution gas and air flow from the gas conditioning system and be transported towards the combustion chamber.

3.2.3. COMBUSTION CHAMBER SETUP

The combustion chamber setup exists of a total of 3 separate sections, the burner head, the combustion chamber and the exhaust section, as depicted in fig. 3.1 by the three separate squares (a large version can be found in appendix A).

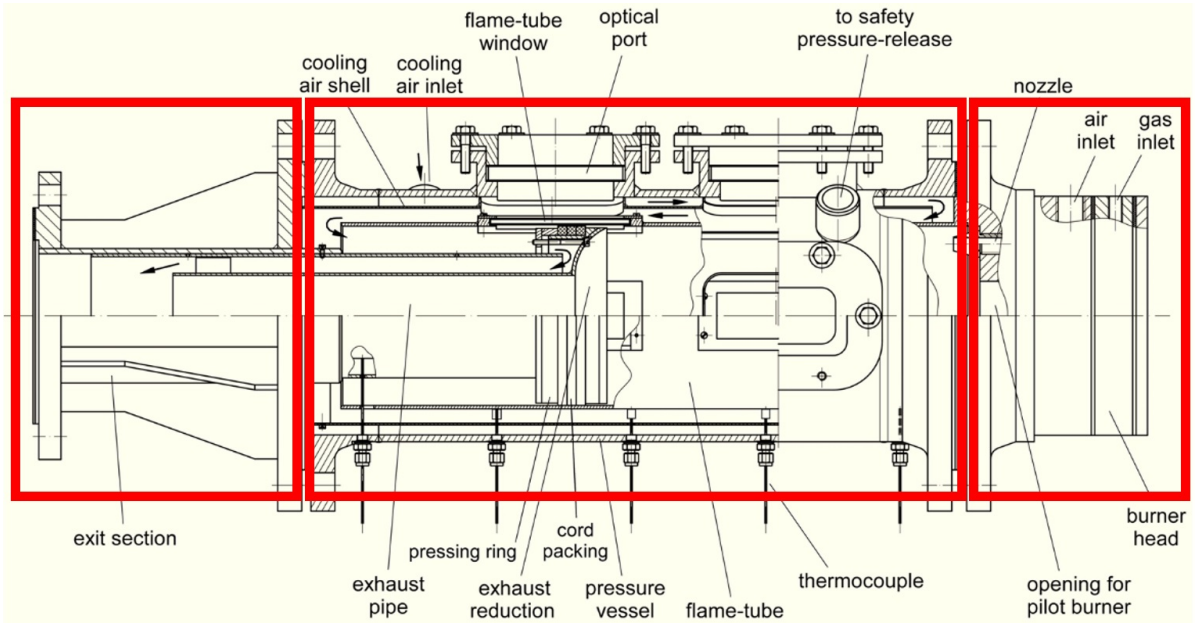

Figure 3.1: Schematic overview of the combustion chamber setup [9]

BURNER HEAD

The burner head has two separate inputs, namely a fuel inlet and a gas inlet. The gas inlet is connected to the pipe coming from the heater. The fuel inlet is connected to the hydrogen and methane pipes coming from the gas conditioning system. Figure 3.2 shows how the two different inputs come together in the burner head. '1' shows the air inlet, '2' shows the fuel inlet and '3' is a hole where the pilot burner is to be put. The latter hole is closed with a dummy made of steel in case the pilot burner is not used. The jets of the fuel inlet fit right into the concentric set of nozzles located on the front of the burner head.

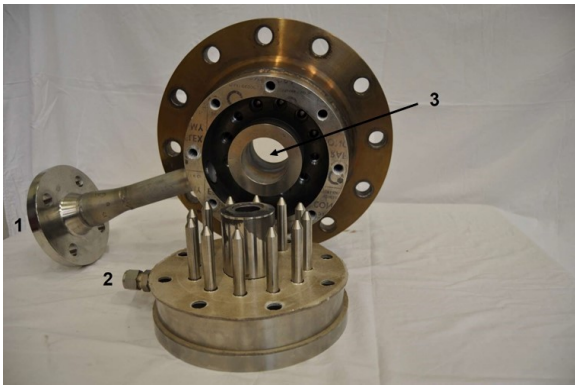

Figure 3.2: Inside of the burnerhead showing different inputs and the fuel nozzles

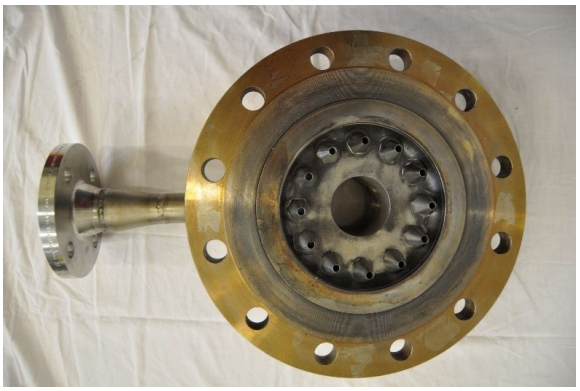

Figure 3.3: Front of the burnerhead showing the gas nozzles

The nozzles located on the front of the burner head can be changed. For this research three different diameters have been investigated which were present, namely 6.67 mm, 8.45 mm and 11.0 mm, shown in fig. 3.4. When changing the nozzles in between runs, the location of the different nozzles was recorded to make sure the distribution of the nozzles remained the same when nozzles were put back in the burner head.

Next to this, to accomodate PIV measurements in different planes, the burnerhead can be turned in its mounting bracket as is shown in figs. 3.5 and 3.6. For this research it was turned 15^o from plane A to plane B to have the PIV laser sheet illuminate the flow exactly in a plane in between two jets.

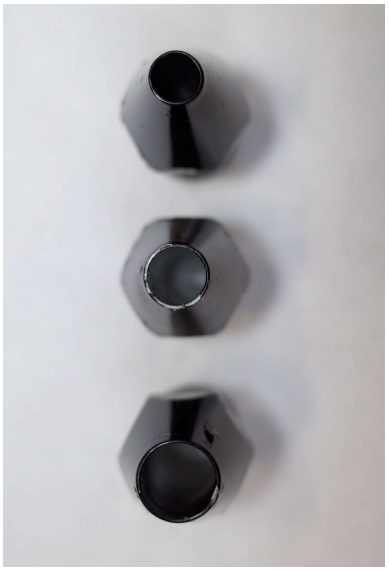

Figure 3.4: Different nozzles used, with d_{nozzle} = 6.67 mm, 8.45 mm and 11.0 mm (top to bottom)

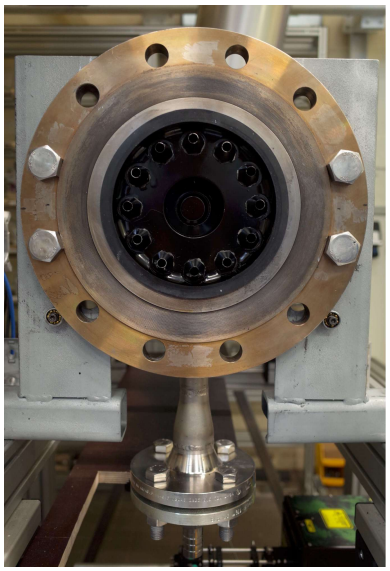

Figure 3.5: The burnerhead, shown in the Plane A configuration

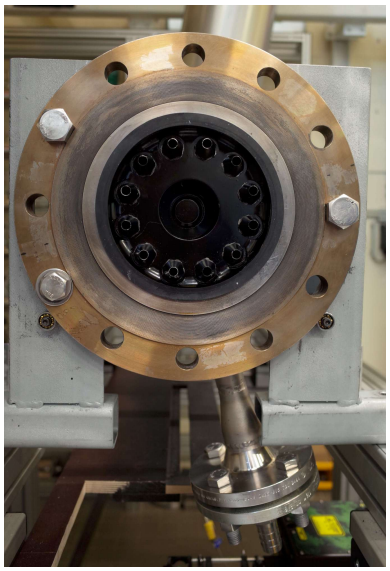

Figure 3.6: The burnerhead, shown in the Plane B configuration, tilted by 15^o

COMBUSTION CHAMBER (ORIGINAL)

The combustion chamber setup, which is where the actual research will take place, is made up of three concentric cylinders, enabling a division between the cooling flow and the combustion air. Windows are present on the sides and the top of the combustion chamber, and 5 thermocouples are located on the bottom reaching all the way to the most inner cylinder to measure the wall temperature. The outer shell contains quartz windows and is designed to withstand the pressure difference between the cooling air (at the same pressure as the combustion air) and the atmospheric air. It is therefore called the pressure shell.

The cooling air shell is concentrically placed within the pressure shell. It has cut-outs corresponding to the window locations and is suspended between the pressure and inner shell. This shell provides a more equal cooling flow along the inner shell and protects the pressure shell from radiation from the inner shell.

This inner shell is the flame tube, also containing quartz windows, and it acts as the dividing layer between the hot combustion air and the cooling air and has an inner diameter of 156 mm.

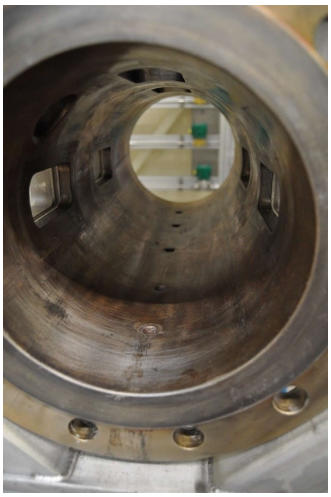

Figure 3.7: Inside of the pressure vessel, showing optical acces from three sides and thermocouple holes in the bottom

Figure 3.8: The cooling shell

Figure 3.9: The flametube, showing its quartz windows on three sides

COMBUSTION CHAMBER (TRANSPARENT)

As will be shown in section 6.1, the original combustion chamber does not allow for complete optical access of the inner aerodynamics. Therefore, this research has also used a clear cast acrylic cylinder with equal inner dimensions as the combustion chamber to provide for this optical access. Since the material properties of this cylinder do not allow for experiments at elevated temperatures, this setup can only be used in with cold flows. The cylinder in its installed position can be seen in fig. 3.10. The inner diameter of this tube is 155.5 mm, with a tube thickness of 4 mm and a length of 555 mm. It is fastened to the exit section using a PVC flange and the burnerhead will be secured agains the other side using a compact screwjack. No flange is used on this side to completely include the nozzle exits in the field of view.

A cast acrylic cylinder has been chosen for this application versus an extruded or polycarbonate cylinder for a few reasons. Although polycarbonate is a stronger material than acrylic, acrylic is more resistant to scratches and can be polished. Acrylic is also more transparent than polycarbonate. Cast acrylic also has a higher optical clarity, a higher resistance against solvents (e.g. PIV oils) and is more scratch resistant than extruded acrylic. A quartz glass cylinder could also have been used, however this is much more expensive and is very delicate and hard to work with and include in the combustion chamber setup. Since superb optical access over a longer period of time and workability are most important in this application, the cast acrylic cylinder has been chosen.

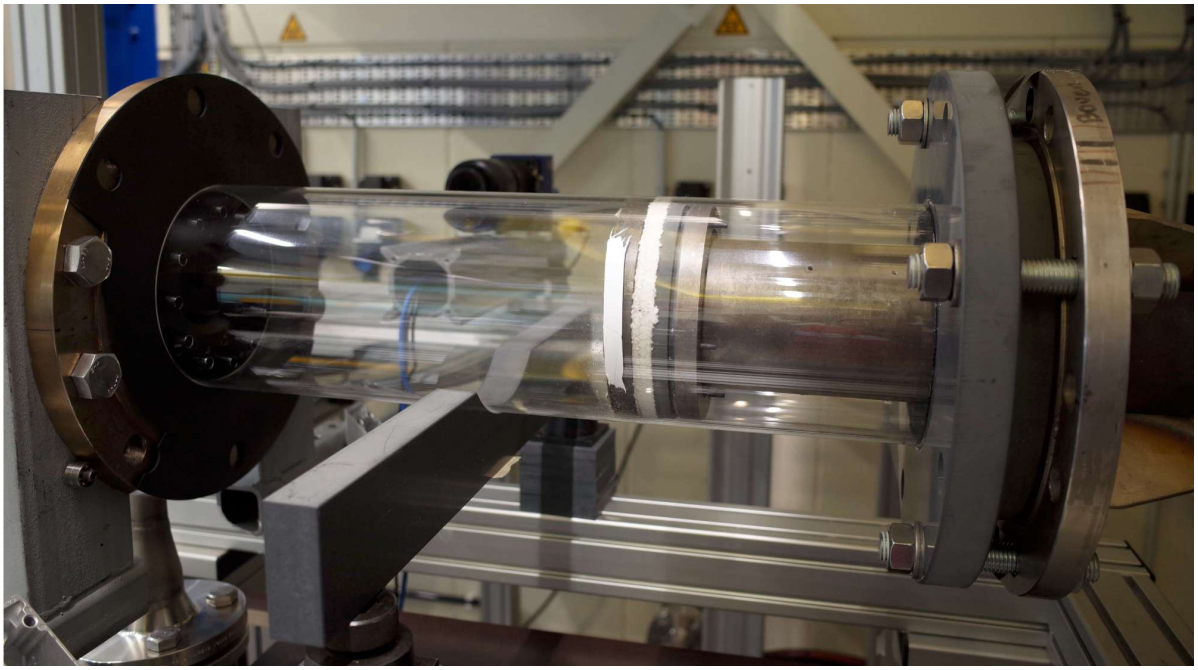

Figure 3.10: Installed transparent cylinder

Exhaust section

The exhaust section ventilates the combustion and cooling gases from the experiment to exhaust of the setup. The exhaust section consist of two parts as is depicted in fig. 3.11, the exit section and the exhaust pipe that fits in the exit section. The exit section supports the exhaust pipe to slide forwards and backwards changing the effective lengths of the combustion chamber. The pipe section consists of two layers, the inner one capturing the combustion air, the outer one guiding the cooling flow (see appendix D).

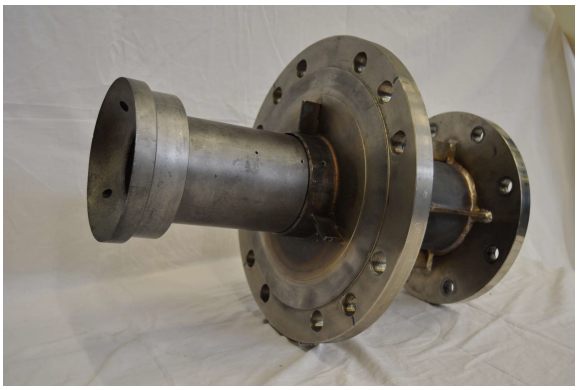

Figure 3.11: The exit section, showing the moveable exhaust pipe

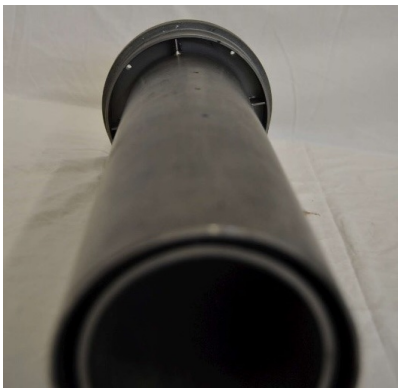

Figure 3.12: The moveable exhaust pipe, showing the separation between the cooling and combustion flow

Measurement flange

A measurement flange has been designed and manufactured to be positioned behind the exit section of the combustion chamber. It is depicted in fig. 3.13. Figure 3.14 shows a schematic cut-trough of the design, from which it can be seen that the cooling and combustion air remain separated throughout the design. The flange itself has holes on the outside that protrude to the inside. These holes can be used by thermocouples or pressure transducers to measure temperatures and pressures of the cooling or combustion air that flows through the exhaust.

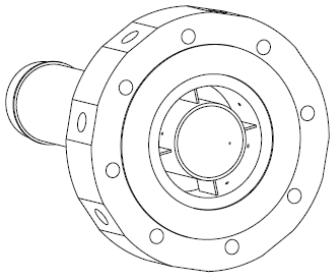

Figure 3.13: Technical isometric drawing of the measurement flange

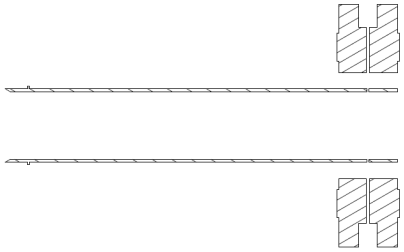

Figure 3.14: A vertical cut of the measurement flange, showing the divisiong between the combustion air and the cooling air and the holes protruding to the inside of the pipe

3.2.4. SUPPORTING COMPONENTS

EXHAUST

The exhaust leads the air from the combustion chamber exhaust outside through a fully open channel. It is heavily insulated to prevent the outer layer from getting hot and the outlet is shielded on the outside to prevent rain from coming in.

SEEDING AIR OUTLET & MFC

Shop air is delivered to the Propulsion Lab through a piping system that is in place in all of the Aerodynamics facilities. It is pressurised at approximately 8 bar. This shall be used to provide the seeding air in the experiments. The seeding air is passed through a ball valve, then an MFC rated at 500 $lspm$ for N_2 and is then connected to the seeding-flange. Bronkhorst has specified that no conversion ratio is needed to switch from $lspm$ rated for N_2 or air. It has a pressure loss of 5.52 bar at maximum flow. It is also controlled remotely via the DAQ&C System.

TEST BED

The test bed serves to support the combustion chamber, the heater and can hold experimental equipment. Due to its configuration, the combustion chamber can slide in all four directions in the horizontal plane, making assembly and dismantling easier.

DAQ&C SYSTEM

A National Instruments cRIO-9067 controller acts as the brain of the DAQ &C System and can be seen in fig. 3.15. The controller holds a NI-9482 C Series Relay Output Module to control the solenoid valves, a NI-9213 C Series Temperature Input Module to measure the temperature of the air through a K-type thermocouple in the heater and a NI-9205 C Series Voltage Input Module for the safety system. Next to this, the RS-232 input in the controller is used to the MFC's to. Through LabView on a computer, the MFC's and solenoid valves are controlled and their outputs as well as that of the thermocouple are logged.

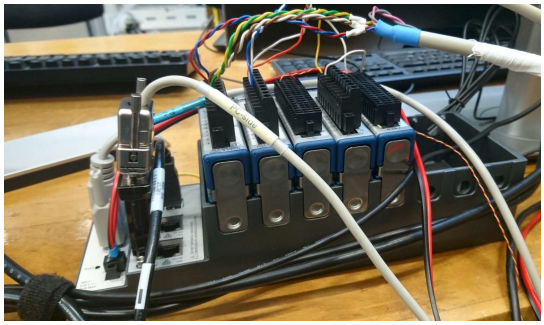

Figure 3.15: The National Instruments cRIO-9067 controller with the different modules installed

3.3. OPERATION

Operation of the setup is relatively straightforward, because of the DAQ&C System from which the solenoid valves and MFC's are controlled and the data of the MFC's and thermocouple is logged as well. This section shall therefore explain what the operational capabilities are for the experiments, how the temperature and pressure readings are performed and used and what the setup's shortcomings are.

3.3.1. OPERATIONAL CAPABILITIES

In cold flow settings, the operational capabilities of the setup are limited to the ones shown in table 3.1.

Table 3.1: Operational capabilities of the setup

Feature	Specification	Comments
Nozzle diameter	6.67, 8.45, 11.0 mm	-
Combustion chamber length	1.5 D, 2.25 D, 3.0 D (D = 156 mm)	Values between 1.5 D or 3.0 D are possible, but not yet mechanically integrated
Mass flow range	0 - 3500 $lnpm$	A too large ΔP over the gas supply system limits the flow at 2900 $lnpm$
Optical access	111 x 40 mm windows for $T_{elevated}$ fully transparent for T_{cold}	-
Seeding possibility	DEHS oil or Titaniumdioxide	Both deteriorate the inside of the transparent cylinder over time

3.3.2. TEMPERATURE AND PRESSURE READINGS

Temperature and pressure readings are important when dealing with air flows. Its accuracy will have a direct impact on the conversion of the mass flow readings from $lnpm$ or $lspm$ to the actual lpm. The temperature of the air was measured in this setup at the end of the heater using a K-type thermocouple as seen in fig. 3.16. The temperature reading through LabView was validated using an RS PRo 1319A Type K Thermometer.

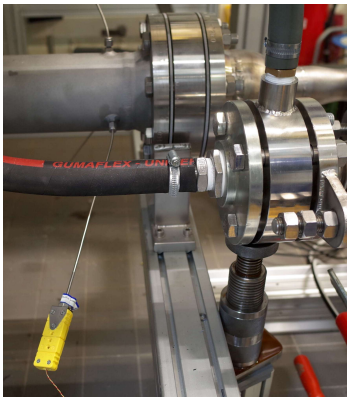

Figure 3.16: En of the heater, showing the inserted K-type thermocouple and the seeding-flange in the foreground

Figure 3.17: Alecto WS-100 weather station

The pressure of the air was indirectly measured using a mobile weather station as seen in fig. 3.17. However, since this is not a scientific measurement device, at the start day it was recorded together with three external atmospheric pressure readings of which an example is shown in table 3.2. Using eq. (3.5) the pressure for each particular run was calculated. The calibration pressure has had readings between -330 and 283 Pa.

$$P_{average} = \frac{P_{HSL} + P_{Windfinder} + P_{KNMI}}{3} \tag{3.5a}$$

Table 3.2: Pressure reading example

Source	Pressure [Pa]
HSL Portable Pressure Gauge, RUSKA 6200	101120
Windfinder, Rotterdam Airport*	101200
The Royal Netherlands Meteorological Institute (KNMI), Rotterdam**	101080
Weather station, Alecto WS-1100	100850
Calibration reading	283

*https://www.windfinder.com/report/rotterdam_airport
**https://www.knmi.nl/nederland-nu/weer/waarnemingen

$$P_{calibration} = P_{average} - P_{Alecto,t_0} \tag{3.5b}$$

$$P_{atm,\,run} = P_{Alecto,\,run} + P_{calibration} \tag{3.5c}$$

The combustion chamber however will not have the same pressure as the atmosphere, due to pressure losses in the exhaust pipe. These are around 90 Pa for the 45 m/s basic configuration, and a maximum of 360 Pa at maximum mass flow. The calculation for this was done using the Handbook of Hydraulic Resistance by Idel'chik [52]. An elaborate explanation of this calculation can be found in appendix D. These pressure losses are added to the atmospheric pressure found through the method described above to come to the pressures inside the combustion chamber.

3.3.3. SHORTCOMINGS

Like every setup, also this one has a few shortcomings that can be summarised in the following way.

- The heater of the setup is not yet connected to the DAQ&C System and can therefore not yet work under elevated temperatures. This means that also combustion cannot yet be commenced since elevated temperature experiments should first be performed. The infrastructure for both is present though.
- No accurate digital pressure transducers are present in the setup. There are already multiple holes with threads in the setup that allow for future insertion of these transducers. For the moment only the pressure in the combustion chamber is calculated using the way described above.
- Due to a too large pressure drop over the gas supply system near maximum mass flows, the pressure present at the main tank is not able delivering the maximum of the MFC's. This can be fixed when changing the diameter of the the gas supply system pipes and removing some of the sharp bends.
- When switching to elevated temperatures and reactive flow, cooling flow will be required to ensure safety of the system. At the moment there is no adequate supply of air available yet that can deliver the needed cooling flows.
- Due to the design of the burner head, seeding material shall accumulate during operation in the burner head and as such cause larger particles to enter the combustion chamber. This not only changes their Stokes number, influencing the results, it also has a higher chance of sticking to the inside of the chamber reducing optical access. Next to this, the design of the head and chamber also reduces the ease of cleaning the setup in between runs or campaigns. Possibly this could limit the number of runs possible within a campaign.

4

METHODOLOGY: PARTICLE IMAGING VELOCIMETRY

As is discussed in section 2.3, PIV has been used in this research for visualisation of the flow inside the combustion chamber. This chapter first explains what aerodynamic phenomena will be investigated in section 4.1, after this the technique behind PIV is discussed in section 4.2. The PIV setup itself is discussed in section 4.3 including the experimental campaign and image acquisition and processing in section 4.4. Lastly the error analysis and conclusions are presented in sections 4.5 and 5.8, respectively.

4.1. AERODYNAMICS OF FLAMELESS COMBUSTION

It has become clear from sections 2.1 and 2.2, that recirculating flue gases and mixing of these gases with the reactants from the jets is vital for FC. This ensures dilution and heating of the reactants, needed to obtain low peak temperatures while sustaining operation under these conditions. Therefore the recirculation zones and the influence of the jets on them shall be investigated. This section concentrates on getting a better insight in how to quantify the recirculation zones and the jet characteristics influencing entrainment of the flue gases, again influencing the recirculation zone. As can be seen, these are connected. In a short overview, thermal NO_x production is reduced by flameless combustion by:

- ⇒ Lowering the concentration of oxygen for the NO_x reaction (1)
- ⇒ Lowering the combustion peak temperature (2)
  - ⇒ (2) Operation is at lean mixtures, often comparable to conventional gas turbine combustion
  - ⇒ (1) (2) Flue gases are recirculated: lowers concentrations of reactants, lowering the heat release rate and oxygen concentration + increases the reactants temperature and enabling operation in such diluted and lean conditions.
    - ⇒ Key in sustaining this, are strong recirculation zones and mixing of the recirculating gases with the reactants through entrainment.

4.1.1. RECIRCULATION ZONES (RZ)

The recirculation ratio (RR), as stated in section 2.2.1, is an important parameter, because it is a measure of the dilution of the jet gases. If the RR goes up, relatively more flue gases are fed back to the jets with respect to combustion gases being exited by the jets. As such the concentrations of oxygen and fuel will go down and enthalpy is brought to the combustion zone. This decreases the heat release rate while operation is ensured. A higher RR will therefore indicate more successfull operation because it decreases the NO_x emissions and increases the range of operation.

To calculate the RR from the results, the mass flow of the negative air flow has to be quantified. This is calculated from the results using a velocity profile over a line. This line is at a certain axial z-location in a plane that intersects the jet from the origin. The negative velocity locations are integrated over a circle

giving a volumetric flow. When multiplied with the air density and then divided by the mass flow input from the nozzles, the RR is obtained. Equation (4.1) shows the integration method used for calculating the mass flow of the recirculated flow.

$$\dot{m}_{recirculated} = \overline{\rho} \int_{R}^{-R} \int_{\pi}^{0} U_{jet<0} r d\theta dr \tag{4.1}$$

The size of an RZ can be distinguished depending on the type of combustor. For this research is established aerodynamically, thus its singularity points (SP) indicate the size. These points indicate the beginning (usually the surface of the burnerhead) and end of the RZ. The sides of the RZ are often set by the jets. When looking at the z-velocity, a U_Z=0 line will clearly indicate this. As stated in the previous subsection, the size of the RZ influences the emissions, in the sense that a larger RZ will have larger mixing structures, lowering NO_x emissions. Clearly there is a link between the backflow velocities, the size of the RZ and the RR that needs to be researched.

4.1.2. MIXING

Mixing of the recirculated flue gases and the reactants is quantified by the entrainment of the jet and the turbulence levels in the jet flow. Where more entrainment and also cause more gases to be recirculated, connecting it to the RR. Turbulence may be quantified by looking at the velocity fluctuations and taking the root-mean-squared from this number. This is done for the z- and the y-direction. Equation (4.2e) is used to get the total of the two directions. This definition is used in the CFD software and shall therefore also be used this way with the PIV results. Since the PIV results are 2D, the fluctuations in the y- and x-direction are assumed to be equal. This assumption holds for when the jet is still axisymmetric which is the case for at least z=60mm. When normalised with the local mean flow velocity, the total RMS of the velocity fluctuations yields a turbulence intensity (TI). Equation (4.2) shows how one gets to TI from velocity fluctuations. Another way to quantify turbulence is by normalising it with the maximum jet flow velocity, where typical values range between 0.1 and 0.25[53].

$$u(t) = \overline{u} + u'(t) \tag{4.2a}$$

$$u'(t) = u(t) - \overline{u} \tag{4.2b}$$

$$Var(u') = \sigma^2 = \overline{u'(t)^2} = \overline{(u(t) - \overline{u})^2} \tag{4.2c}$$

$$u'_{rms} = \sigma = \sqrt{Var(u')} = \sqrt{\overline{u'(t)^2}} = \sqrt{\overline{u(t)^2} - \overline{u}^2}, \text{ in x-, y- and z-direction} \tag{4.2d}$$

$$u'_{rms} = \sqrt{\frac{1}{3}\left(u'^2_{rms,x} + u'^2_{rms,y} + u'^2_{rms,z}\right)} \tag{4.2e}$$

$$TI = \frac{u'_{rms}}{U_{mean}} \tag{4.2f}$$

Entrainment can be looked at in two different ways. Firstly, the entrainment can be quantified directly with eq. (4.3), where R is taken where the velocity of the jet is $u/u_0 \approx 1\%$ [53] and $\dot{m}_0$ is the mass flow inserted by the jet.

$$\dot{m} = 2\pi \int_{0}^{R} \rho u r dr \tag{4.3a}$$

$$Entrainment = \frac{\dot{m} - \dot{m}_0}{m_0} \tag{4.3b}$$

Secondly, high entrainment rates can be identified by the presence of high Reynolds shear stresses $\langle u \cdot v \rangle$ or $\overline{u'v'}$. This is a measure for the amount of transfer of streamwise momentum to the side of the jet [53]. At locations of high Reynolds shear stress, there shall be a lot of interaction between two regions of fluid with a different speed (or temperature or concentrations for that matter). The entrainment rate is extracted from the PIV results by taking the mean over a 1 cm line from z = 60 mm to z = 70 mm between y = 58 and 60 mm, depending on the location side of the jet which differs for each nozzle diameter.

4.2. FLOW VISUALISATION TECHNIQUE, PIV

The Aerodynamics Faculty of the DUT is renowned for its expertise in PIV. Much of the information presented in this section is taken from the reader of the course 'AE4180 Flow Measurement Techniques' given at the Delft University of Technology [54].

4.2.1. GENERAL WORKING PRINCIPLE

As the name Particle Imaging Velocimetry already suggests, it is a technique that analyses images of (clouds of) particles suspended in a flow in order to measure the velocity vector field often this fluid. A typical PIV setup can be seen in fig. 4.1[55].

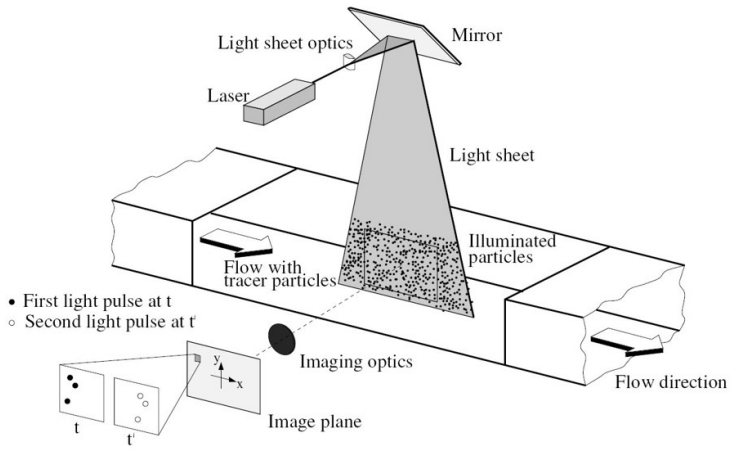

Figure 4.1: Schematic of a PIV setup

To take the image, a camera, a lense and an optical entry to the flow of interest are needed. These together dictate the possible Field of View (FOV) of the images. Since flows themselves usually don't have particles in them, so-called seed particles are added to the flow. It is important that these particles are chosen to follow the flow accurately. Then using a laser and an optical installation, the flow is illuminated for two consecutive instances with a δt time-step inbetween in the order of microseconds. The resulting two images are then processed using specific software in the following way. Each image is cut into interrogation windows and which are cross-correlated (see fig. 4.2). This interrogation windows size (IWS) is usually around $16x16$, $32x32$ or $64x64$ pixels. Together with the magnification factor the particle displacement can be found. By knowing δt and the displacement between groups of particles on the two images using cross-correlation an instantaneous vector field of the velocity can be obtained. These vector fields can then also be averaged into a generalised version of the flow including its turbulence characteristics.

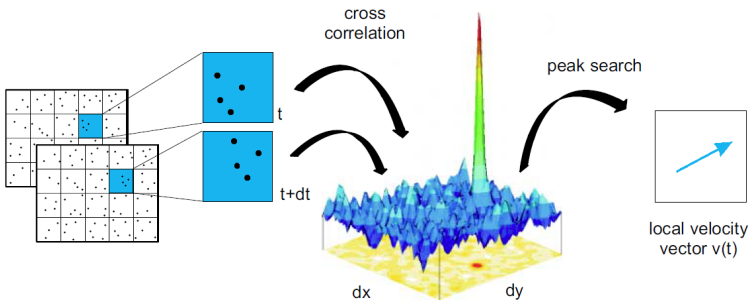

Figure 4.2: From interrogation windows, using cross-correlation to a vector [13]

4.2.2. REQUIRED COMPONENTS

To perform PIV measurements, the following components are needed in the setup and discussed here: Seeding particles, laser, camera, optics, processing software and lastly the topic of noise is discussed.

SEEDING PARTICLES

In order to illuminate the flow field seeding particles are added to the flow. These particles should adhere to a few rules:

Particle concentration When the particle concentration is too low, PIV will change into Particle Tracking Velocimetry (PTV), which is a different kind of technology. When it is too high, it will alter the fluid properties. The mass ratio should be the following, $m_{fluid}/m_{particles} = 10^{-3}$ and it should have a uniform distribution. In reality this comes down to approximately 10-20 particles per interrogation window.

Scattering ability The laser light wavelength λ, the particle diameter d_p and the index of refraction (n_p/n_f) relative to that of the fluid dictate whether or not particles are easy to be detected. Larger particles scatter more light, but shall interfere with accurate flow tracking abilities. If d_p is larger than λ, Mie's scattering can be used to approximate the diameter of the particle as seen by the camera, called the normalized diameter q, given by eq. (4.4). Since λ is usually dictated by the laser that is available, one uses the maximum particle size possible that still follows the flow well. Next to this, a higher index of refraction will also yield better scattering.

$$q = \frac{\pi d_p}{\lambda} \tag{4.4}$$

Stokes number Since PIV is an indirect technique calculating the vector field of the seeding, instead of that of the fluid, the seeding should follow the flow accurately. The Stokes number is a ratio between the characteristic time of a particle τ_p and that of the flow τ_f. Particles with a low Stokes number S_k follow the flow accurately ($S_k < 1$), those with a high number will want to continue following their initial trajectory as this is governed by their inertia ($S_k > 1$). If $S_k < 0.1$ the error in the velocity is smaller than 1%[56]. Smaller particles will yield lower Stokes numbers, but will be harder to detect as has been discussed. If a particle accelerates from one velocity to another, the characteristic time τ is the time it takes to increase with 63.2% ($1 - e^{-1}$) of the velocity difference. Equations for the Stokes number are given in eq. (4.5), where μ is the dynamic viscosity of the fluid, L_f is the flow length scale and ΔU this velocity difference. This shows that smaller particles, with low densities in a viscous fluid follow the fluid best for a certain fluid flow state.

$$S_k = \frac{\tau_p}{\tau_f} \tag{4.5a}$$

$$\tau_p = d_p^2 \frac{\rho_p}{18\mu} \tag{4.5b}$$

$$\tau_f = \frac{L_f}{\Delta U} \tag{4.5c}$$

Hazards The chosen seeding material should not be hazardous for the environment, nor a person or protective measures should be taken.

Operating temperature For room temperatures, often a glycol-water based fog is used. In case of operating under elevated temperatures, the seeding particles should keep their good characteristics and not melt, evaporate or stick together. However, since this research is limited to room temperature flows, this is not an issue.

LASER

Four main requirements adhere to choosing the correct laser: pulse duration, pulse pair frequency, repetition rate and pulse intensity.

Pulse duration The laser pulse should be short in order to let the seeding particles appear as dots and not as streaks. In practice this means that within this pulse duration the particle should move a distance significantly smaller than its own size.

Pulse pair frequency The pulse frequency is dictated by the cross-correlation technique. Time between two pulses δt should be large enough for the image pairs to be different, but small enough for the cross-correlation to still find the particle patterns in both pictures close to each other. In reality δ_t

will need to be such that the particle displacement is a maximum of $\frac{1}{4}$ of the interrogation window size, so this depends on the maximum flow velocity. For higher displacements, the processing will need to be differently, yielding less accurate results.

Repetition rate In case one wants a time-resolved experimental results, the repetition rate of the laser (as well as the camera) will need to be in the order of kHz. In case this is not needed, repetitions rates in the order of 0.5 - 100 Hz could be used. Different laser techniques yield different rates as can be seen in table 4.1.

Pulse energy The laser intensity should be high enough to let the light scattered by the particles be detected by the camera. Approximately an energy of 100 mJ per $10x10cm^2$ is required for airflows.

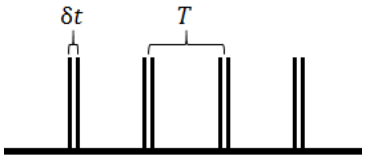

Figure 4.3: Timing of the exposures

Table 4.1 shows the specifications of the two types of lasers used for PIV applications: Nd:YAG (neodymium-doped yttrium aluminium garnet) and Nd:YLF laser (neodymium-doped yttrium lithium fluoride). Since this research is not focused on time-resolved results and the available Nd:YAG laser is much smaller and thus easier to handle, this is the laser that is used. Its pulse duration is around 5-10 ns, hardly limiting the flow speed. These kind of laser have two separate lasers in them, both firing at the required time, allowing to make image pairs very close to each other.

Table 4.1: Laser type properties

Laser type	λ [nm]	Pulse duration [ns]	Repetition Rate [Hz]	Pulse energy [mJ]
Nd:YAG	532	5 - 10	0 - 50	10 - 1000
Nd:YLF	526	50- 100	1000 - 5000	10 - 30

CAMERA

Figure 4.3 shows the two different light pulses that need to be captured in two different images. This is done using a CCD sensor inside a camera. The timing of the exposure is important to get sharp images and to have exact information on the time difference between the two pictures, needed to calculate the flow speed. This is therefore done with an external synchronizer. The camera can take these image pairs a few times per second. Often, the camera sensor architecture allows readings that do not facilitate the required δt value to become sufficiently small. Therefore an *interline transfer CCD* architecture has been developed which allows for storage of the first reading of a pair and then letting the sensor read one pair per time during the time of T. This way, δt can become sufficiently small. T, as shown in fig. 4.3, is then still limited by the actual processing speed of the camera.

OPTICS

The optics involved in PIV have two different tasks. Firstly, optics are needed to change a laser beam into a sheet at the desired location and secondly, to correctly portray the image of the laser sheet in the combustion chamber onto the camera sensor. For the first task two things need be taken in to account. One can choose to produce a laser sheet with constant width or one width a linearly expanding width. What is preferred depends on the application. Also, the two laser pulses should create a laser sheet with an overlap of at least 80% to create accurate measurements.

To correctly portray the laser sheet image on the camera, one has to correctly work with lense focal lengths, object and camera distances, magnification and f-stop. The definition of these optical parameters is defined in fig. 4.4 The thin lense equation relates the focal length f with the object d_o and image

d_i distances (see eq. (4.6a)), and these two distances also make up the magnificiation factor M (shown in eq. (4.6b)). F-stop $f\#$ is needed to know the focal depth δz, the distance over which the particles are still in focus (see eqs. (4.7a) and (4.7b), where D is the aperture of the camera). The focal depth is important in making sure that the whole laser sheet is in focus and not just parts of it.

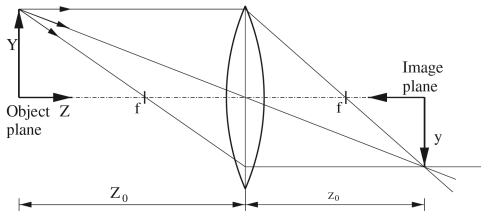

Figure 4.4: Thin lense schematic [14]

$$\frac{1}{f} = \frac{1}{d_i} + \frac{1}{d_o} \quad (4.6a) \qquad M = \frac{d_i}{d_o} = \frac{sensor\ size}{imaged\ object\ size} \quad (4.6b)$$

$$f\# = \frac{f}{D} \quad (4.7a) \qquad \delta z = 4.88\lambda f\#^2 \left(\frac{M+1}{M}\right)^2 \quad (4.7b)$$

Lastly, the diffraction pattern should be taken into account to get a sharp image. Due to diffraction, the geometrical size of the particle image on the sensor, will be different from what the sensor will be measuring. d_{geom} is the geometrical size of the particle on the sensor, shown in eq. (4.8a). The image size of the diffraction pattern of the particles is d_{diff} and shown in eq. (4.8b). The actual image size is a combination of the two and is approximated with a Euclidian sum, shown in eq. (4.8c). This also shows that for extremely small particles, the captured diameter is close to the diffraction pattern instead of the geometrical size.

$$d_{geom} = M \cdot d_p \quad (4.8a) \qquad d_{diff} = 2.44\lambda(1+M)f\# \quad (4.8b) \qquad d_\tau = \sqrt{M^2 d_p^2 + d_{diff}^2} \quad (4.8c)$$

PROCESSING SOFTWARE

To process all these images taken by the camera, a software package is used to cross-correlate the images and turn them into vector images (see fig. 4.5 for an example). The software can also create mean and root mean squared images of the input. This way much more information can be taken from the images than just its instantaneous vector field. Next to the fact that the particles should not move more than $\frac{1}{4}$ of the an interrogation window, they should also not move forward or aft inside the laser sheet with more than $\frac{1}{4}$ of the laser sheet thickness, or else the software cannot correlate them well anymore.

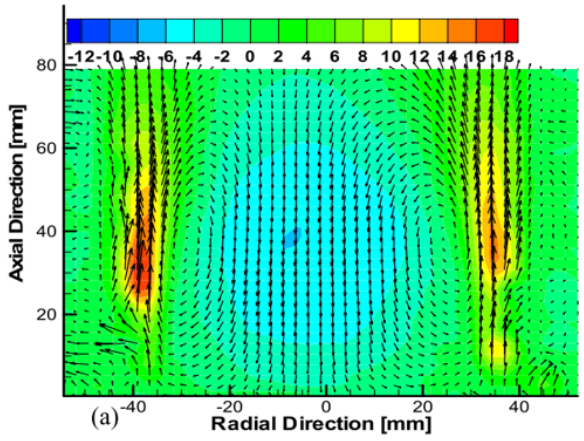

Figure 4.5: Axial velocity contours of a FLOX® burner as captured by PIV [15]

NOISE

It is important to diminish noise from light-sources other than the laser sheet, when performing PIV measurements. These can be reflections from surfaces in the room, light sources such as a computer, a small light or a hole in a blinder letting through sunlight. When operating at elevated temperatures, this can also be broadband light emissions from hot radiating sources. To diminish these effects, one has to be very careful with the positioning of reflective surfaces, darkening a room and perhaps use wavelength filters to filter out any other wavelengths than that of the laser. Noise can also be reduced afterwards in the processing, however, this will always also lead to a loss of information and is undesired.

4.2.3. CONCLUSION

What can be concluded from this section on the PIV measurement technique is that it is not easy in preparation and operation, but can give results that are otherwise hard to obtain. Many factors should be taken into account and thought of carefully on beforehand. In short these are the (dis)advantages:

+ It allows for capturing a large area of a flow field
+ It is a quantitative measurement
+ It is non-intrusive, thus not influencing the flow field
+ No calibration measures are needed
– Optical access is required
– Preparation of and setting up the technique is complicated
– Only a low temporal resolution is possible
– Spatial resolution is very dependent on setup equipment

For closed setups this technique gives challenges. Seeding particles deposit against the sides of the volume and influence the aerodynamics and thus require regular cleaning [42].

4.3. PIV SETUP

In this section all the equipment used in this PIV setup is specified. Also an overview of all the relevant PIV parameters is given.

4.3.1. EQUIPMENT

The equipment used in this experiment has been chosen from a variety of equipment present at the Aerodynamics facilities of the DUT.

SEEDING PARTICLE GENERATOR

The PIVTEC Aerosol Generator working with DEHS oil has been used to provide seeding (see fig. 4.7). Titaniumdioxide was also present to be used as a seeding material, however this is toxic and required extra handling measurements. Theatrical smoke was also present, however this needs to be able to expand after exiting the apparatus, which was not possible in this setup. As such, DEHS oil was the preferred solution. The droplet size of the seeding generated by this apparatus is ca. 1 mm for DEHS oil (see fig. 4.6).

The seeder has a remote control (see fig. 4.8), which allows for remotely setting the number of nozzles that are open, controlling the amount of seeding. More open nozzles does not only mean more seeding, but also more airflow, so this has been taken into account when setting the required air flow from the gas supply system. Next to this, a metallic cylinderically shaped device can be seen on top of the seeder, called the impactor. This filters out droplets that are too large in size, improving the Stokes number of the seeding. Especially for this setup the impactor is important since this reduces the accumulation of DEHS oil inside the burner head.

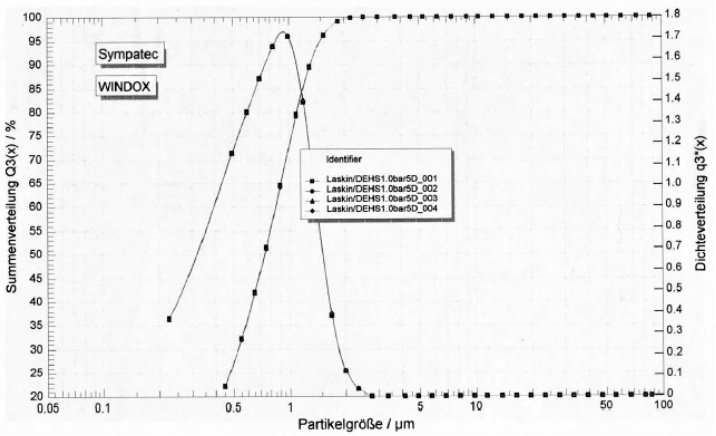

Figure 4.6: Probability density function and cumulative distribution function of the seeding particle size

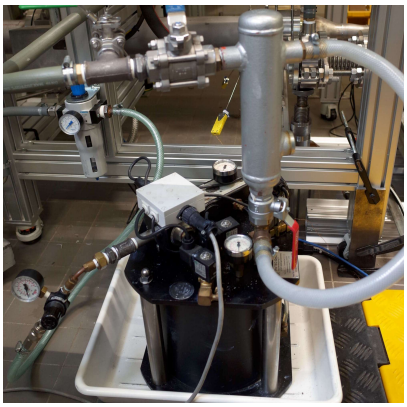

Figure 4.7: The PIVTEC Aerosol Generator including the impactor

Figure 4.8: Remote control unit for the PIVTEC Aerosol Generator

ND:YAG LASER

A Quantel Evergreen 200 Nd:YAG dual pulsed laser has been used as the source of illumination for the PIV experiments. It generates a beam with a wavelenth of 532 nm and a maximum of 200 mJ per pulse at 15 Hz and a beam diameter of ca. 5 mm. The laser head itself is accompanied by a power supply, cooling station and control unit that can be seen in fig. 4.9. The laser itself is therefore compact and can be positioned inside the setup together with an array of optics to shape this laser beam into a divergent lasersheet that will illuminate a plane inside the combustion chamber (see fig. 4.10).

Figure 4.9: Power supply, cooler and control unit for the Quantel Evergreen laser

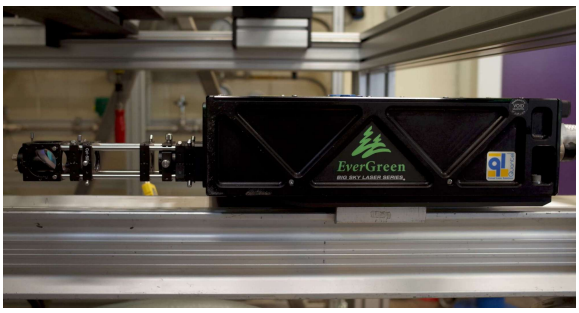

Figure 4.10: Quantel Evergreen 200 Nd:YAG laser head, togethr with its array of lenses and a mirror, positioned inside the setup

LAVISION CAMERA

The camera used in these experiments is a LaVision Imager Pro LX 16M, with a resolution of 4872x3248 and a pixel size of 7.4x7.4 μm (see fig. 4.11). It has a maximum frame rate of 3 Hz and a $\delta t < 1 \mu s$. Two of them have been used, with two different lenses to also enable a close-up zoom-case of the jet nozzle. As such the jet exit velocity profile and jet spreading can be investigated more accurately. The minimum T attainable between two image pairs for this camera at full resolution was 1.25 s or 0.8 Hz. This makes it impossible to obtain time-resolved PIV results.

The high resolution was needed to compensate for the large Field of View (FOV) of the setup of 240x160 mm, to still have a spatial resolution of 412 pixels per mm^2 or 20.3 pixels per mm. Which is needed to capture phenomena with sizes of around 1.5 mm when using interrogation windows of 32x32 pixels in size. This way, approximately 4 interrogation windows are present for the smallest jet nozzle, which means it will still be able to capture the velocity profile. For the zoom-case with an FOV of 75x50 mm, this led to 65 pixels per mm, capturing phenomena of around 0.5 mm in size, yielding a three-fold increase in spatial resolution. Please find an overview of these parameters for the different cases as well in table 4.3.

Figure 4.11: The LaVision Imager Pro LX 16M camera with an f=105 mm lense

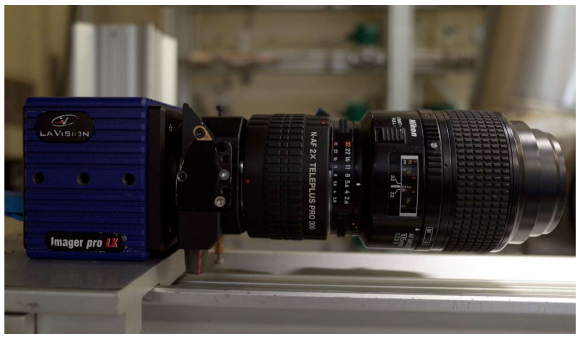

Figure 4.12: The Lavision Imager Pro LX 16 camera with an $f_{effective}$=210 mm lense, used for the zoom-case

LENSES AND DISTORTION

Both lenses had a focal length of 105 mm, but for the zoom-case a lense-multiplier was added, effectively making it a 210 mm lense (see figs. 4.11 and 4.12). For both lenses focusing was done at the smallest D of 2.6 and then enlarged to 5.6 capture more light and increase the focal depth. The choice for an f = 105 mm lense was made based on the comparison between different lenses as shown in figs. 4.13 to 4.15. From this it can be seen that the f = 35 mm lense has a large radial distortion around the edges, a fisheye-effect, and the f = 60 mm lense also still effect and starting from the f = 105 mm this is not present anymore. Going to larger focal lengths would require the cameras to be too far away from the setup, making them impractical.

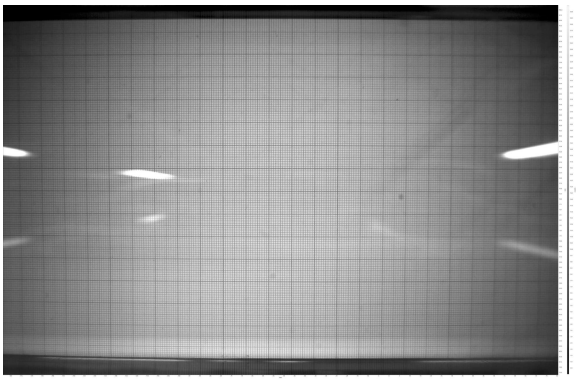

Figure 4.13: Image using an f = 35 mm lense

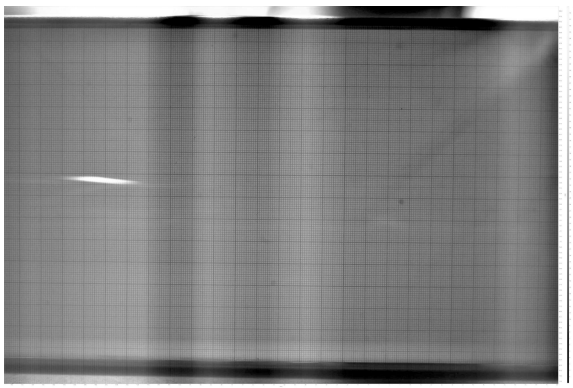

Figure 4.14: Image using an f = 50 mm lense

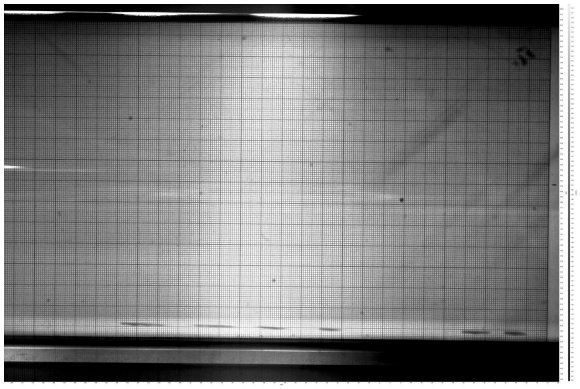

Figure 4.15: Image using an f = 105 mm lense

Next to distortion from the focal length of the lense, also distortion from the transparent cylinder is present due to the refractive index differences between this material and the air and the material thickness. The influence of this has been investigated as well, by taking an image of millimeter paper inside the cylinder in the final setup and counting the number of pixels that go into one millimeter on the paper. The final result of this is shown in fig. 4.16. Note that the counts are done at different axial locations, namely near in the middle and at 10% from the left and right edges of the FOV. This was done to identify if the distortion was any different near the side of the image. At each of these axial lines, the top and bottom 10 mm and the middle 5 mm of the image has been counted (see fig. 4.17). Figure 4.16 only shows the result for the middle of the cylinder, the full result is shown in appendix E.

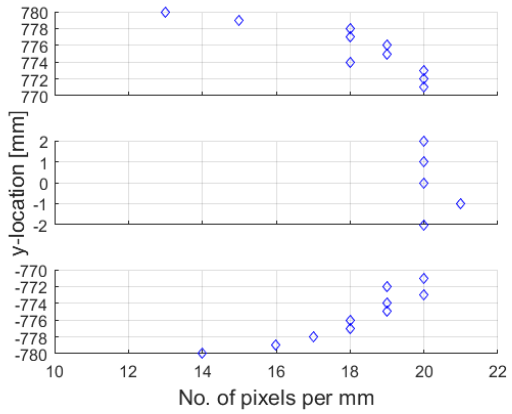

Figure 4.16: Distortion of the image due to the curve and thickness of the transparent cylinder, over the midline of the FOV

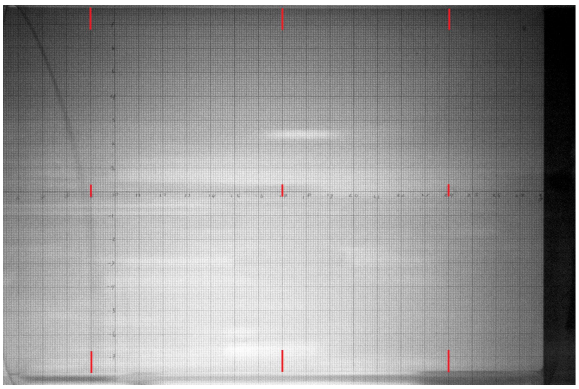

Figure 4.17: A calibration image showing the locations of where the distortion measurements have been taken

PROGRAMMABLE TIMING UNIT (PTU)

To coordinate triggering the laser pulse and the camera exposures a LaVision PTU has been used, in combination with the LaVision software This PTU is shown in fig. 4.18.

Figure 4.18: The LaVision Programmable Timing Unit

REFLECTION REDUCTION

Early in the experimental campaign it became clear that some of the reflections saturated the image and would as such distort the final results. Therefore a few precautions were taken to prevent these reflections from happening as much as possible. The burnerhead and the nozzles have been painted black (see fig. 3.5) and a piece of black theatre-cloth absorbs the laser sheet on the fume hood (see fig. 4.19). A wooden plank with a slit was used to stop the reflections from the lasersheet that are reflected from the bottom of the cylinder (see fig. 4.20). The final results still portray reflections sometimes, however, these are due to the crazing of the inner surface of the acrylic cylinder which caused internal reflections of the laser beam, which could not be taken away. These tiny cracks are likely to have grown from the use of the DEHS seeding oil.

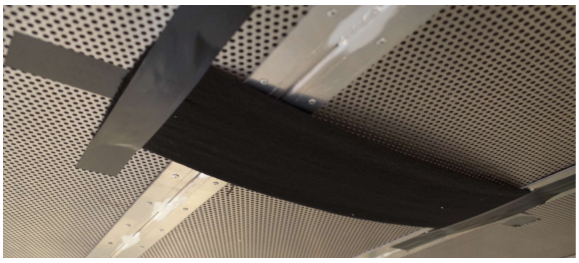

Figure 4.19: Black theatre-cloth attached to the fume hood to prevent reflections

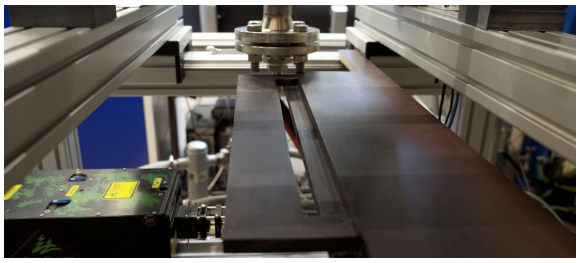

Figure 4.20: A black wooden plank with a slit, used to prevent interference from reflections from the bottom of the cylinder

4.3.2. EXPERIMENTAL CAMPAIGN AND PARAMETERS

Table 4.2 gives an overview the different runs within the experimental PIV campaign. It shows which combinations of variables has been used from the ones mentioned in section 3.2.3. The combination depicted in **bold** is the **'basic configuration'**. In case the configuration is not mentioned in one of the results, this is the one to be assumed. This was chosen because a length of 2.25 D, would most certainly not interfere with the recirculation zone. A nozzle diameter of 8.45 mm allows for high enough velocities, while also giving an acceptable spatial resolution on the jet exit velocity profile. Lastly, 45 m/s was chosen because this result turned out to have the cleanest picture (least interference from reflections).

Table 4.2: Experimental campaign

Run	Plane	Chamber length [–]	Nozzle d $[mm]$	U_{jet} $[m/s]$								
1	A	1.5 D	8.45	15	30	45	60					
2		**2.25 D**	6.67	15	30	45	60	75	90	105	120*	135*
3			**8.45**	15	30	**45**	60	75				
4			11.0	15	30	45						
5	B	2.25 D	6.67	15	30	45	60	75	90	105		
6			8.45	15	30	45	60	75				
7			11.0	15	30	45						
8	ZOOM	2.25 D	8.45	15	30	45	60	75	90**			

**This result has a too small ensemble size due to oil interference to take into account quantitatively*
***This result is spoilt by limitations on the equipment and should only be used for quantitative analysis*

It may seem arbitrary that Run 1 only goes up to 60 m/s while Run 3 goes to 75 m/s and Run 8 went up to 90 m/s, all for the same configuration. The reason for this is that either the results for higher velocities have been discarded due to too much oil interference or due to a time constraint in the campaign. A clear overview of all the experimental parameters with which this PIV campaign has been run is given in table 4.3.

Table 4.3: Experimental parameters

Parameter	Unit	Value	
		Plane A / B	*ZOOM*
Stokes number		0.0167 - 0.247	
Focal length $[mm]$	mm	105	205
Aperture	mm	5.6	5.6
f#		18.75	37.5
Pixel size	μm	7.4	
Image resolution	$pixels$	4872 x 3248	
FOV, wxh	mm	240 x 160	75 x 50
Magnification factor		0.15	0.48
Acquisition frequency	Hz	0.8	
dτ	μs	6 - 30	6 - 10
Ensemble size		400	
Run time	min, s	8, 20	
Laser power	%, mJ	100/100, 200	
Interrogation window	$pixels$	32 x 32	
Digital resolution	$pixels/mm$	20.3	65
Vector spacing	$pixels$,mm	8, 0.4	8, 0.12

What should be noted from these parameters, is that the Stokes number is higher than 0.1 for some of the experimental runs. The effect of this shall be treated in section 4.5. Also, during the runs a few problems occured that are helpful to know for future reference. Over time, crazing of the inner acrylic surface will happen, causing reflections that cannot be taken away. Due to the shape of the burnerhead and the long run time, oil accumulates inside the burnerhead and is then taken by the jet into the combustion chamber, interfering with the laserlight and obstructing the camera view.

4.4. IMAGE ACQUISITION AND PROCESSING

Aqcuisition of the images was done using Davis 8.4 software and the equipment stated in the previous section. To ensure a correct jet velocity in the results, a test run of 10 images was always taken first and processed with quick parameters. From this is became clear that because of the boundary layer inside the jet, the effective nozzle diameter decreased between 5% and 15%. The exact values for this per case can be found in appendix F. With the right settings, a run was performed taking 400 images. Due to oil interference, the cases for 105 m/s and 135 m/s are made up of two sets of data, in the end still comprising of 400 images. Next to this, problems arose with the δt that could not be lowered below 6 μs. As such, the maximum pixel displacement was higher than 10 and for the 90 m/s case in Run 8, it became as high as 34 pixels. The next section shall explain how this anomaly was dealt with.

After data acquisition, the Davis 8.4 software was used to process this. Table 4.4 shows the vector calculation processing parameters used. Also the parameters used for the special cases are portrayed.

Table 4.4: Vector calculation in data processing, using a multipass decreasing in size

	Max Δpx	Window size	Weight	Overlap	Passes
Normal	< 15	64 x 64	1:1 □	50	1
		32 x 32	1:1 ○	75	3
Run 8, 45 m/s	17	96 x 96	1:1 □	50	1
		32 x 32	2:1 ⬭	75	3
Run 8, 60 m/s	23	128 x 128	1:1 □	50	1
		32 x 32	4:1 ⬭	75	3
Run 8, 75, 90 m/s	28, 34	256 x 256	1:1 □	50	1
		32 x 32	4:1 ⬭	75	3

4.5. ERROR ANALYSIS

There are many different sources of error in PIV measurements and these shall be highlighted in this section. Firstly, the statistical error involved when working with a finite ensemble size and secondly the three main sources of error from the PIV measurement itself. Lastly, the errors from environmental measurements are treated. Note that the results themselves shall not be presented in the subsections, but are summarised at the end in table 4.7.

4.5.1. FINITE ENSEMBLE SIZE

Three result taken from the PIV measurements shall be the mean velocity, the RMS velocity fluctuations and the Reynolds Shear Stress (RSS). The influence of the finite ensemble size on their uncertainty was improved by Benedict and Gould[57] and discussed by Sun[58]. The errors of mean velocity, the RMS velocity fluctuations and RSS are displayed by eqs. (4.9) to (4.11), respectively.

$$\epsilon_{\overline{u}} = \frac{\sqrt{\overline{u'^2}}}{\sqrt{N}} = \frac{u'_{rms}}{\sqrt{N}} \tag{4.9}$$

$$\epsilon_{u'_{rms}} = \frac{\sqrt{\overline{u'^2}}}{\sqrt{2N}} = \frac{u'_{rms}}{\sqrt{2N}} \tag{4.10}$$

$$\epsilon_{\overline{u'v'}} = \frac{\sqrt{1+R_{uv}^2}\sqrt{\overline{u'^2}}\sqrt{\overline{v'^2}}}{\sqrt{N}}, \quad \text{with} \quad R_{uv} = \frac{\overline{u'v'}}{\sqrt{\overline{u'^2}}\sqrt{\overline{v'^2}}} \tag{4.11}$$

In these equations, ϵ is the error, N the ensemble size, u is the velocity, u'_{rms} is the RMS of the velocity fluctuations and R_{uv} is the correlation coefficient. The general depiction of this error is ϵ_N.

4.5.2. PIV MEASUREMENT

This subsection treats the sources of errors originating from the PIV technique itself, namely, cross-correlation, seeding particle lag and a finite spatial resolution.

CROSS-CORRELATION

The cross-correlation technique used to extract the vector field from the images gives rise to an error as well which can be quantified using eq. (4.12), noting that ϵ_{corr} for planar PIV is 0.1 $pixels$. In eq. (4.12), k is the digital image resolution in $pixels/mm$ and δt is the time between two pulses in ms (see fig. 4.3). This parameter will be the largest for Runs 1-7 at the smallest δt of 6μs, so this one will be portrayed.

$$\epsilon_{cc} = \frac{\epsilon_{corr}}{k\delta t} \tag{4.12}$$

SEEDING PARTICLE LAG

As was discussed in section 4.2.2, the Stokes number of the seeding particles should be low enough to make sure it's own inertial forces do not interfere to much with the direction of the flow field. Even still, the particle will have a lag in following the flow velocity field and the difference between de particle and fluid velocity is called the slip velocity u_{slip}, which is estimated in the following way. Equation (4.13) shows how it can be approximated [58], where τ_{slip} is the particle response time and a_p the particle acceleration. For DEHS oil, τ_{slip} is in the order of 2 μs [59].

$$u_{slip} \approx \tau_p a_p \tag{4.13}$$

To define the particle acceleration eq. (4.14a) can be used, which assumes the density of the particle to be much higher than that of the fluid (which is the case for this experiment)[60]. However this can again be simplified to eq. (4.14b), when steady flow is assumed[59].

$$a_p = \frac{du_p}{dt} = \frac{u_p - u_f}{\tau_p} \tag{4.14a}$$

$$a_p = \mathbf{U}\cdot\nabla\mathbf{U} \tag{4.14b}$$

Substitution results in eq. (4.15). It should be noted that this approximation is only valid in the absence of strong vortices. In the presence of this, the centrifugal force would be the main contributor of slip, however these regions are not the focus of this research.

$$u_{slip} \approx \tau_p \cdot (\mathbf{U} \cdot \nabla \mathbf{U}) \tag{4.15}$$

The $\nabla \mathbf{U}$ parameter has been taken from the Davis software package. It turned out that the results for Run 8 (the ZOOM-case) were most accurate for this. Therefore, this uncertainty analysis only applies to runs up to 75 m/s. The results for this can be found in table 4.5 for the different velocities.

Table 4.5: Particle slip uncertainty for τ_{slip}=2μs

Case $[m/s]$ $[m/s]$	U$_{jet,PIV}$ $[m/s]$	2D Divergence, x-y $[1/s]$	U$_{slip}$ $[m/s]$	Uncertainty $[-]$
15	14.5	800	0.023	0.2%
30	31.5	1800	0.11	0.4%
45	43.8	2500	0.22	0.5%
60	58.5	3500	0.41	0.7%
75	71.1	4300	0.61	0.9%

FINITE SPATIAL RESOLUTION

This spatial resolution uncertainty originates from the fact that the velocity is averaged within an interrogation window. Any fluctuations within this window will not be measured and this will give a difference between the real local velocity and the measured local velocity. The ratio between the interrogation window size WS and the size of the flow structures one wants to resolve λ determines this spatial resolution uncertainty. This ratio is also known as the normalised window size l^* and is depicted in eq. (4.16a). It may be clear from this that this uncertainty is dependent on the size of the structures of interest. Runs 1-7 have $WS = 1.6mm$ and Run 8 has $WS = 0.5mm$. For a one-iteration method, the error can then be estimated using eq. (4.16b)[16].

$$l^* = \frac{WS}{\lambda} \tag{4.16a}$$

$$\epsilon_{sp} = 1 - \frac{u_{meas}}{u_{real}} = sinc(l^*) \tag{4.16b}$$

However, a total of 4 iterations is performed in each of the cases for in this research, giving rise to a different function, namely that of fig. 4.21 for 1D flow structures (shear layers) and that of fig. 4.22 for 2D flow structures (such as vortices). Table 4.6 then gives the estimated errors for different normalised sizes for 1D and 2D, taken from these figures. To stay within a 1% uncertainty, for 1D structures $\lambda = 3.5mm$ for Run 1-7 and $\lambda = 1.25mm$ for Run 8. This means the mean velocity profile can be accurately taken from Run 1-7 and the shear layer can be accurately taken from Run 8. For 2D structures $\lambda = 7.3mm$ for Run 1-7 and $\lambda = 2.27mm$ for Run 8. This means the stagnation points of the vortex structures can be accurately taken from Run 1-7 and in instantaneous images larger vortex structure can be accurately identified from Run 8.

Table 4.6: Spatial resolution uncertainties for different flow structure sizes for 1d$_{nozzle}$ and 2d$_{nozzle}$

l*, 1d	Uncertainty	l*, 2d	Uncertainty
0.5	4%	0.5	30%
0.4	1%	0.25	2%
0.25	0%	0.22	1%
0.1	0%	0.1	0%

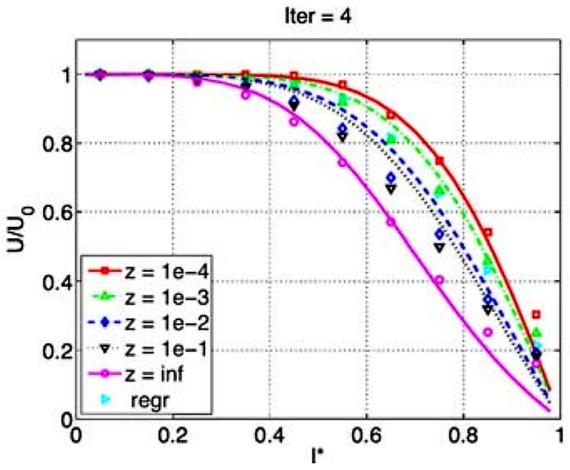

Figure 4.21: Quantification of the spatial resolution uncertainty for a 1D fluctuation after 4 iterations is given by the light blue regression line[16]

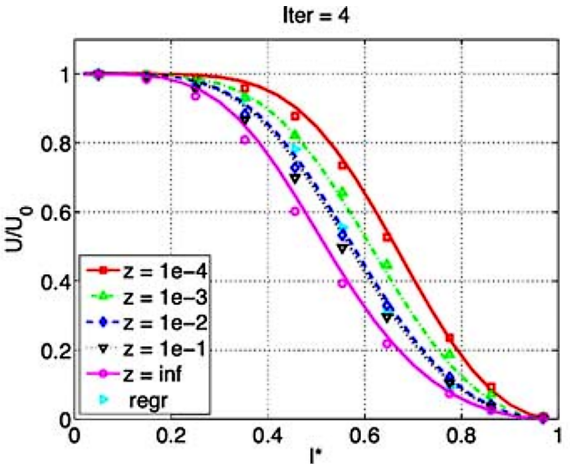

Figure 4.22: Quantification of the spatial resolution uncertainty for a 2D fluctuation after 4 iterations is given by the light blue regression line[16]

4.5.3. ENVIRONMENTAL ERRORS

As specified in section 3.3.2, the pressure measurement is not very accurate and will have an error. The largest impact of this is on the calculation of the actual volume flow based on the normalised and standardised ones. However, the uncertainty occuring from an error of +/- 500 Pa is <0.5% which is thus deemed negligible. The error in the temperature reading will be much smaller because it is measured right before the combustion chamber with a calibrated thermocouple. The uncertainty originating from an error of +/- 1 K is only <0.4%, and therefore this uncertainty is also deemed negligible. The calculations for this can be found in appendix C.

4.5.4. TOTAL ERROR

All individual errors discussed before are summarised in table 4.7. The cross correlation error is dependent on the digital image resolution and the time between two pulses and would therefore need different errors for the different runs and velocity cases. However, for the smallest δt and the worst resolution, the error is still only 0.0001% and thus negligible. Therefore it is portrayed as 0% for all cases. Also the particle slip uncertainty differs for the different cases, for the total uncertainty, the largest one is taken. In the last two rows, the total error for both parts is calculated using the standard error propagation relation stated in eq. (4.17).

$$\epsilon_{total} = \sqrt{\epsilon_N^2 + \epsilon_{cc}^2 + \epsilon_{slip} + \epsilon_{sp}} \tag{4.17}$$

Table 4.7: Overview of sources of uncertainty and their results

Uncertainty source	Percentage
Ensemble size, $\epsilon_{\overline{u}}$	1.25%
Ensemble size, $\epsilon_{\langle u' \rangle}$	0.88%
Ensemble size, $\epsilon_{\overline{u'v'}}$	0.32%
Cross-correlation, ϵ_{cc}	0%
Particle slip, ϵ_{slip}	0.2-0.9%
Spatial resolution, ϵ_{sp}	1%
Total uncertainty, mean $\epsilon_{total,\overline{u}}$	1.8%
Total uncertainty, rms $\epsilon_{total,u'_{rms}}$	1.6%
Total uncertainty, rss $\epsilon_{total,\overline{u'v'}}$	1.4%

4.6. CONCLUSION, STRENGTHS AND LIMITATIONS

PIV is an excellent technique to investigate the flow structures **inside** the DUT Flameless Combustor Setup without interfering with the flow. Due to the excellent equipment that was available, also a setup with a ZOOM-case on the nozzle exit was possible. This gives a higher accuracy when looking at the jet exit velocity profile. Processing of the data has been a long process due to the large ensemble size of 400 images and the use of 16 MP cameras, but it does allow for correction of some of the reflections. Due to the use of an acrylic cylinder, some reflection problems grew over time and the outer 7mm of the results should only be analysed qualitatively, not quantitatively. The total uncertainties of the velocity field, the RMS and RSS are only 1.8%, 1.6% and 1.4% respectively, which is low. However, this should still be taken into account when analysing the results.

5

METHODOLOGY: COMPUTATIONAL FLUID DYNAMICS, CFD

Computational Fluid Dynamics (CFD) can be a powerful tool when investigating flows, when used correctly. It allows the user to perform experiments without the need of time-consuming and expensive real-life setups and experiments. Especially with the enormous increase in attainable computational power the last few years, accurate CFD models are possible for many different types of applications. Running these simulations requires the use of models, which are suited for different flows cases. It is therefore important to validate CFD results with real life results. Once a validated model has been obtained, it can be used to predict what real-life situation would do and reduce the need for real-life experiments or target them better. A CFD solution also allows the user to look into the flow in 3D, something is a complex thing to realise in a real-life experiment.

This research has used two software packages from ANSYS, namely, ICEM 18.2 for building the mesh and FLUENT 18.1 as the solver. The latter was chosen instead of CFX, since Fluent is better at combustion CFD and this analysis would therefore enable a better continuation of the research. This chapter first explains the mathematical basis behind Reynols Averaged Navier-Stokes (RANS) analyses in section 5.1, then the numerical setup used in sections 5.2 to 5.6, then the parameters that will be investigated in section 5.7 and lastly present the conclusion in section 5.8. The numerical setup is split up in a discussion of the turbulence models in section 5.2, the computational domain in section 5.3, the boundary conditions in section 5.4, the near-wall treatment in section 5.5 and lastly the solver settings in section 5.6.

5.1. REYNOLDS AVERAGED NAVIER-STOKES EQUATIONS

The continuity and Navier-Stokes equations are used by CFD to compute the flow in the domain. Their general forms are given by eqs. (5.1) and (5.2), respectively[61]. The continuity equation is based on the conservation of mass. This states that the mass entering a system should be equal to the mass exiting the system plus the mass that stays within the system. The Navier-Stokes equation is based on conservation of momentum, of which the result will be a velocity field. It states that a change in momentum (LHS of eq. (5.2)) should be equal to the sum of external forces acting on it (RHS of eq. (5.2)). The external forces taken into account are pressure forces $\vec{\nabla} p$, viscous forces $\vec{\nabla} \cdot \tilde{\tau}$ and external body forces causing body accelerations $\rho \vec{g}$.

$$\frac{\partial}{\partial t}(\rho) + \vec{\nabla} \cdot (\rho \vec{v}) = 0 \tag{5.1}$$

$$\frac{\partial}{\partial t}(\rho \vec{v}) + \vec{\nabla} \cdot (\rho \vec{v} \vec{v}) = \left[-\vec{\nabla} p + \vec{\nabla} \cdot \tilde{\tau} + \rho \vec{g} \right] \tag{5.2}$$

In these equations ρ is the density, $\vec{\nabla}$ the mathematical operator for divergence, $\vec{v}$ the velocity vector, p pressure, $\tilde{\tau}$ the viscous stress tensor and $\vec{g}$ the body accelerations.

Solving these equations precisely, is computationally expensive. Therefore the Navier-Stokes equations are averaged and the pressure and velocity terms are split up into a mean and a fluctuation part. The solution becomes time-independent and therefore much less computationally expensive. However, averaging the Navier-Stokes equation brings up an unclosed term called the Reynolds stress tensor, which is seen as the last term in eq. (5.3). Different turbulence models have been developed to model this term and are discussed in the next section, section 5.2.

$$\frac{\partial}{\partial t}(\overline{\rho}\tilde{u}_j) + \frac{\partial}{\partial x_i}(\overline{\rho}\tilde{u}_i\tilde{u}_j) = \left[-\frac{\partial}{\partial x_j}\overline{p} + \frac{\partial}{\partial x_i}\overline{\tau_{ij}} + \overline{\rho}g_j\right] - \frac{\partial}{\partial x_i}\left(\widetilde{\overline{\rho}u_i''u_j''}\right) \tag{5.3}$$

5.2. TURBULENCE MODELS

To solve the unclosed term from the RANS equation, two different approaches have been developed. The more simple two equations models (k-ϵ and k-ω) and the Reynolds Stress Models (RSM). The former two models are more simple because they relate the turbulent stress tensor to the mean strain rate tensor in the Boussinesq isotropic eddy viscosity assumption[62]. These models state that the Reynolds stress tensor is a function of the mean strain rate tensor and the so-called eddy viscosity μ_t. A general note to go with all these models is the following. In the equations of these models, constants are present that have to be set by the user. A default set of constants has been researched by ANSYS to work best in most cases, but these can of course be changed when one thinks this could improve their case.

5.2.1. K-ϵ

This model was first proposed by Launder and Spalding[63] and has a high robustness, economy and acceptable accuracy for many flows. It is a semi-emperical model and is a model based on transport equations for the turbulent kinetic energy k and the turbulent dissipation rate ϵ. These two variables are used to calculate the eddy viscosity. In the derivation for this model, the assumption is made that the flow is fully turbulent and molecular viscosity effects are negligible, it is thus only valid in fully turbulent flows. To improve upon the weaknesses of the Standard version of this model, the RNG and Realizable model have been developed. The RNG variant supplies better solutions for rapidly strained flows, swirling flows and accounts better for low-Reynolds number effects. The Realizable model contains a new formulation of the turbulent viscosity and has an improved new version of ϵ-equation. As such it more accurately predicts the spreading rate of both planar and round jets and performs better in flows involving rotation.

5.2.2. K-ω

This model is based on the k-ω model from Wilcox[64]. It is an empirical model and where calculation of the eddy viscosity is based on the transport equations for the turbulent kinetic energy k and the specific dissipation rate ω (that can be seen as the ratio of $\frac{\epsilon}{k}$). It is a model that also takes low-Reynolds number effects into account, compressibility and shear flow spreading. Therefore it can also resolve the boundary layer, taking away the need for a Near-Wall Treatment, contrary to the k-ϵ model. However, it has a weakness in that it is very sensitive to values for k and ω in the freestream, making free shear flows hard to predict. This would make it less suitable for solving the flow of jets. Variants on this model are the Baseline (BSL) and Shear-Stress Transport (SST) models, which both incorporate a gradual change from the Standard k-ω model in the low-Reynolds number regions to the k-ϵ model in the high-Reynolds number regions. The SST accounts for the transport effects of the principal turbulent shear stress on top of this and is regarded as the best k-ω model for flows with adverse pressure gradients or separation.

5.2.3. RSM

RSM is a class of models that elaborates on the already presented k-ϵ and k-ω models. It is the most elaborate approach, because it does not incorporate the assumption used by Boussinesq of isotropic eddy viscosity. Instead it solves transport equations for the Reynolds stresses. As such the number of additional equations to be solved for 3D flows is seven (for 2D this is five). This way the model accounts for the effects of streamline curvature, swirl, rotation and rapid changes in strain rate better than the two equation models and is more accurate. The model is harder to close and convergence and even the differences in the solution may not always be very clear compared to the two equation models. Still, it should be seriously considered for flow that have strong gradients in Reynolds stresses, such as highly swirling flows and rotating flow passages and could therefore prove interesting for this case.

5.2.4. CONCLUSION

From earlier research it has become clear that the k-ϵ model outperforms the k-ω model for this case and therefore this one is decided to use in this research[9]. Literature has shown that the Realizable model could be the better option, because it predicts the spreading rate of both planar and round jets more accurately[9]. Also, the Standard model with the $c1\epsilon$-parameter changed from the default 1.44 to 1.6 has shown to improve predictions turbulent round jets. Therefore, these are the ones that will be investigated to see the best option for this particular combustion chamber case. In the end, also the flow structure of the k-ϵ model with $c1\epsilon$=1.3, the k-ω SST model and the RSM k-ϵ model with $c1\epsilon$=1.44 shall be displayed to see if they could provide new insights for future work.

5.3. COMPUTATIONAL DOMAIN

The dimensions of the basic configuration have been used for the mesh of the combustion chamber. However, to decrease computation time, symmetry is assumed and only $\frac{1}{6}^{th}$ of the actual volume is computed. The split is made along the z-axis at 0^o and at 60^o and can be seen in fig. 5.1. An angle of 60^o w.r.t. 30^o has been chosen, because this would lead to less singularity issues at the z-axis of origin.

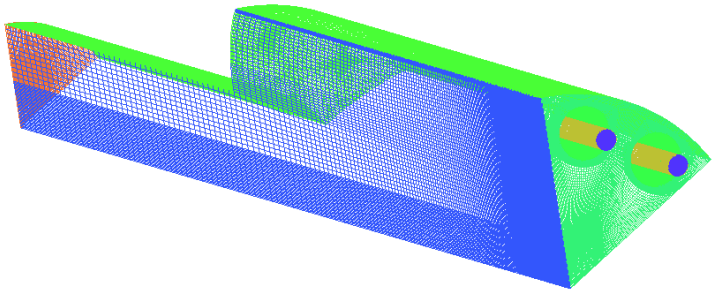

Figure 5.1: Geometry of the CFD domain

The structured mesh, shown in fig. 5.1, has been chosen instead of an unstructured mesh because it will have less cells for the same accuracy and is easier to control. However, making a correct structured mesh is harder, especially with complex shapes. This geometry is not that complex and was managed to construct using two O-grid blocks around the jets.

With the presence of all these different blocks in the geometry, the cell densities and their gradients can be controlled. Fine and high quality meshes are needed in places of interest. A low quality mesh will also hinder the convergence speed of solver, or could even refrain the solver from converging at all. To obtain a high quality mesh, attention has to be paid not to have steps in cell lengths larger than 1.2, aspect ratios (AR) of blocks should be around 1 and skewness of the cells should be low as well. The latter means that the cell corners should have right angles as much as possible.

A finer mesh leads to a more converged solution, but also leads to higher computational times. Therefore a mesh convergence study is needed to define when mesh refinement does not anymore lead to a more change in solution. This study has been based on a global and a local parameter. Namely, the absolute pressure difference between the inlet and the outlet, and a comparison of the velocity profiles in the nozzle and in the jet region. The characteristics of the different meshes are displayed in table 5.1, where the quality parameters are defined by ICEM and where '1' is best. The solver setting with which this study has been performed is explained in the next subsection, namely section 5.6.

The pressure difference in fig. 5.2 shows an asymptote at $\Delta P = 155Pa$. Meshes within 1% of this are said to be globally converged, as such mesh Finer 7 was taken and improved and producing the result of mesh Final, within the threshold. Figures 5.3 and 5.5 show the z-velocity profiles at x=50 and x=150 mm and figs. 5.4 and 5.6 show zoomed parts of these figures, respectively. From these figures it can be stated that convergence is reached after mesh Finer 2 and thus that the Final mesh provides a mesh independent solution.

Table 5.1: Mesh characteristics of convergence study

		Mesh quality parameters		
Mesh name	No. of nodes	Skewness	AR	Quality
Coarse 2	192483	0.947	0.281	0.877
Base 0	419421	0.948	0.272	0.948
Finer 2	713571	0.949	0.266	0.912
Finer 5	1454280	0.948	0.230	0.925
Finer 7	2237504	0.950	0.226	0.930
Finer 9	3329516	0.950	0.228	0.934
Final	1836728	0.948	0.230	0.925

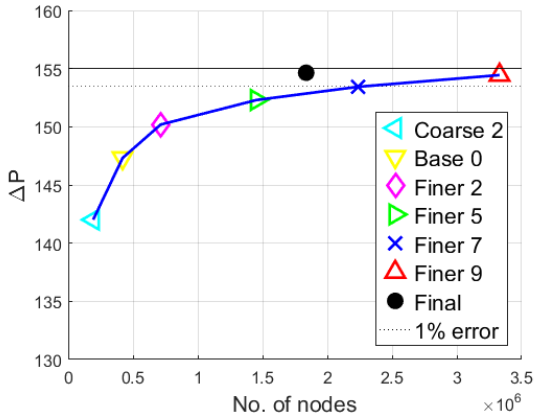

Figure 5.2: Global mesh convergence, based on pressure loss in the combustion chamber

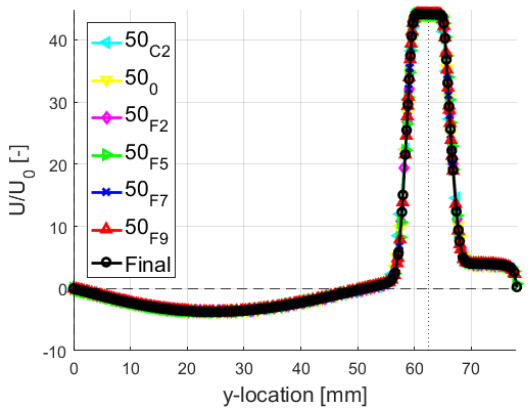

Figure 5.3: Z-velocity profile at z=50mm for mesh convergence study

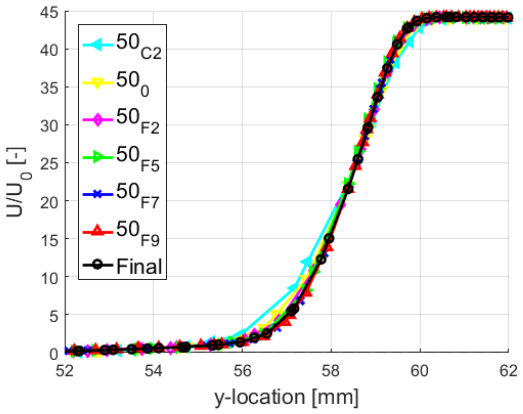

Figure 5.4: Zoomed z-velocity profile at z=50mm for mesh convergence study

5.4. BOUNDARY CONDITIONS

For this case, the following boundary conditions have been set for the domain. Firstly, the inlet is the start of the two nozzles and was set as a mass-flow inlet. Here a mass flow of 0.005305 kg/s, a turbulence intensity of 5% and a hydraulic diameter of 0.00845 m have been chosen as the default settings. The hydraulic diameter is equal to the nozzle diameter for the basic configuration. With this mass flow, a 45 m/s case for the experimental PIV setup is simulated. The outlet was set as outflow, since it the details of the flow at this location are not known prior to solving the case. The two sides of the geometry have been coupled using a periodic interface with a 60^o rotation.

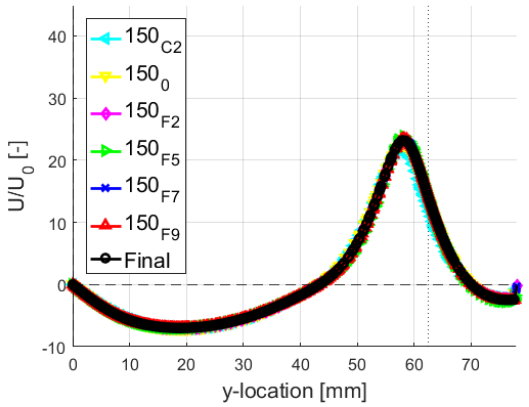

Figure 5.5: Z-velocity profile at z=150mm for mesh convergence study

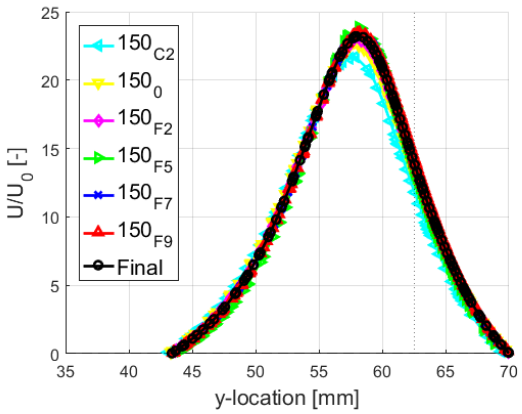

Figure 5.6: Zoomed z-velocity profile at z=150mm for mesh convergence study

5.5. NEAR-WALL TREATMENT

The near-wall region or boundary layer of a flow can be subdivided in mainly three regions. A viscous sublayer where the flow is laminar, a buffer layer providing a transition to finally the fully turbulent outer layer. These layers are displayed in fig. 5.7. On the x-axis, the y^+-parameter can be seen, which is the dimensionless wall coordinate defined by eq. (5.4). In eq. (5.4) Δy_p is half of the height of the first mesh cell, ρ is the air density, τ is the friction force and μ is the dynamic viscosity. In this equation, only τ is a variable which is defined by eq. (5.5), where μ is now the friction coefficient and $\delta U/\delta y$ is the velocity gradient calculated by the model.

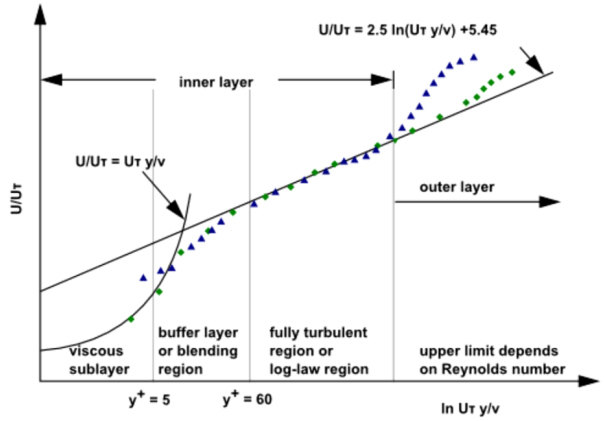

Figure 5.7: Subdivisions of the near-wall region, as taken from the ANSYS Fluent Manual

$$y^+ = \frac{\Delta y_p \sqrt{\rho \tau}}{\mu} \tag{5.4}$$

$$\tau = \mu \left(\frac{\delta U}{\delta y} \right) \tag{5.5}$$

The boundary layer is formed by to the no-slip condition at the wall, altering the mean velocities and giving a strong gradient to the velocity from the wall to the freestream. This gradient in the mean velocity causes high turbulent kinetic energy in this layer. Due to the large gradients and transport of momentum and other scalars, turbulence and vorticity are produced mostly in this layer. So an accurate respresentation is important to model a turbulent jet right. Which is again important for modelling the flow in the combustion chamber volume. The turbulence models are valid for the freestream turbulent flows, but different representations are needed to simulate the viscous boundary layer.

These representations can be split in two forms. Firstly, 'wall functions' solve the viscous sub-layer near the wall and the buffer layer based on semi-emperical relations and then link to the freestream. They completely replace the turbulence model in this layer and calculate the velocity gradient in eq. (5.5) from the semi-emperical relations. Therefore the y^+ value of the mesh that this function is used with should stretch into the buffer layer, so that the whole first cell can be replaced with a formula for the viscous sublayer. 'Near-wall models' on the other hand will actually modify the turbulence model and solve the boundary layer itself and are therefore only valid when the mesh near the wall is fine enough to give a good spatial resolution. The concept of this is shown in fig. 5.8.

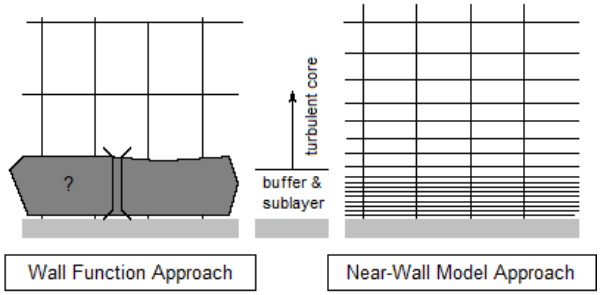

Figure 5.8: Near-wall treatment approaches: Wall fuction & Near-wall model, modified from the ANSYS Fluent Manual

To decide on the near-wall treatment that is used in this research, an investigation with two different meshes and the Standard Wall Function (SWF) and the Enhanced Wall Treatment (EWT) model have been performed. Two different meshes are needed, because for the EWT model a mesh with a $y^+ < 4$ at the wall is needed. An adapted version of the Final mesh was used for this.

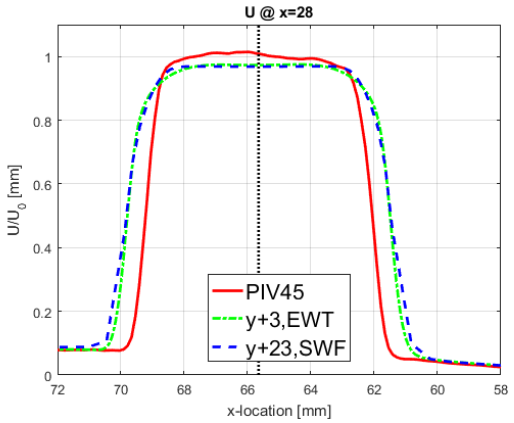

Figure 5.9: Velocity profile at z=28mm (1mm after the nozzle exit) from PIV and CFD, for wall treatment comparison

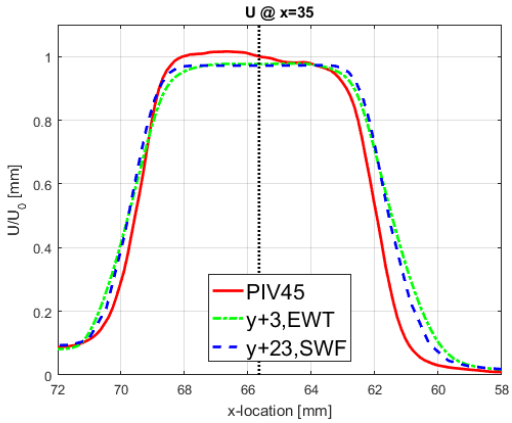

Figure 5.10: Velocity profile at z=35mm from PIV and CFD, for wall treatment comparison

The results of this analysis next to the PIV-results can be seen in figs. 5.9 and 5.10. Both approaches produce very similar results, but the SWF shows a slightly more similar profile at z=35mm than the EWT. Next to these results one should know that the EWT-cases were much harder to converge and took much longer as well. This is also a reason for choosing the Final mesh together with the SWF in this research.

To check whether the length-wise mesh refinement has converged in the nozzle, a convergence study has been performed as well. The used cases can be seen in table 5.2 and the result of it in fig. 5.11. As can clearly been seen from this, the mesh is already converged in the mesh called 'Final 0' and any refinement does not make any difference.

Table 5.2: Mesh characteristics of convergence study for the nozzle alone

Mesh name	Node distance $[mm]$
Final 0	1.0
Nozzle 1	0.5
Nozzle 2	0.25
Nozzle 3	0.1

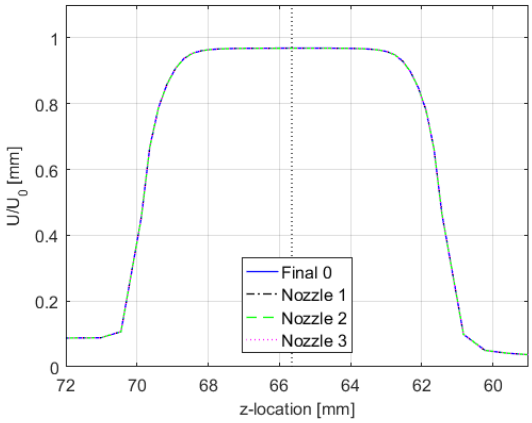

Figure 5.11: Result of nozzle convergence study, showing zoomed nozzle exit velocity profiles for different mesh refinements

5.6. SOLVER SETTINGS, SOLUTION METHOD & CONTROLS

When starting Fluent, a pressure based or density based solver should be chosen. In the pressure based solver the different equations are calculated seperately, whereas for the density based solver they are coupled and calculated simultaneously each iteration. The latter is needed for compressible flows, but each iteration takes longer. Since the flow of interest in this research can be regarded as incompressible, the pressure based solver is chosen.

Next to this solver setting, also a solution method needs to be specified to find the solutions of the transport equations for all the different cells in the mesh. Many different options are possible, some of which can cope with highly skewed cells or perform well with high-swirl or rotating flows, but often are then less robust. Table 5.3 shows the methods used for this research and a more elaborate motivation for this can be found in appendix B.

Table 5.3: Chosen solution methods

Solution Method	Type
P-V Scheme	SIMPLE
Gradient	Least Squares Cell Based
Pressure	Second Order Upwind
Momentum	Second Order Upwind
Turbulent Kinetic Energy	Second Order Upwind
Turbulent Dissipation Rate	Second Order Upwind

The solution controls are defined by the under-relaxation factors, these determine the ratio of the old value and the one determined by the new iteration. The default settings are recommended to used, because they are optimised for most of the common flow cases. When a solution does not seem to converge, the factors can be lowered, but this will increase computational times. If a solution is found with different under-relaxation factors, this will be mentioned with the results.

5.7. PARAMETER INVESTIGATIONS

After setting a base configuration for the way the different models and cases shall be approached, it is time to look at the models and cases themselves. The parameters that shall be investigated in this research are the following,

- Comparison of the k-ϵ Standard and Realizable model, including a c1ϵ change of 1.44 to 1.6 for the former model
- Boundary layer optimisation in the nozzle, by changing the length of this in the geometry of the mesh
- A turbulence intensity investigation as the boundary condition at the nozzle inlet.

For comparing results of different turbulence intensities with the PIV results, an extra formula is needed. Since u'$_{rms,z}$ and u'$_{rms,y}$ cannot be taken individually from the CFD results, the total u' is calculated using the turbulent kinetic energy using eq. (5.6). It can be read in the Fluent User Guide that Fluent uses this formula to calculate the RMS of the velocity fluctuations used for calculating the turbulence intensity.

$$u'_{rms} = \sqrt{\frac{2}{3}k} \tag{5.6}$$

5.8. CONCLUSION & LIMITATIONS

From this chapter and the analysis presented here, the solver settings can be summarised in table 5.4.

Table 5.4: Summary of the numerical experimental setup

	Chosen parameter
Solver	Pressure based
Turbulence model	Standard k-ϵ
Model constants	Cmu = 0.09, c1ϵ = 1.44, c2ϵ = 1.92, TKE Prandtl number = 1, TDR Prandtl number = 1.3
Near-wall treatment	Standard Wall Function

Limitiations that are clear from this CFD analysis are the following. Firstly, a structured mesh in combination with the geometry of the combustion chamber poses problems on the mesh quality. Due to the O-grid blocking, many of the refinement settings for the nozzles and the boundary layer have their effect throughout the whole domain. This can lead to large aspect ratios or meshes with high refinement in regions of low interest. The former leads to convergence problems, the latter to high computation times.

6

RESULTS

This chapter presents the relevant results from the experimental and numerical investigations of this research. The results from the preliminary runs, using the steel combustion chamber with the quartz glass windows, are shown in section 6.1. Afterwards, the results of the experiments using the transparent cylinder are presented. Starting with the flow structure in section 6.2, followed by the results on air recirculation and entrainment in section 6.3. Section 6.4 shows the intermediate and final numerical results. These results are then used together with Plane B results from PIV, to show the 3D flow structures in section 6.5. A thorough analysis and discussion of the results is performed in chapter 7.

A few notes are to be made for all results. The middle of the burnerface is set as x,y,z = 0,0,0 mm (see fig. 6.2), the z-location for the exit of the nozzle is 27 mm and the diameter of the combustion chamber D is 156 mm. Also, because of the spatial error originating from the PIV measurements, the turbulence intensities are only investigated for the ZOOM-case. The velocity profiles can still be used for the other runs since the structures here are large enough to stay within the 3.25 mm for a 1% error.

One of the geometrical variables of the setup is the combustion chamber length, L_{cc}, which can be shortened from 2.25D of the basic configuration to 1.5D. A depiction of this difference in relation to the recirculation zone for the basic configuration can be seen in fig. 6.1.

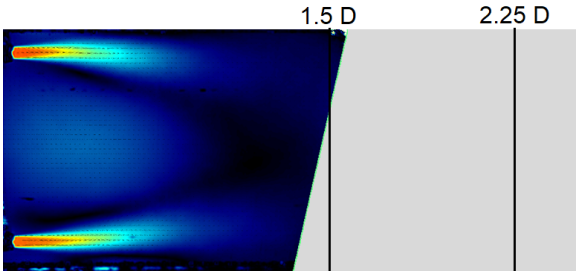

Figure 6.1: The variable combustion chamber length put into perspective of the RZ

6.1. PRELIMINARY RUNS

This section presents the results of the preliminary runs done on the combustion chamber, using the steel mid-section with quartz windows. Figure 6.2 puts the FOV of these results into perspective with the whole lay-out of the combustion chamber.

Figures 6.3 and 6.4 show two velocity fields for U_{jet}= 30 and 60 m/s, respectively. Both figures clearly show a black region, depicting zero velocity and marking the edge of the recirculation zone in the combustion chamber. Clearly, the FOV is too limited to say anything about the jet region. It was therefore decided to change the steel mid-section for a fully transparent acrylic cylinder with equal inner diameter.

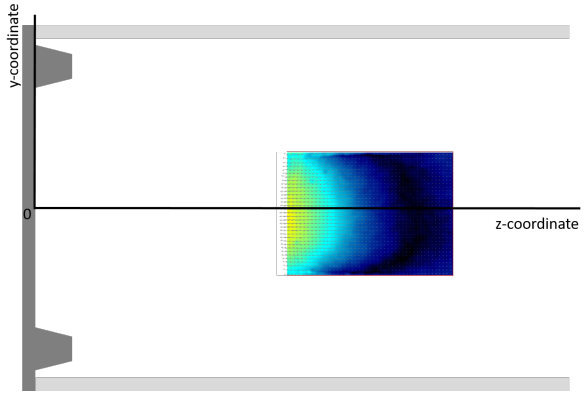

Figure 6.2: The FOV of the preliminary runs put into perspective with the whole combustion chamber lay-out

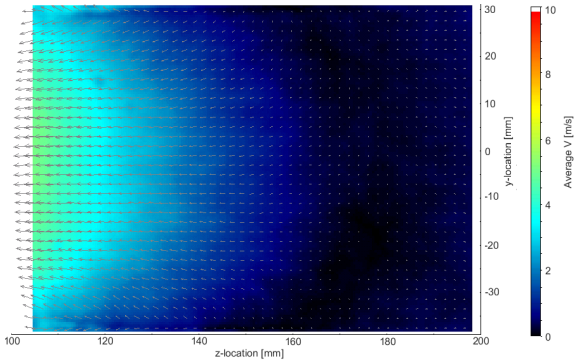

Figure 6.3: Velocity vector field of the FOV of the preliminary runs, U_{jet}=30 m/s

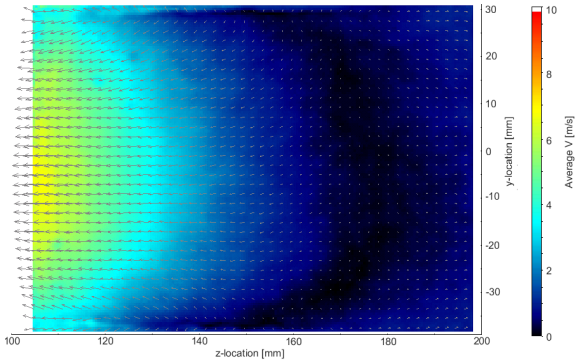

Figure 6.4: Velocity vector field of the FOV of the preliminary runs, U_{jet}=60 m/s

To strengthen the observation that the FOV shows the end of the recirculation zone, figs. 6.5 and 6.6 are shown. On these, the middle black line shows the division between air coming from the top and bottom into the RZ. Most clearly seen in fig. 6.5 can be seen that on the right it shows the end of the RZ, with a very low velocity region of almost 0 m/s.

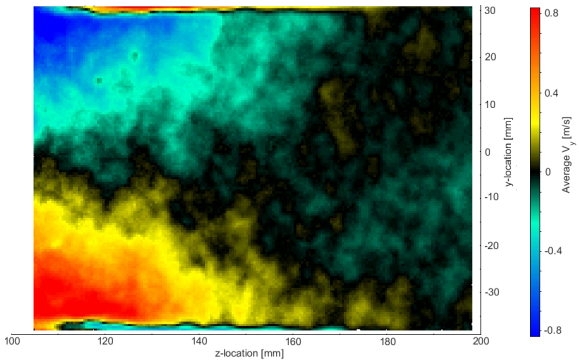

Figure 6.5: Vector field showing the y-component of velocity of the preliminary runs, U_{jet}=30 m/s

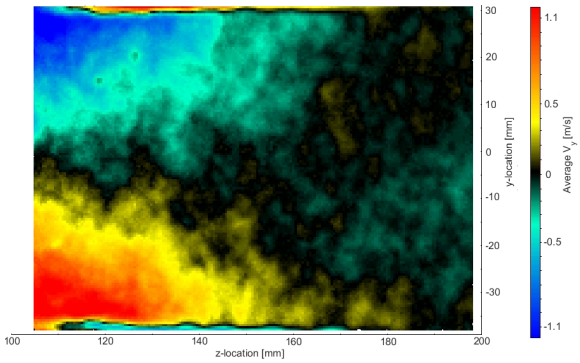

Figure 6.6: Vector field showing the y-component of velocity of the preliminary runs, U_{jet}=60 m/s

6.2. FLOW STRUCTURE

This section assesses the flow structure by looking into two parameters. The locations of the stagnation points (SP) are displayed to show the RZ shape and the velocity profiles are used to investigate the jet flow behaviour. For both parameters it is shown how they are affected by the combustion chamber length in section 6.2.1, by the nozzle diameter in section 6.2.2 and by the jet velocity in section 6.2.3.

6.2.1. INFLUENCE OF COMBUSTION CHAMBER LENGTH

RECIRCULATION ZONE SHAPE

The RZ shape of both combustion chamber lengths is summarised by plotting the stagnation points (SP) in fig. 6.7. Note with these plots that the SP's had to be identified visually, therefore an error of a few millimeters can be present. Movement of the stagnation points can be seen to be small and is not showing any correlation with the length of the combustion chamber. Especially not when taking into account the visual identification error. For both geometries, the length of the RZ is 1.18D and the width 0.62D. It does show that the lower SP is located more towards the burnerface than the upper SP in both cases. This is due to the asymmetry in the upper and lower jet strengths, where the upper jet is stronger than the bottom jet. This will be elaborated upon in chapter 7.

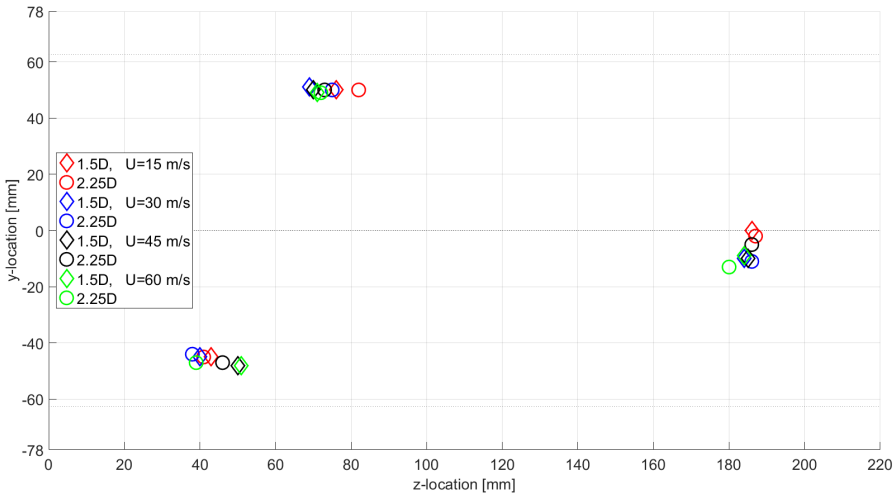

Figure 6.7: Distribution of the stagnation points for L_{cc}= 1.5D and 2.25D, for different jet velocities

VELOCITY PROFILES

Figures 6.8a, 6.8b, 6.9a and 6.9b show the normalised velocity profiles for both combustion chamber lengths, for U_{jet}=15 and 45 m/s and at z = 60 and 140 mm, respectively. For both velocities, it can be seen that no differences exist between the normalised profiles, not in the jet region, nor further downstream. Therefore there is no influence of the combustion chamber length on the velocity development of jet up to at least z = 140 mm. The small peak at y = 40 mm in fig. 6.8a is due to a reflection and should be ignored.

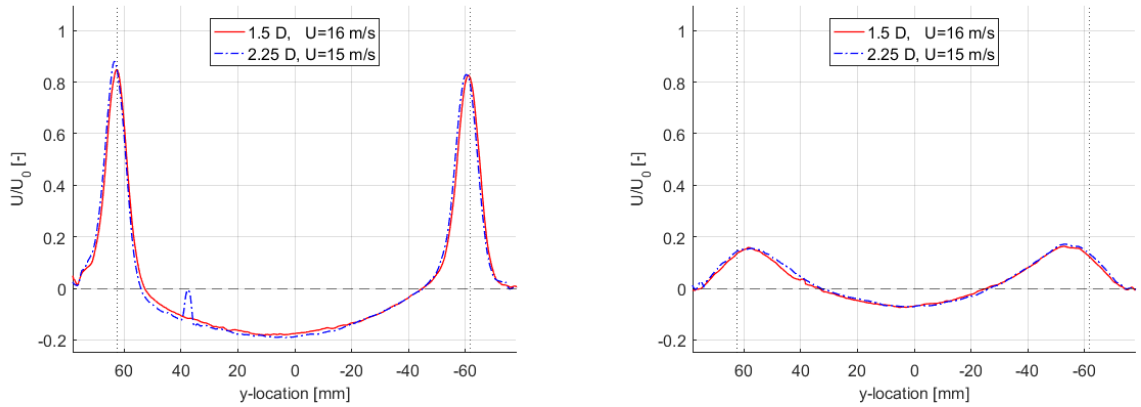

(a) taken at z = 60 mm

(b) taken at z = 140 mm

Figure 6.8: Velocity profiles for the three different nozzle diameters for U_{jet} = 15 at z = 60 and 140 mm

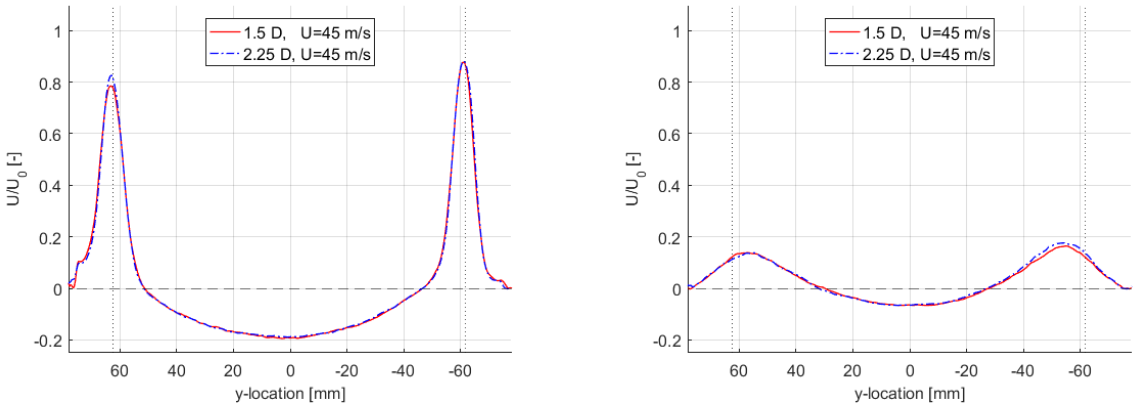

(a) taken at z = 60 mm (b) taken at z = 140 mm

Figure 6.9: Velocity profiles for the three different nozzle diameters for U_{jet} = 45 m/s at z = 60 and 140 mm

6.2.2. INFLUENCE OF THE NOZZLE DIAMETER

RECIRCULATION ZONE SHAPE

The SP locations for the three cases are plotted in fig. 6.10. The frontal and lower SP's show a correlation between the location and the nozzle diameter. With an increase in nozzle diameter, the RZ will become shorter and the lower SP moves towards the burnerhead and up. It can be seen that the asymmetry in the flow structure becomes larger for larger nozzle diameters. The sizes of the RZs are summarised in table 6.1. This shows that the length of the recirculation zone is always shorter than the combustion chamber length, but increases for decreasing nozzle diameter. The width of the RZ also increases for decreasing nozzle diameter.

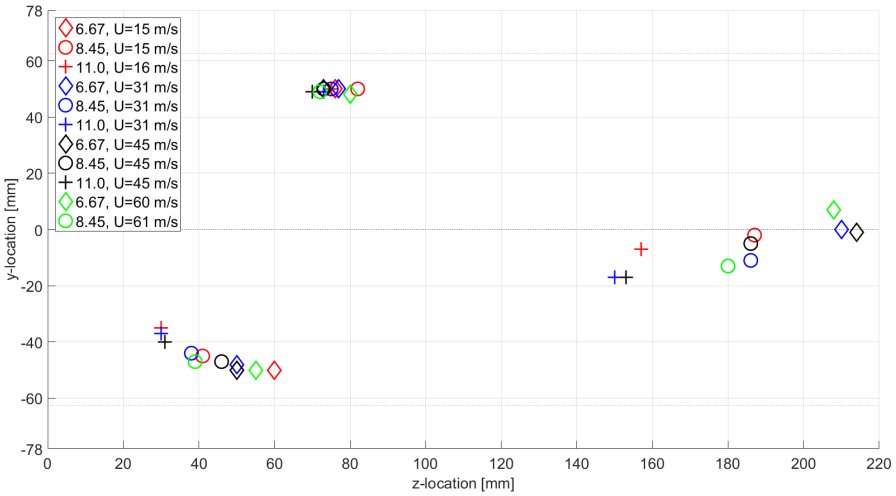

Figure 6.10: Distribution of the stagnation points for d_{nozzle} = 6.67, 8.45, 11.0 mm, for different jet velocities

Table 6.1: Overview of the average recirculation zone length L_{RZ} and width W_{RZ} for d_{nozzle} = 6.67, 8.45, 11.0 mm

Case	Length	mm	D	Width	mm	D
6.67 mm		211	1.35		99	0.63
8.45 mm		185	1.18		96	0.62
11.0 mm		160	1.03		89	0.57

VELOCITY PROFILES

Figures 6.11a, 6.11b, 6.12a and 6.12b display the normalised velocity profiles for all three d_{nozzle}, for U_{jet}=45 m/s at z-locations of 35, 60, 100 and 140 mm, respectively. They show that larger nozzle diameters yield wider jet flows. The difference in maximum jet velocity between the upper (left) jet and the lower (right) jet is larger for larger diameter nozzles, showing more asymmetry. It also shows an increased backflow velocity for larger nozzle diameters, which then reduces downstream and is weaker than the others at z = 140 mm.

The increased backflow is due to higher recirculated mass flows which need to be transported in a slightly smaller volume. The backflow velocity reduces quicker for larger nozzle diameters because turbulence is stronger in this zone for these cases, causing more dissipation. Equal behaviour is seen for the other velocities and these cases are therefore not shown.

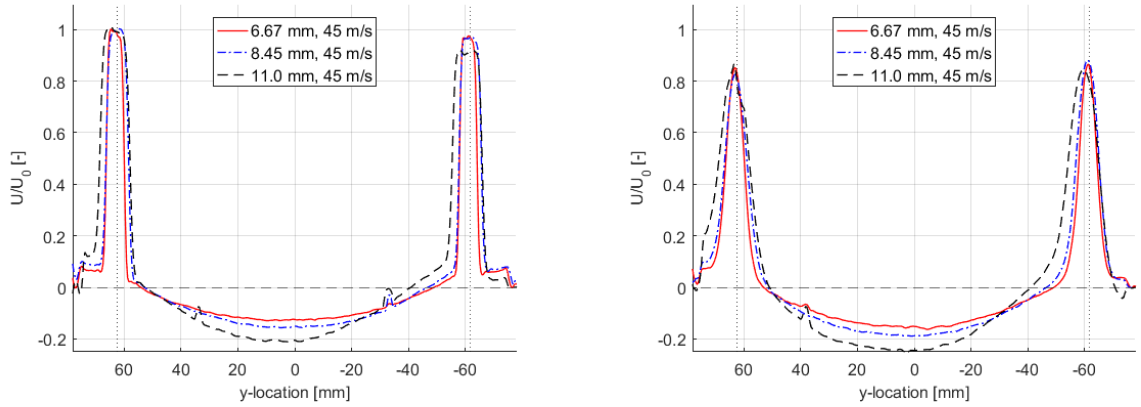

(a) taken at z = 35 mm (b) taken at z = 60 mm

Figure 6.11: Velocity profiles for d_{nozzle} = 6.67, 8.45, 11.0 mm, for U_{jet}= 45m/s at z = 35 and 60 mm

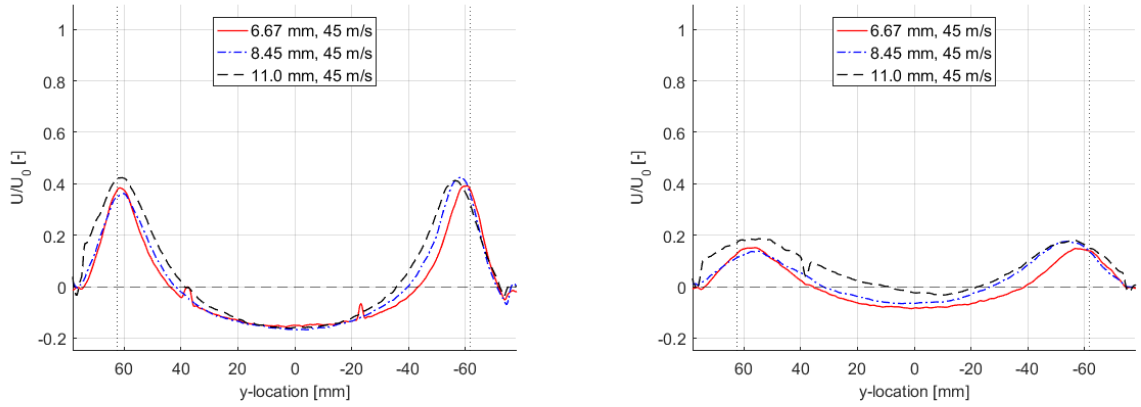

(a) taken at z = 100 mm (b) taken at z = 140 mm

Figure 6.12: Velocity profiles for d_{nozzle} = 6.67, 8.45, 11.0 mm, for U_{jet}= 45m/s at z = 100 and 140 mm

6.2.3. INFLUENCE OF DIFFERENT VELOCITIES

For the analysis of the recirculation zone shape, only the basic configuration is addressed. For the velocity profiles, the recirculation ratio and the turbulence characteristics all the three different nozzle diameter are addressed.

RECIRCULATION ZONE SHAPE

The RZ shape for the different cases is summarised by plotting the SP's in fig. 6.13. The small differences in SP locations do not show any consistency, the figure does not show a clear correlation between the shape and the velocities. What can be seen here again is the difference in z-location between the upper and the lower SP. For both geometries, the length of the RZ is 1.18D and the width 0.62D.

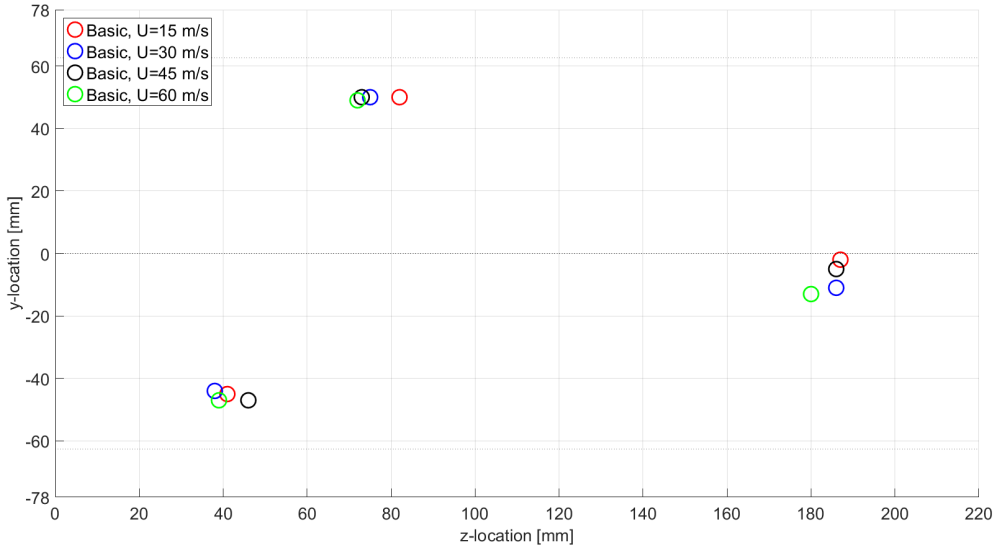

Figure 6.13: Distribution of the stagnation points for the basic configuration for U_{jet} = 15, 30, 45 and 60 m/s

VELOCITY PROFILES

Figures 6.14a, 6.14b, 6.15a, 6.15b, 6.16a and 6.16b show the velocity profiles for all three d_{nozzle} and possible jet speeds up to U_{jet}=75 m/s, at z-locations of 40 and 100 mm, respectively. They show that the profiles do not differ between different velocities for each of the diameters. For the profiles at z = 40 mm, the region between y = 0 and -50 mm, shows a stronger backflow velocity for higher velocities, with a maximum of a 5% difference, decreasing asymmetry for that configuration.

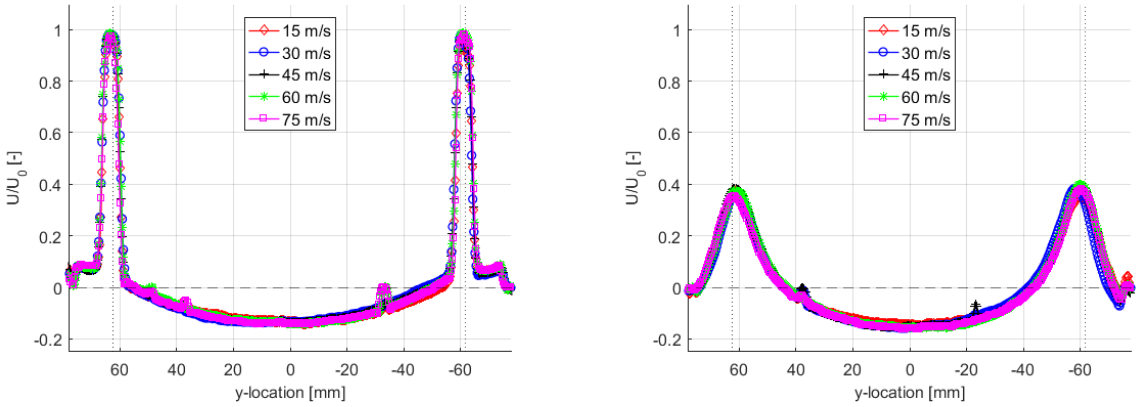

(a) taken at z = 40 mm (b) taken at z = 100 mm

Figure 6.14: Velocity profiles for d_{nozzle}=6.67 mm, for U_{jet} up to 75 m/s

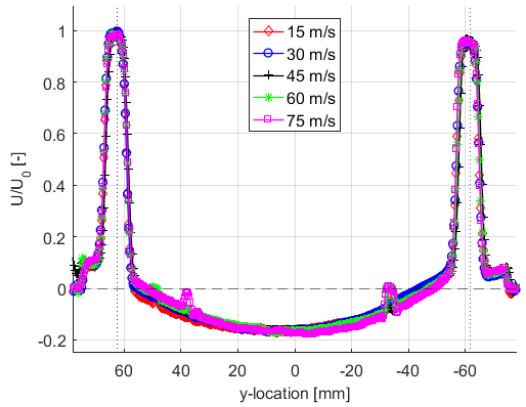

(a) taken at z = 40 mm

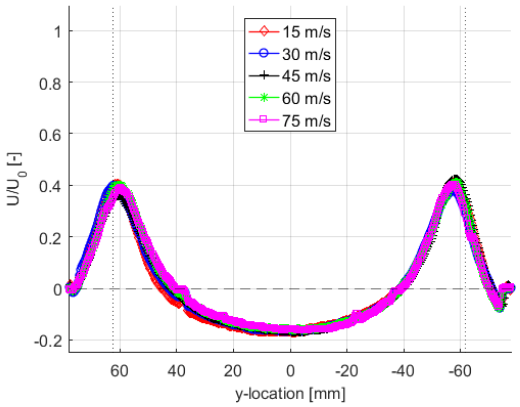

(b) taken at z = 100 mm

Figure 6.15: Velocity profiles for d_{nozzle}=8.45 mm, for U_{jet} up to 75 m/s

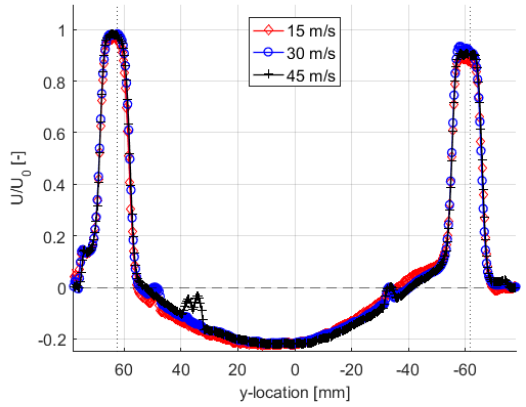

(a) taken at z = 40 mm

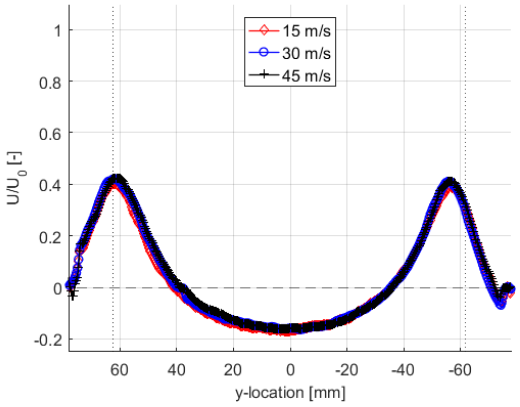

(b) taken at z = 100 mm

Figure 6.16: Velocity profiles for d_{nozzle}=11.0 mm, for U_{jet} up to 45 m/s

From these profiles it seems that the y- or radial location of the maximum velocity moves inward quicker for larger nozzle diameters. This is therefore portrayed in fig. 6.17, which shows that this is not the case, but that this parameter behaves similar for the different nozzles.

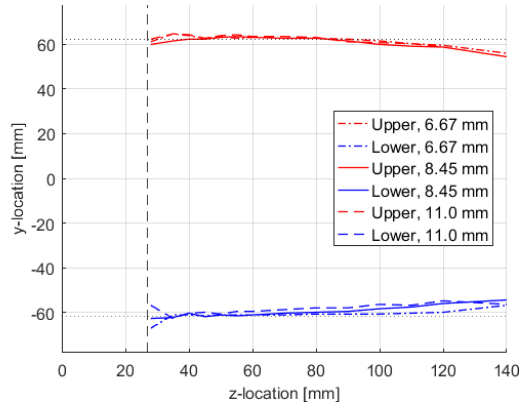

Figure 6.17: Y-location of maximum jet velocity locations for the three different nozzle diameters

6.3. RECIRCULATION & ENTRAINMENT

6.3.1. INFLUENCE OF COMBUSTION CHAMBER LENGTH

The Recirculation Ratios (RR) and Entrainment Rates (ER) for both combustion chamber lengths for U_{jet} = 15 and 45 m/s, are presented in figs. 6.18a and 6.18b, and figs. 6.19a and 6.19b, respectively. The RRs and ERs are calculated as has been explained in section 4.1. Note that these results are obtained with d_{nozzle} = 8.45 mm.

None of the results show significant differences between the two geometries. It does show that the maximum backflow of mass is achieved around z = 50 - 60 mm, approximately 5 mm aft of the point where maximum ER is achieved. From these results it can be concluded that no influence of the combustion chamber length can be seen on the RR and ER.

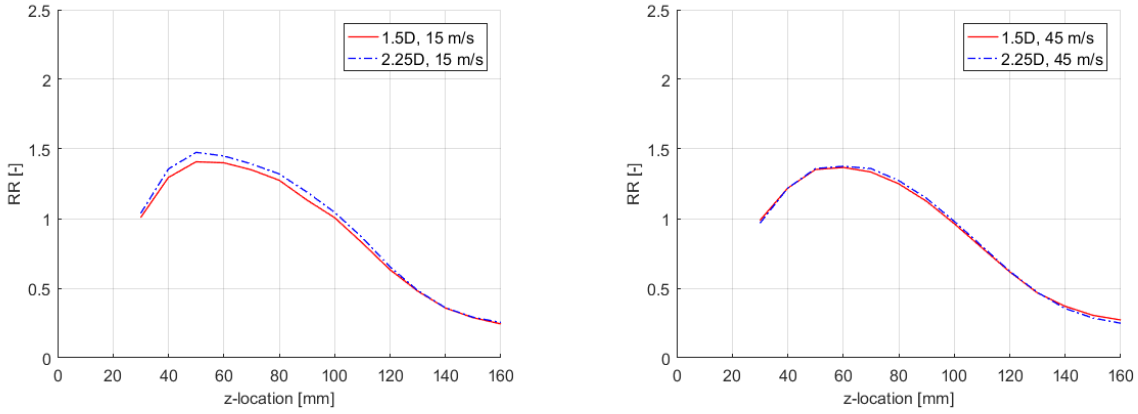

(a) U_{jet} = 15 m/s (b) U_{jet} = 45 m/s

Figure 6.18: Recirculation ratios over the z-axis for U_{jet} = 15 and 45 m/s in the combustion chamber for L_{cc} = 1.15 and 2.25 D

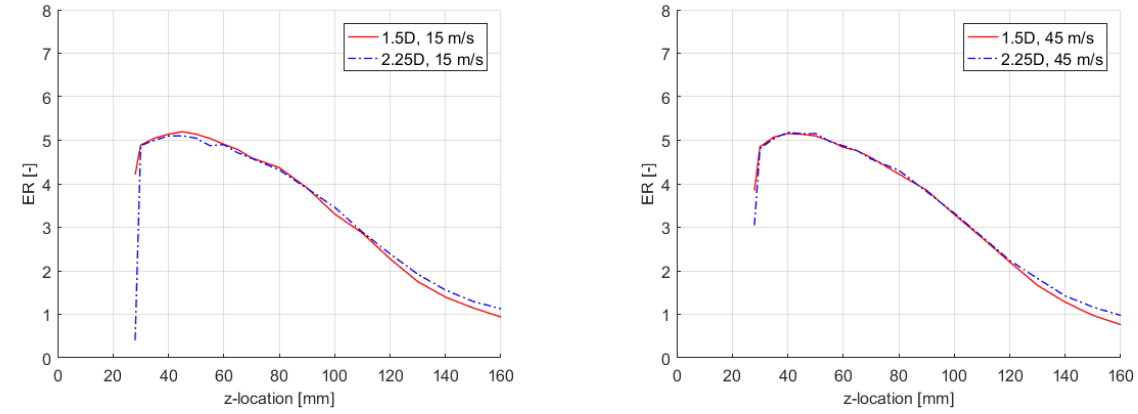

(a) U_{jet} = 15 m/s (b) U_{jet} = 45 m/s

Figure 6.19: Entrainment rates over the z-axis for U_{jet} = 15 and 45 m/s in the combustion chamber for L_{cc} = 1.15 and 2.25 D

6.3.2. INFLUENCE OF THE NOZZLE DIAMETER AND JET VELOCITY

This section assesses the results of recirculation, entrainment and the reynolds shear stress with respect to jet velocity, mass flow, and jet momentum for all three different nozzle diameters. To identify the recirculated and entrained mass flow, the maximum is taken from the centreline profile. This is always around z = 50 - 60 mm as can be seen in figs. 6.18a and 6.18b. Reynolds shear stress is calculated the way it has been explained in section 4.1.

Contrary to the results shown in figs. 6.18a and 6.18b, recirculation and entrainment will not be displayed using the RR and the ER, but directly using the recirculated mass flow and the entrained mass flow. Otherwise dividing it with respect to the inlet mass flow used in the calculation of RR and ER, will make a clear analysis harder.

COMPARISON ON JET VELOCITY

Figures 6.20a to 6.20c show the recirculated and entrained air mass flow and the Reynolds shear stress over the jet velocity for the three different nozzle diameters.

Firstly, it seem that they all show related behaviour. Higher reynolds shear stresses increase quadratically with velocity, which is expected when looking at the unit of the RSS and knowing its depiction is $\overline{v'w'}$. Higher RSS values indicate higher entrainment rates because of the increased momentum exchange between the y- and z-direction, meaning perpendicular to parallel to the jet flow. Higher entrainment rates lead to higher recirculated mass flows because more air needs to be fed back to the jets.

Secondly, a larger nozzle diameter shows increased RSS, entrained mass flow and recirculated mass flows for an equal jet velocity. This can be explained by the increased inlet mass flow that a larger nozzle diameter has with respect to a smaller one for equal jet velocity. An increased mass flow gives a higher jet momentum, that increases the RSS and as such in the end also the recirculated mass flows.

The increase in recirculated air flow and drop of entrained air flow shown for d_{nozzle} = 6.67 mm at U_{jet} = 75 m/s, cannot be explained. It has been investigated not to be due to a decrease or increase of reflections in the PIV results for these cases compared to the other cases.

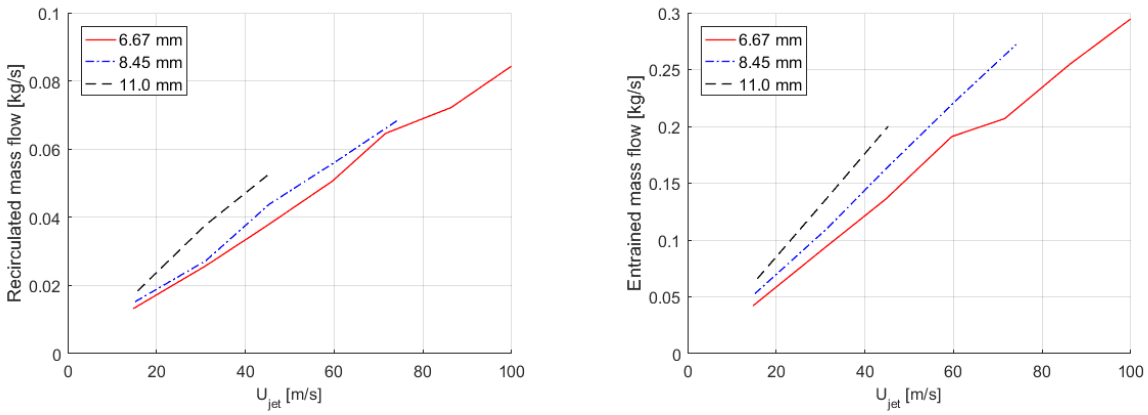

(a) Recirculation

(b) Entrainment

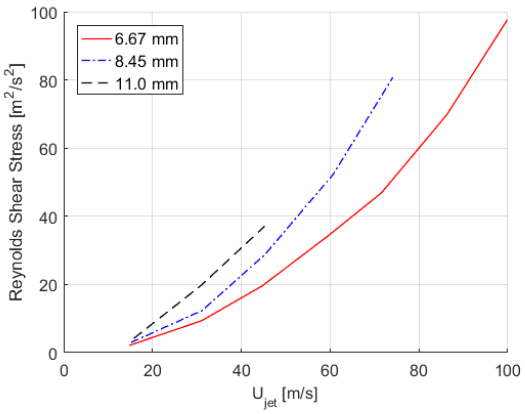

(c) Reynolds shear stress

Figure 6.20: Recirculated and entrained mass flows and Reynolds shear stresses over jet velocity, for d_{nozzle}=6.67, 8.45, 11.0 mm

COMPARISON ON INLET MASS FLOW

Figures 6.21a to 6.21c show the recirculated and entrained air mass flow and the Reynolds shear stress over the inlet mass flow for the three different nozzle diameters.

Firstly, they all show related behaviour again. This time however, the smaller nozzle diameter leads to an increased RSS, entrained mass flow and recirculated mass flows. This can be explained by the increased jet velocity that a smaller nozzle diameter has, with respect to a larger one for equal mass flows. This increased velocity leads to a jet with higher momentum, creating higher RSS values and as such more recirculation in the end.

Just as for figs. 6.20a to 6.20c, the plots for the different nozzles seem to express linear relations and are going through the origin, but only with different slopes. So for a certain mass flow or jet velocity, the ratios between the recirculated or entrained mass flows for the different nozzle diameters are approximately equal.

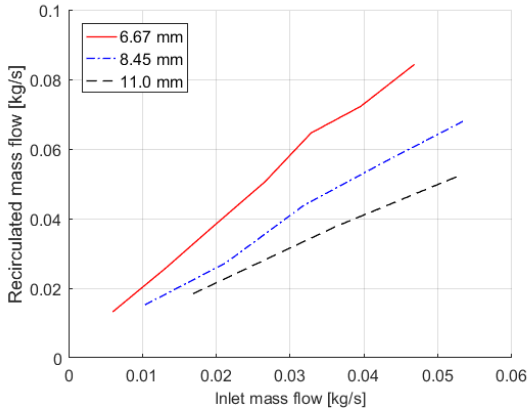

(a) Recirculation

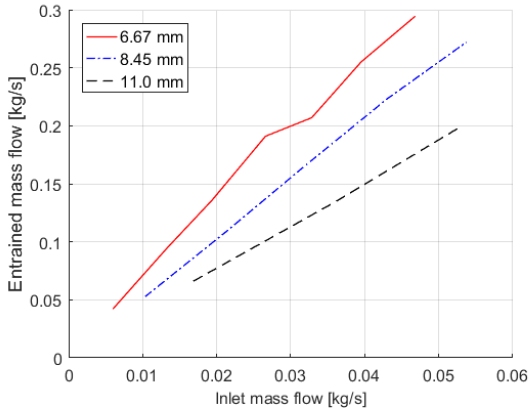

(b) Entrainment

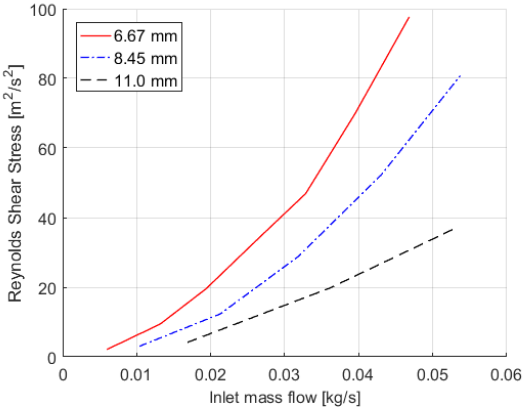

(c) Reynolds shear stress

Figure 6.21: Recirculated and entrained mass flows and Reynolds shear stresses over inlet mass flow, for d_{nozzle} = 6.67, 8.45, 11.0 mm

COMPARISON ON JET MOMENTUM

Jet momentum seems to be the driving force behind increasing or decreasing the RSS and this seems to be directly related to the entrained and recirculated mass flows. Note that although the defintion jet momentum is used, this is not completely right. Since mass is entering the combustion chamber per second, substituting m with $\dot{m}$ in the equation for momentum, this also leads to a momentum input per

second, as is shown by eqs. (6.1a) and (6.1b). Equation (6.1c) also shows why the unit of Newton is used in the graphs for momentum. However, for the remainder of the report, the defintion of jet momentum will be used to talk about $\dot{p}$, unless indicated differently.

$$p = m \cdot v \tag{6.1a}$$

$$\dot{p} = \dot{m} \cdot v \tag{6.1b}$$

$$\frac{kg}{s} \cdot \frac{m}{s} = kg \cdot \frac{m}{s^2} = N \tag{6.1c}$$

Figures 6.22a to 6.22c show the recirculated and entrained air mass flow and the Reynolds shear stress over the jet momentum for the three different nozzle diameters.

The differences between the different nozzle diameter seem to almost have gone away. The RSS values show a suprisingly good match for d_{nozzle} = 6.67 and 8.45 mm, as does the entrainment. For both of these d_{nozzle} = 11.0 mm shows slightly lower values. It is hard to say if this is indeed the case due to the limited number of data points for this nozzle diameter and the experimental errors. For the recirculated mass flows d_{nozzle} = 6.67 shows increased values for equal jet momentum. This difference is consistent and significant and is harder to attribute to errors. It could not be due to more entrainment in the plane of measurement, because this anomaly is not shown in fig. 6.22b. What could be the case is that there is an exchange of air between this primary flow plane and the secondary flow plane in between the jets. However this is hard say with the current measurements and would require a further investigation.

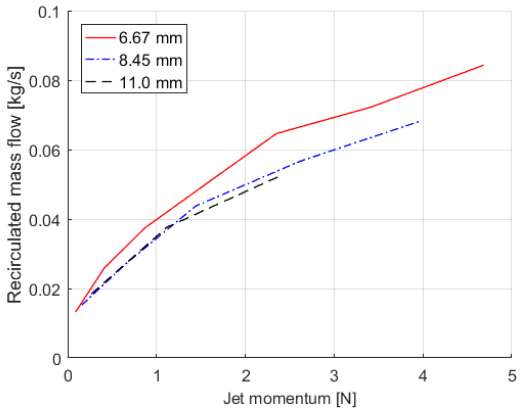

(a) Recirculation

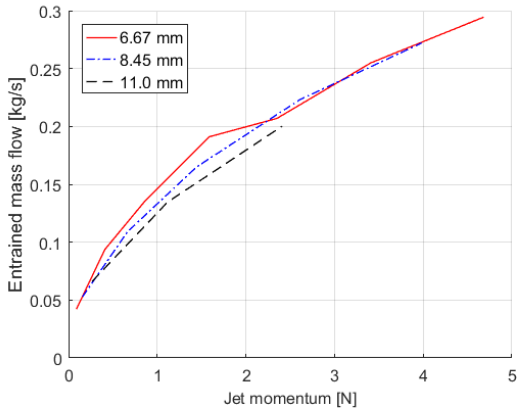

(b) Entrainment

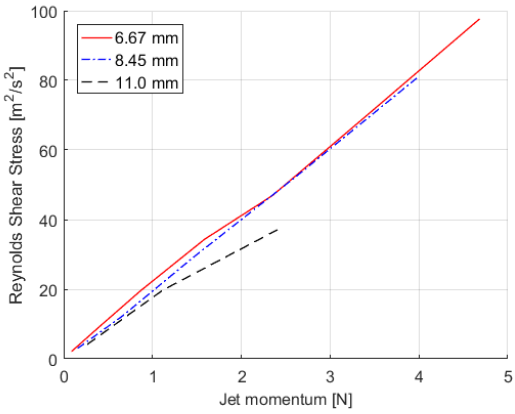

(c) Reynolds shear stress

Figure 6.22: Recirculated and entrained mass flows and Reynolds shear stresses over jet momentum, for d_{nozzle} = 6.67, 8.45, 11.0 mm

6.3.3. INFLUENCE OF THE JET VELOCITY ON RECIRCULATION RATIO

Figures 6.23a to 6.23c show the RR for all three nozzle diameters for different velocities. It seems that for all different diameters, the 15 m/s case shows the highest RR. The differences between the other velocities increments are in the order of a few percentages and no change is to be seen between the RR and the jet velocity for a constant nozzle diameter.

The behaviour of the 15 m/s case could be due to the low Reynolds number for this jet been investigated by Ricou and Spalding. It was found that the entrainment rate decreases for higher Reynolds numbers up to approximately $2.5x10^4$, after which it stays constant[65]. This could explain the differences seen, since for d_{nozzle} = 6.67 mm Re = 7000, for d_{nozzle} = 8.45 Re = 9000 and for d_{nozzle} = 11.0 mm Re = 12500 at U_{jet}=15 m/s. However, this behaviour should then also be seen in figs. 6.24a to 6.24c, which is not the case. It is therefore unknown what has caused this behaviour. Figures 6.24a to 6.24c, show the ER for all three nozzle diameters for different velocities. Again the differences between the velocities are negligible and no change is to be seen between the ER and the jet velocity for a constant nozzle diameter.

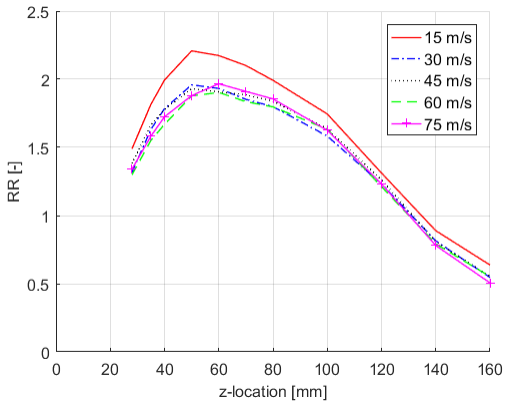

(a) d_{nozzle} = 6.67 mm

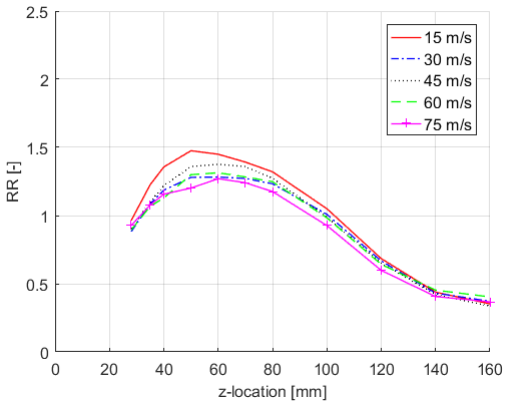

(b) d_{nozzle} = 8.45 mm

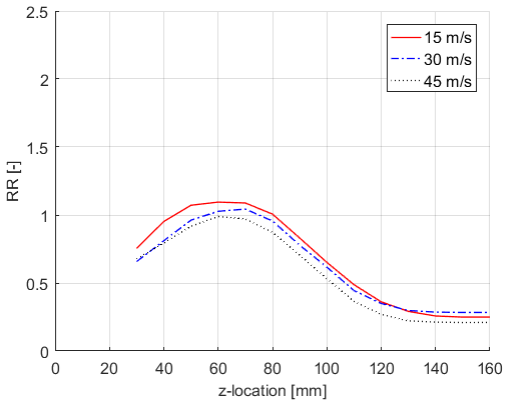

(c) d_{nozzle} = 11.0 mm

Figure 6.23: Recirculation ratios over the z-axis for U_{jet} = 15, 30, 45, 60 and 75 m/s in the combustion chamber for the different nozzle diameters d_n = 6.67, 8.45, 11.0 mm

Figures 6.23a to 6.23c also show that for any of the velocity cases, the RR is higher for a smaller nozzle diameter. This seems different from what was shown in the previous paragraphs of section 6.3.2, where higher recirculated airflows can also be obtained for larger nozzle diameters. However, for the calculation of RR, the recirculated airflow is divided by the inlet air flow. As such, what is actually depicted is how much airflow per second is recirculated for each kg/s that is put into the combustion chamber. The more narrow nozzle will input this kg at a higher speed, and therefore with a higher momentum and thus will recirculate more air with the same mass flow. So although the results may seem contradicting, they do line up with what was seen earlier.

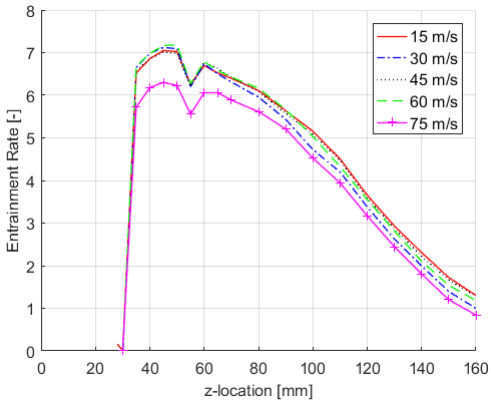

(a) d_{nozzle} = 6.67 mm

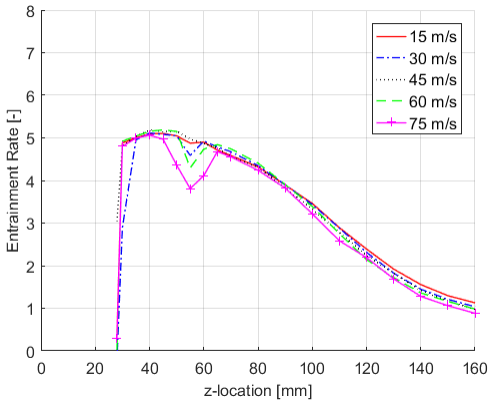

(b) d_{nozzle} = 8.45 mm

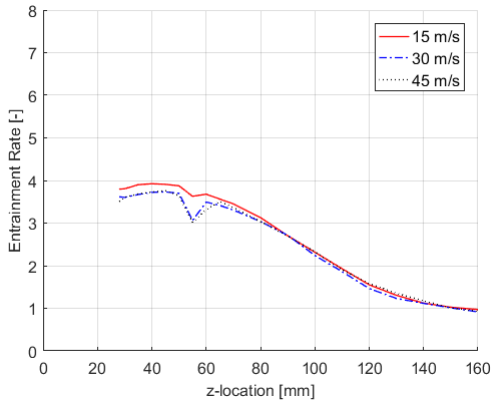

(c) d_{nozzle} = 11.0 mm

Figure 6.24: Entrainment rates over z-location, for different jet velocities for all three nozzle diameters

To strengthen the argument of the behaviour of RSS with respect to the cases of equal jet velocity, inlet mass flow and momentum, contourplots of the RSS in the combustion chamber volume are shown in figs. 6.25a to 6.25f. These runs have been chosen since they allow a comparison of RSS for cases for equal jet velocity, equal mass flows and jet momentum. Since the experimental runs were only performed for equal jet velocities, the equal mass flow and equal momentum flux cases are not exactly equal, but differ by a few percentages. This percentage is always less than 10% and also displayed in table 6.2, where the values for d_{nozzle} = 8.45 mm are used as the reference value. When comparing the right figures per case it can be seen that for equal jet velocities, higher RSS are obtained for smaller nozzle diameters. For equal mass flows, the behaviour is opposite. For equal jet momentum, the results are very similar and the difference shown can be attributed to the differences in momentum of the cases.

Table 6.2: Cases for d_{nozzle} = 6.67, 8.45, 11.0 mm used for comparison at equal mass flows and equal momentum

d_{nozzle}	Jet velocity m/s	Volume flow lpm	Mass flow kg/s	Jet momentum $kg \cdot m/s^2$	Difference -
6.67 mm	72	1578	0.0328	-	2.1%
8.45 mm	45	1545	0.0318	-	0%
11.0 mm	31	1692	0.0360	-	9.5%
6.67 mm	72	1480	0.0328	2.36	9.6%
8.45 mm	61	1972	0.0431	2.61	0%
11.0 mm	45	2399	0.0532	2.40	8.0%

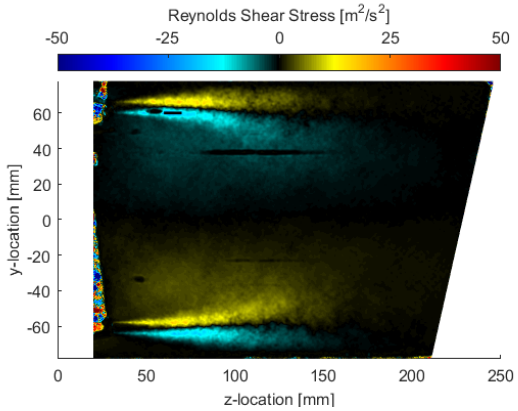

(a) RSS for d_{nozzle}=6.67 mm for U_{jet} = 45 m/s.
Case(s): **U_{jet}**

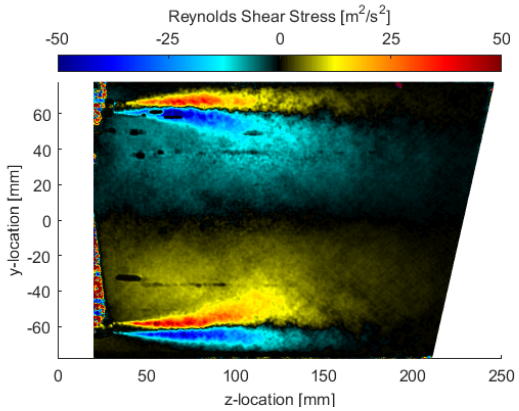

(b) RSS for d_{nozzle}=6.67 mm for U_{jet} = 75 m/s.
Case(s): **Mass flow**, **Momentum**

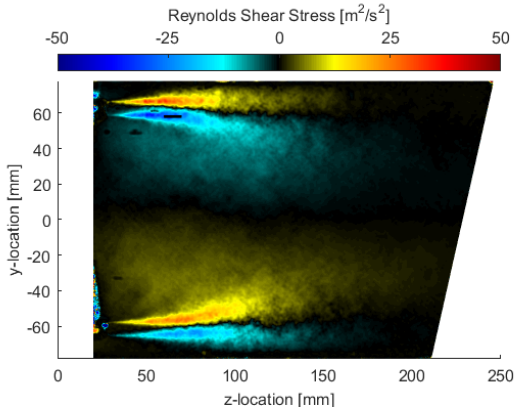

(c) RSS for d_{nozzle}=8.45 mm for U_{jet} = 45 m/s.
Case(s): **U_{jet}**, **Mass flow**

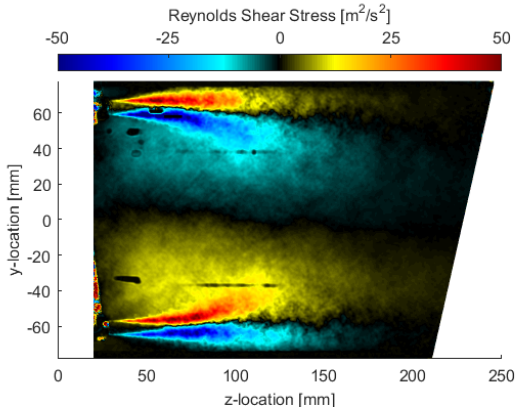

(d) RSS for d_{nozzle}=8.45 mm for U_{jet} = 60 m/s.
Case(s): **Momentum**

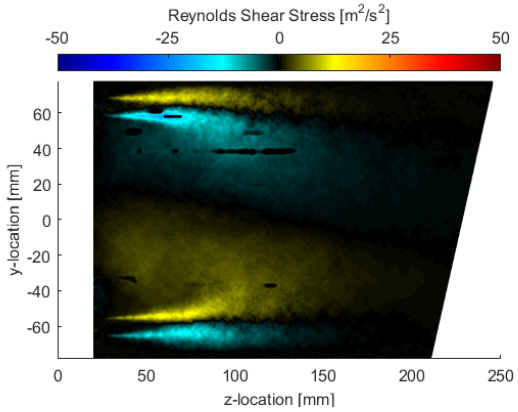

(e) RSS for d_{nozzle}=11.0 mm for U_{jet} = 30 m/s.
Case(s): **Mass flow**

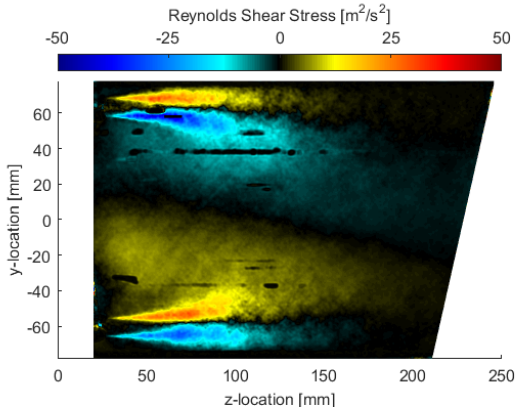

(f) RSS for d_{nozzle}=11.0 mm for U_{jet} = 45 m/s.
Case(s): **U_{jet}**, **Momentum**

Figure 6.25: Turbulence characteristics and entrainment rate for d_{nozzle}=6.67 mm, d_{nozzle}=8.45 mm, d_{nozzle}=11.0 mm for $\dot{m} \approx 0.0335\ kg/s$

6.4. CFD MODELLING

The CFD investigation is started using the settings discussed in chapter 5. For the turbulence model, this means the k-ϵ Standard model is used with c1-ϵ=1.44 and a standard wall function. From this baseline, the turbulence model is changed first to see how this impacts the results in section 6.4.1. Then the nozzle exit conditions are improved, by first investigating the boundary layer in section 6.4.2 and secondly the boundary condition of turbulence intensity is changed in section 6.4.3.

6.4.1. TURBULENCE MODEL INVESTIGATION

Next to the baseline model, c1-ϵ has been changed to 1.6 and the k-ϵ Realizable model has been chosen. These two turbulence model variations had been indicated by literature to give improvements over the standard settings.

RECIRCULATION ZONE SHAPE

Figure 6.26 shows the flow field from PIV and the three different turbulence models. Firstly, the difference in the length of the RZ between the models is clear. For the standard model with $c1\epsilon$=1.6 this is 227 mm or 1.46D, which is almost 24% longer than PIV. The other two are within 10% of the PIV result. Secondly, for the standard model with $c1\epsilon$=1.6 the jet penetration is much stronger than for the other two, where the standard model with $c1\epsilon$=1.44 gets closest to the PIV result. These results are unexpected, since the k-ϵ model is known to overestimate dissipation for turbulent round jets and would therefore underestimate jet penetration[66]. It is therefore thought that perhaps the jet outlet conditions are not equal to reality, as such affecting the dissipation rate.

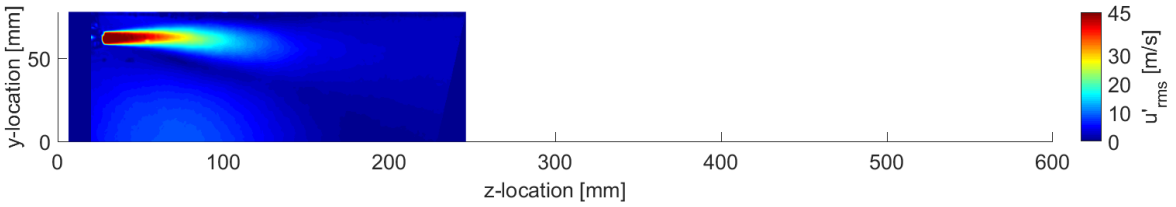

(a) PIV result for the basic configuration

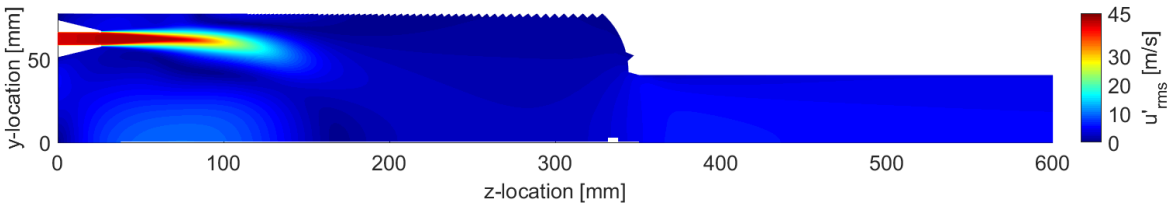

(b) k-ϵ Standard, c1ϵ = 1.44

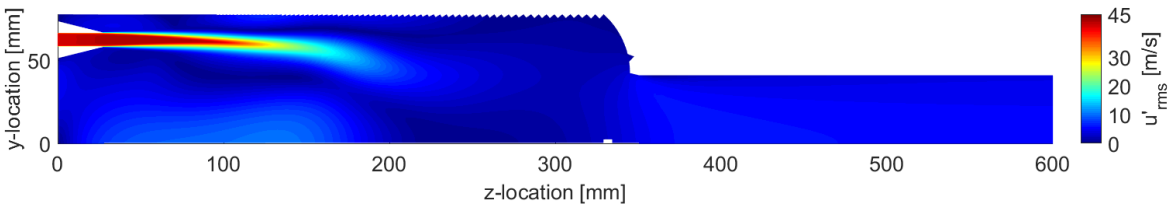

(c) k-ϵ Standard, c1ϵ = 1.6

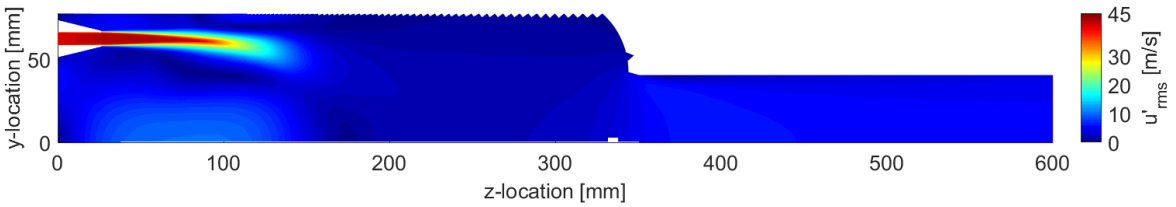

(d) k-ϵ Realizable

Figure 6.26: Contourplots of the PIV result and the three different turbulence models

VELOCITY PROFILES

Figures 6.27a to 6.27d show velocity profiles for the PIV result of the basic configuration and the CFD results for the three different turbulence models. The main observation from the contourplots can be seen here as well, which is that all CFD models overestimate the penetration of the jet into the volume at first and dissipate their energy much slower to their surroundings than the PIV results show. This also leads to a thinner velocity profile for the CFD-cases.

For z=35 mm, the results seem to correspond, however for an in-depth display of the nozzle exit profile, figs. 6.28a and 6.28b shall be used later on. At z=60 mm, there is still not much difference to be seen between the different turbulence models, although the PIV results already show a decrease in velocity. From z=100 mm it can be seen that the Realizable model penetrates less far than the Standard-1.6 model and Standard-1.44 penetrates even less far. Both these models also have a wider jet profile than the Standard-1.6 model. At z=140 mm the Realizable and Standard-1.44 model behave very similar and the Standard-1.6 model is still much behind on them. What is striking as well about this last location, is that the Realizable and Standard-1.44 model predict the U_{jet} = 0 m/s location well in both cases.

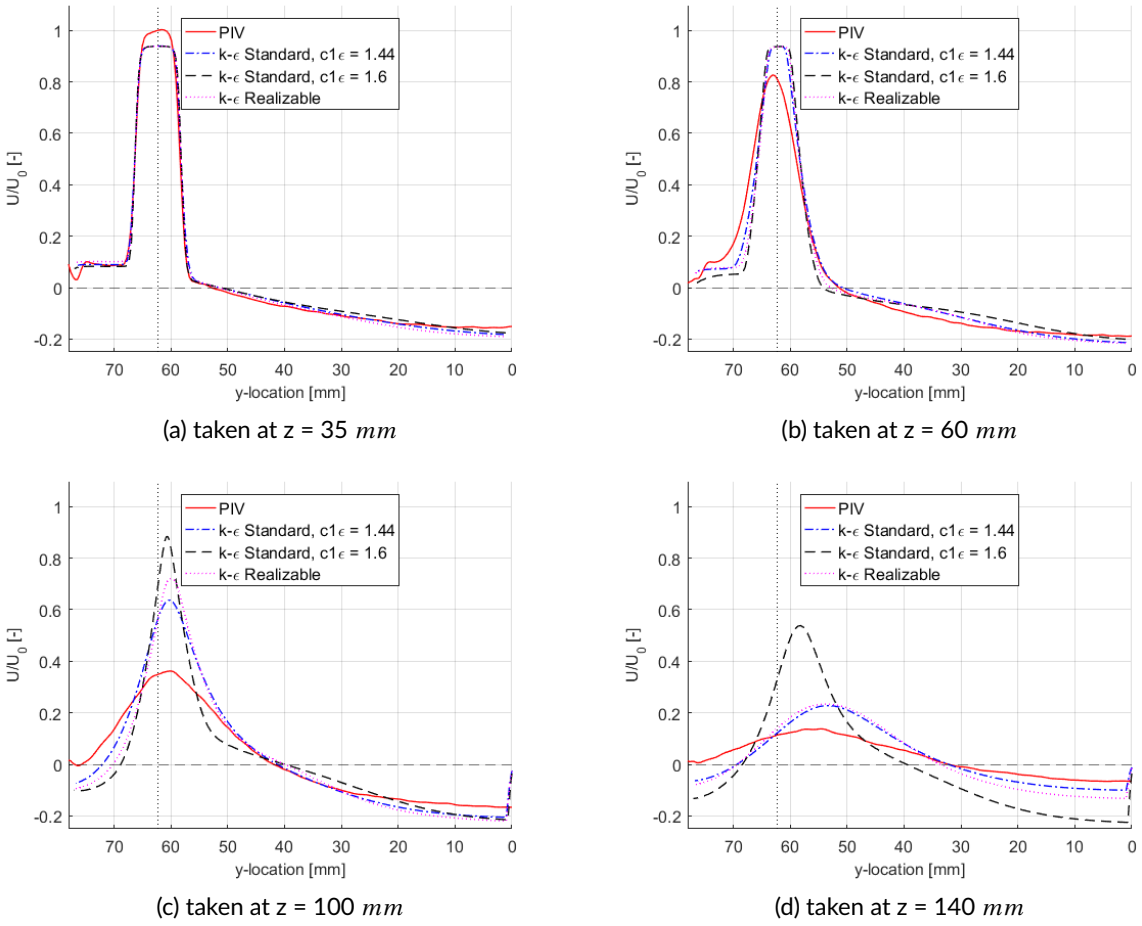

(a) taken at z = 35 mm

(b) taken at z = 60 mm

(c) taken at z = 100 mm

(d) taken at z = 140 mm

Figure 6.27: Velocity profiles for the PIV result and the CFD results of the three different turbulence models

To get a better grip on what the different turbulence models mean for the nozzle exit velocity, figs. 6.28a and 6.28b show a zoomed in view of this profile. Both figures show the PIV results at z = 28 mm, which is 1 mm behind the nozzle exit. Figure 6.28a also shows the CFD results 1 mm downstream, whereas fig. 6.28b shows the CFD profiles, right at the nozzle exit, to show that the diameter of the nozzle is correct in this simulation. Something one might doubt when looking at fig. 6.28a, since the downstream result shows a much wider velocity profile than the PIV results. Next to this it is clear to see that maximum velocity obtained by the models is also lower than for the PIV results. Apart from

these differences, the three turbulence models do not yet show any differences between themselves right here at the nozzle exit. This is expected, since the nozzle exit profile is mostly dictated by the wall treatment. Also, all turbulence models are based on the same equations and the nozzle length is too short to already develop differences.

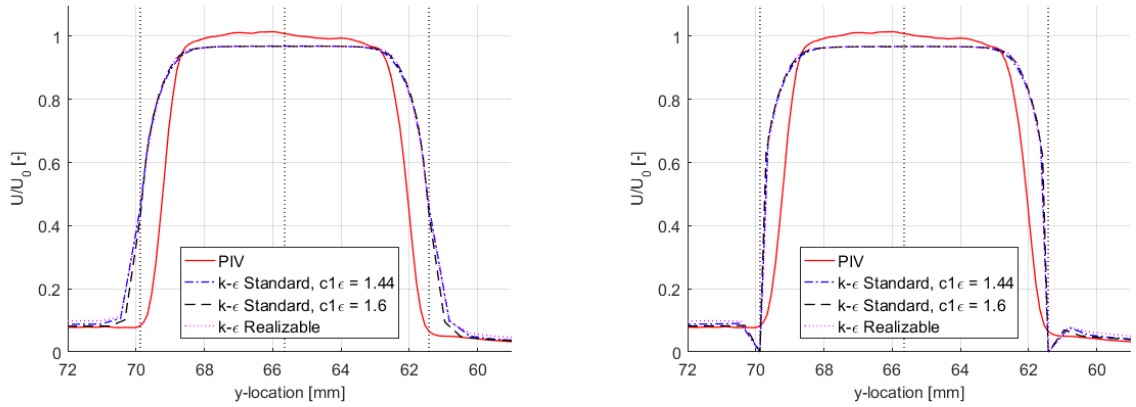

(a) taken at z = 28 mm, 1 mm behind the nozzle exit

(b) taken at z = 27 mm, right at the nozzle exit

Figure 6.28: Zoomed in velocity profiles for the PIV result and the CFD results of the three different turbulence models

From these first results two major anomalies are found. The jet penetration is much larger for the investigated turbulence models and the nozzle exit velocity profile shows a wider profile for the CFD analysis. Since the nozzle exit conditions will influence the jet penetration, this is first investigated.

6.4.2. BOUNDARY LAYER FIT

In an effort to improve the nozzle exit velocity profile, the boundary layer development is changed. The k-ϵ Standard model with c1ϵ=1.44 has been used as it gave the best results up to now. The nozzle length has then been changed to see if the Standard wall function would then give a better approximation of the jet exit velocity profile.

Figures 6.29a and 6.29b show the result of the impact this has on the velocity profile 1 and 8 mm after the nozzle exit. The actual nozzle length is 50 mm, but the best profile fit can be seen for L_{nozzle} = 85 mm. Since the PIV velocity profile diminishes quicker than the CFD models, mostly fig. 6.29a should be used as reference. The increase in nozzle length does not seem to influence the boundary layer thickness and deliver a sharper velocity profile. This is unexpected, since a longer nozzle would increase the boundary layer thickness and yield a more developed flow profile. Whereas now it seems from the velocity profiles that the cases with lenghtened nozzles, have a higher mass flow, due to the increased maximum velocity, while the rest of the profile remains almost unchanged. Because of this anomaly, the velocity profiles and TI profiles inside the nozzle are investigated.

Figure 6.30a shows the mean velocity profile imposed as a boundary condition at the inlet, which is equal for all cases, and how this has developed at the end of the nozzle for the different lengths. This shows a more developed flow for longer nozzle lengths, where the top-hat profile becomes a more parabolic profile and the core flow reduces in width and a higher maximum velocity if obtained. Figure 6.30b shows the TI profiles, starting with the intial condition of 5% and showing the final profiles for the three different lengths. From this it can be seen that the boundary layer is indeed thickening for a longer nozzle. It also shows a decreased TI in the core flow, because the flow can dissipate its turbulent energy for a longer time period.

Figure 6.29a actually already showed the more parabolic shape on the top for increased nozzle lengths, upon close inspection. Still, the behaviour seen on the sides of the velocity profile, creating an almost identical profile for all CFD cases and wider profile than the PIV results remains unclear. Figure 5.4 already showed that this could not be due to the mesh density.

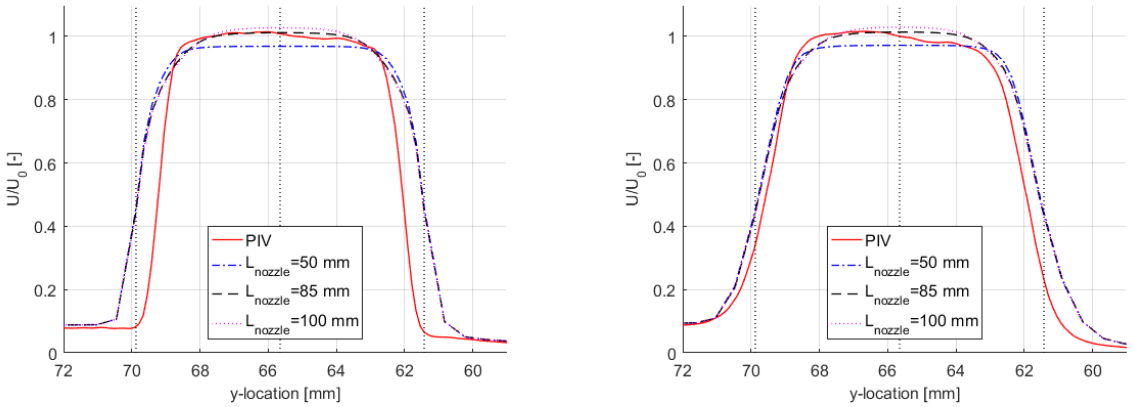

(a) taken at z = 28 mm (b) taken at z = 35 mm

Figure 6.29: Zoomed in velocity profiles for the PIV result and the CFD results of three different nozzle lengths

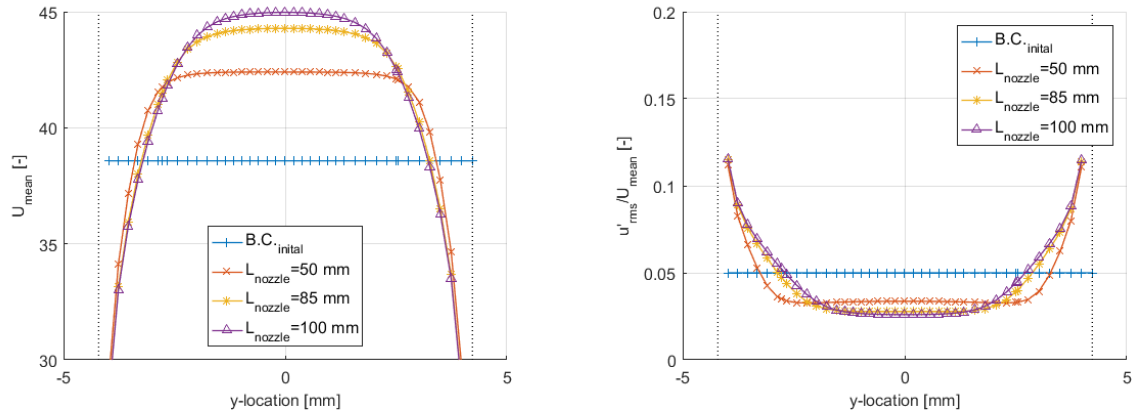

(a) mean velocity profile (the y-axis starts at 30 m/s) (b) TI profile

Figure 6.30: Profiles of the flow inside the nozzle taken at the outlet for the three different nozzle lengths, also showing the inlet boundary condition

Something that could be of an influence here is the swirl level inside the nozzle. Because of the shape of the burnerhead, swirl will be present in reality and therefore this is added as a boundary condition at the inlet. Adding swirl would change a portion of the axial kinetic energy to a tangential kinetic energy. This could decrease the width of the axial velocity profile at the nozzle exit and give a better prediction. A case with a tangential velocity component of 0.4 (w.r.t. 1.0 for the axial velocity component) imposed as a boundary condition has been run. This value was taken from literature to be a realistic value[67, 68].

Figure 6.31a shows the development of the tangential velocity component inside the nozzle. This shows that at first the maximum tangential velocity is 15.3 m/s with a steep profile in the middle, reducing to 13.5 m/s with a reduced slope at the nozzle exit due to dissipation. The case from the previous paragraph clearly shows no tangential velocity whatsoever. Figure 6.31b shows the nozzle exit velocity profile of the swirl case compared to the non-swirl and PIV results. The sides of the velocity profile have remained equal and only the top of the profile shows a difference. The maximum velocity obtained by the swirl-case is reduced, due to part of the axial kinetic energy being used tangentially and the extra amount of dissipated energy inside the nozzle. This was created by the steep velocity gradient imposed at the inlet. Clearly, the velocity profile has not come closer to match the PIV results. Perhaps, the solver itself smooths the steep velocity gradient at the sides of the profile with the flow that is present around the nozzle, but this remains uncertain.

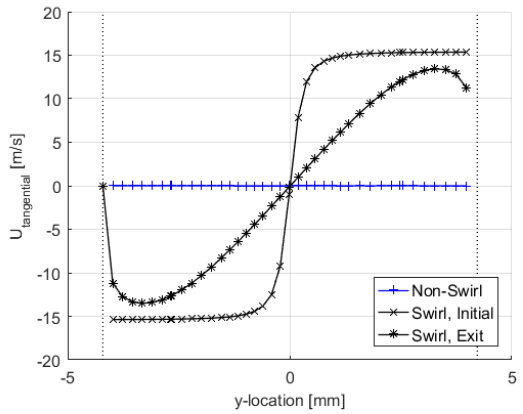

(a) tangential velocities inside the nozzle

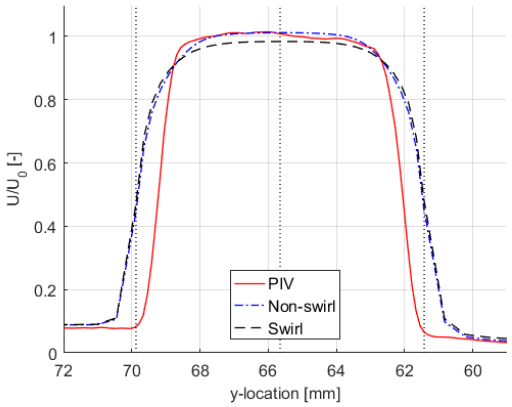

(b) velocity profiles 1 mm after of the nozzle exit

Figure 6.31: Velocity profiles for the non-swirl and swirl case, inside the nozzle and 1 mm downstream of the nozzle exit

6.4.3. TURBULENCE INTENSITY INVESTIGATION

In an effort to improve energy dissipation from the jet to the main volume of the combustion chamber, the turbulence intensity (TI) boundary condition at the jet inlet was changed. The k-ϵ Standard model with c1ϵ=1.44 is still used for this analysis, and TI has been changed from the default 5% to 13% and 20%. These cases do not incorporate swirl, but do incorporate L_{CC}=85 mm. Figures 6.32a and 6.32b show the normalised RMS profile of the velocity fluctuations and figs. 6.33a and 6.33b show the RMS profile divided by the local mean, thus the TI, both at 28 and 60 mm, respectively.

Both representations show a few things. Firstly, the TI does not change on the edges of the jet with a different boundary condition. Secondly, the centre of the jet shows small differences with strongly increased values of TI as boundary conditions. Thirdly, the TI is highly underestimated on the edges of the jet by almost a factor of 2. However, the trends that can be seen from the PIV measurements do correspond with CFD. To investigate the first two anomalies, the development of the TI profile inside the nozzle for the different boundary conditions is displayed in figs. 6.34a to 6.34c. What this shows is that even though the initial condition can be much higher, the TI values decrease quickly through dissipation and converge to similar solutions. TI values on the sides are equal for all and the initial condition of 5% ends up at 2.8% (1.8 times less), 13% ends up at 4.6% (2.8 times less) and 20% ends up at 5.4% (3.7 times less) at the core. These observations explain the equal TI profiles at the edge and the similar core values in TI profiles taken in the combustion chamber.

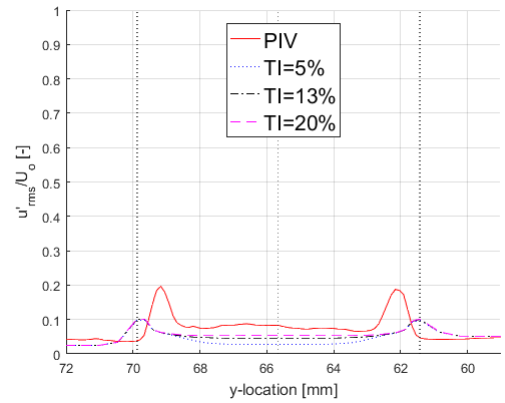

(a) taken at z = 28 mm

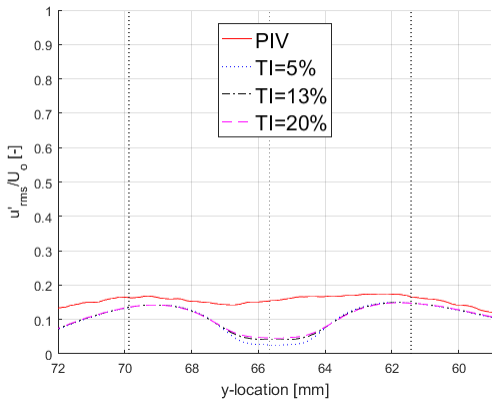

(b) taken at z = 60 mm

Figure 6.32: Zoomed in normalised RMS values of the velocity fluctuations of the PIV result and the CFD results for TI=5%, 13% and 20% as the boundary condition

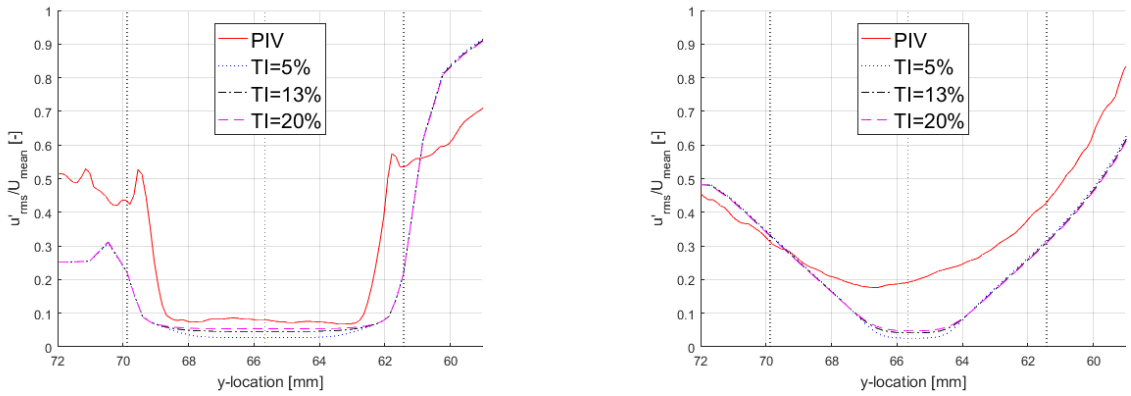

(a) taken at z = 28 mm (b) taken at z = 60 mm

Figure 6.33: Zoomed in TI profiles for the PIV result and the CFD results for TI=5%, 13% and 20% as the boundary condition

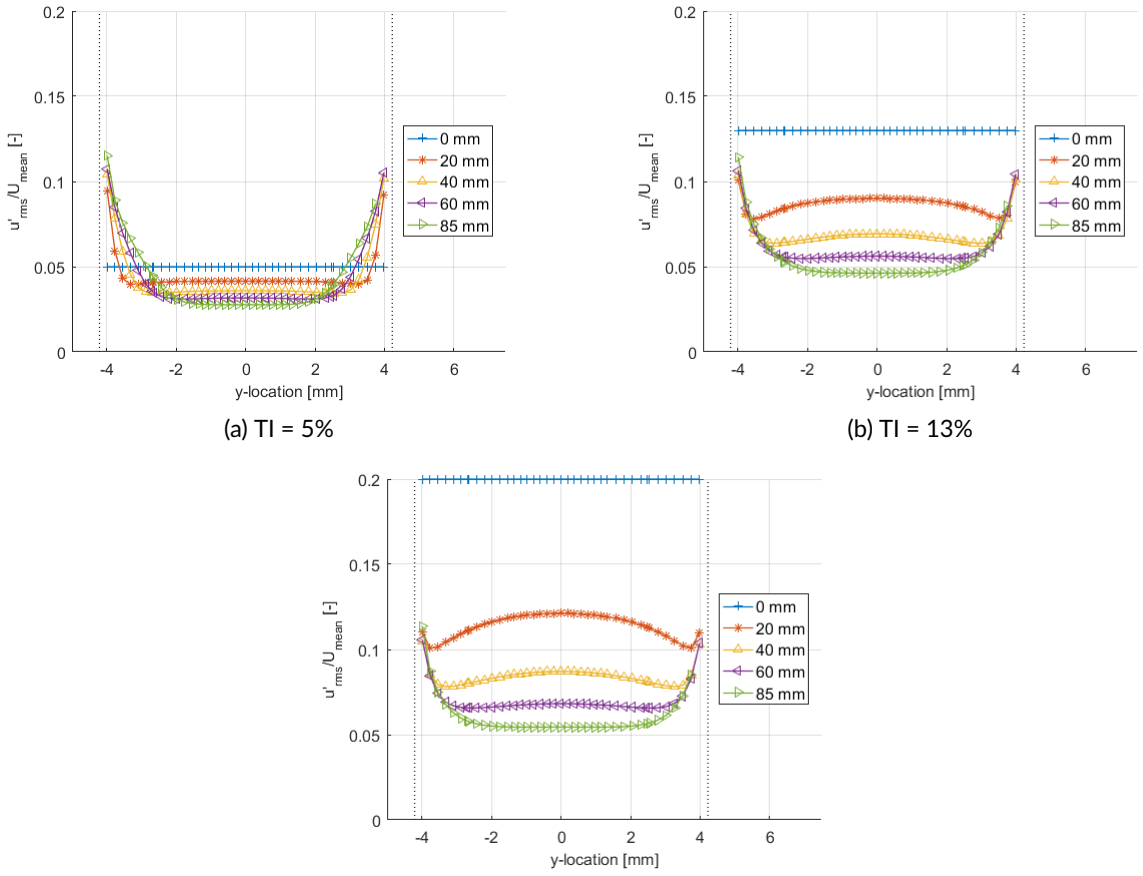

(a) TI = 5% (b) TI = 13%

(c) TI = 20%

Figure 6.34: TI development inside the nozzle for TI=5%, 13% and 20% as the boundary condition at z=0mm

To give a better idea of the overall difference in the RMS of the velocity fluctuations, contour plots of this are shown in figs. 6.35a to 6.35c for the PIV results and TI=5% and 20%. This agrees with the previous results, that the jet penetration is overestimated, and TI is underestimated. The PIV results show that the middle of the jet also has a higher TI than both CFD cases. This illustrates that the design of the burnerhead and the short nozzle length produce nozzle exit conditions that are far from a developed flow. This is important for improving this model. The lower TI values, may be the reason for the decreased dissipation and increased penetrations for the different turbulence models.

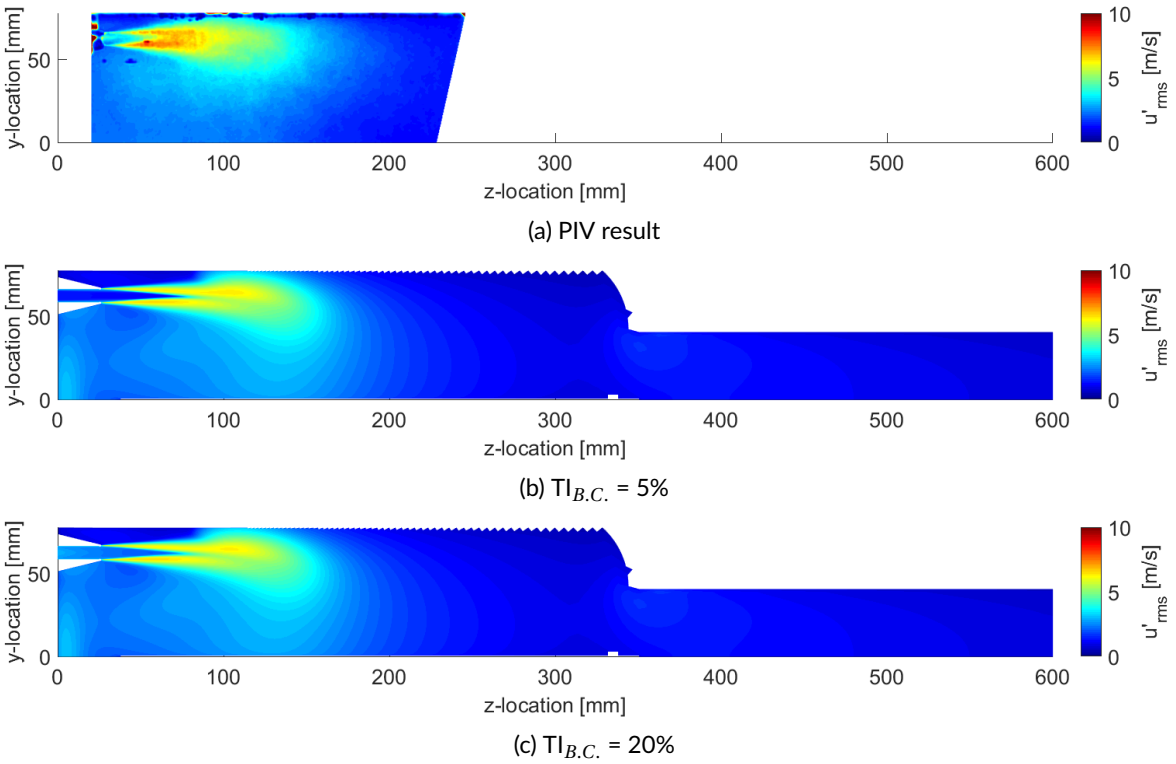

(a) PIV result

(b) $TI_{B.C.}$ = 5%

(c) $TI_{B.C.}$ = 20%

Figure 6.35: Contourplots of the RMS of the velocity fluctuations for PIV and CFD cases with TI=5% and 20%

6.4.4. OTHER TURBULENCE MODELS

Although literature indicated that the k-ϵ Standard or Realizable model would work best for this application and that c1ϵ values of 1.44 or 1.6 would be most beneficial, three other turbulence models are still investigated here. Firstly, the k-ϵ Standard model with c1ϵ=1.3 model is investigated, because this will have an increased dissipation rate, which could aid in matching the PIV results. Secondly, the k-ω SST is chosen because it incorporates the best of the k-ϵ and k-ω models. Thirdly, the k-ϵ Standard model with c1ϵ=1.44 is enhanced using the Reynolds Stress Model version of this model.

Figures 6.36a and 6.36b show velocity profiles of these models and the PIV result at z=60mm and 140 mm. All of the models still overestimate the jet penetration at z=60mm, although the k-ϵ model has a slightly widened profile. Behaviour of RSM and the k-ω model is similar, although the RSM predicts the y-location of maximum velocity better. Both still underestimate the dissipation of the jet. The k-ϵ model can be seen to be almost dissipated to zero at z=140mm.

Figures 6.37a to 6.37d show contourplots to assess the overall influence of the different models. The k-ϵ model seems to come closest to the PIV results, but shows a too short CRZ as well and weak jet penetration. The fact that its jet penetration is too strong at first, and still predicts a too short CRZ and then dissipates too much shows it is not an accurate model for this case. Although its behaviour close to the jet is better than for c1ϵ=1.44 or c1ϵ=1.6, downstream its dissipation is too strong.

The k-ω model is actually extremely similar to the k-ϵ Standard model with c1ϵ=1.44, when comparing these results with fig. 6.26b and show no improvements. Although the RSM result seems to deviate the most, it does depict a lengthened low-velocity zone at the end of the CRZ, similar to the PIV case. The length of the CRZ is stretched and lasts almost up to z=280mm compared to 200mm for the PIV results, but this is likely due to the strong overestimation of the jet penetration. As such, perhaps with an improved jet modelling, the RSM would get closer to the PIV result than the other models.

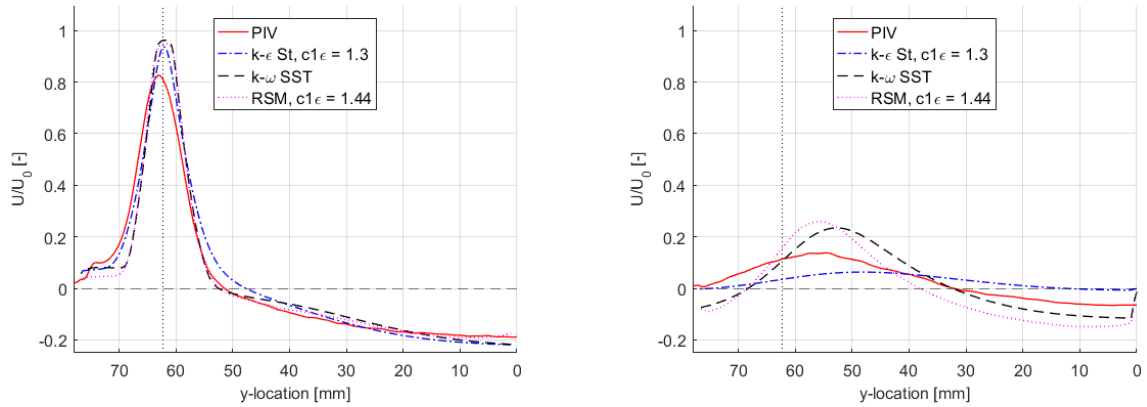

(a) taken at z = 60 mm

(b) taken at z = 140 mm

Figure 6.36: Velocity profiles for the PIV result and the CFD results of the k-ϵ St c1ϵ=1.3, k-ω SST and RSM k-ϵ turbulence models

(a) PIV result for the basic configuration

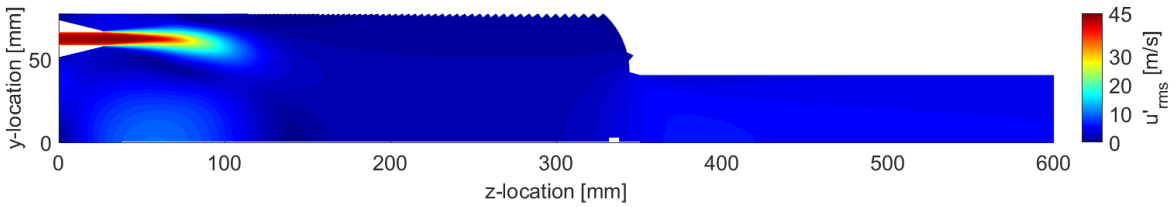

(b) k-ϵ Standard, c1ϵ = 1.3

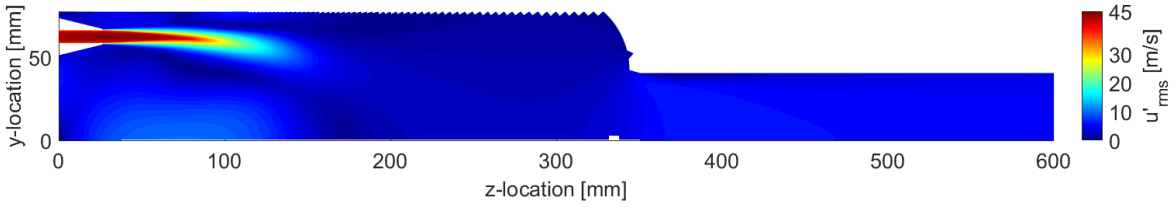

(c) k-ω SST

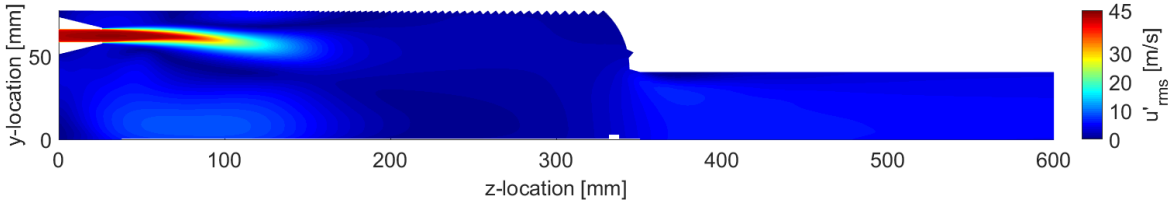

(d) RSM k-ϵ, c1ϵ = 1.44

Figure 6.37: Contourplots of the PIV result and the three other different turbulence models

6.5. 3D FLOW STRUCTURES

Using the PIV results from Plane B and the CFD results a better comprehension of the 3D flow structure can be obtained. Plane B corresponds in the PIV experiments to the laserplane being positioned in between the bottom two and top two jets, instead of cutting through the top and bottom jet (which was Plane A). The 3D investigation starts by looking into the jet interaction and the secondary flow structures, followed by an investigation in the change of the RR by including Plane B in de calculation and using the complete 3D structure of the CFD analysis.

6.5.1. JET INTERACTION & SECONDARY FLOW STRUCTURES

Figures 6.38a to 6.38c show that the y-position where the jets merge is around y = 60 mm for all cases, which is about 3 mm lower than the location of the jet itself. The z-locations for the upper/lower jets of d_{nozzle} = 6.67, 8.45 and 11.0 mm are z = 75/100 mm, 65/88 mm and 45/60 mm, respectively. This shows that a larger nozzle diameter producs a wider jet and will merge earlier. The differences in merging point per configuration, also shows that the lasersheet was not precisely located in between the jets. Otherwise the d_{nozzle} = 6.67 should not have different upper and lower locations. The centre of the image is the same as for Plane A, so this does not show anything new. The sides now show a more prominent PRZ between the jet flow and the wall. The PRZ can be seen to shift aft with decreasing nozzle diameter, following the earlier merging of the jets.

Plane A and B are depicted together in fig. 6.38d, showing the increase in PRZ size and the spreading of the jet well. The colorbar used here only goes up to 15 m/s, whereas the jet speed is 45 m/s, but this increases visibility of the weaker flow structures.

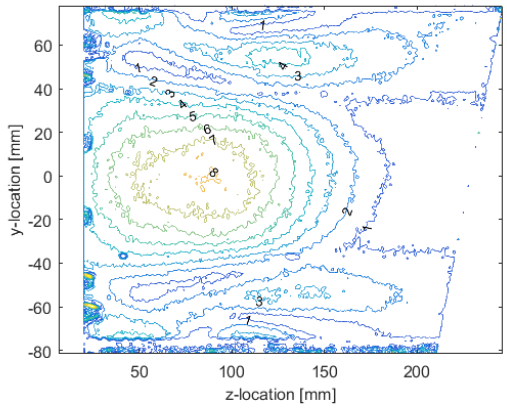

(a) Contourplot of Plane B for d_{nozzle} = 6.67 mm

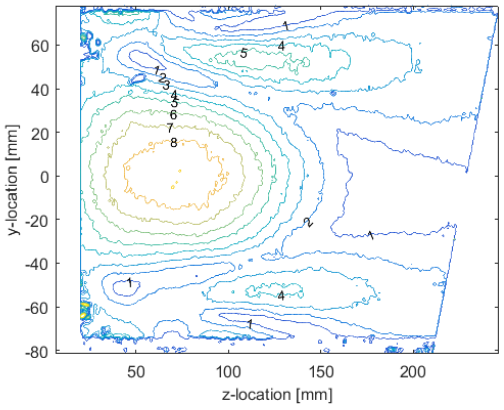

(b) Contourplot of Plane B for d_{nozzle} = 8.45 mm

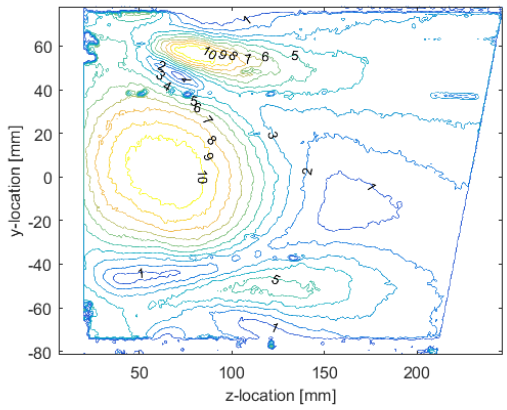

(c) Contourplot of Plane B for d_{nozzle} = 11.0 mm

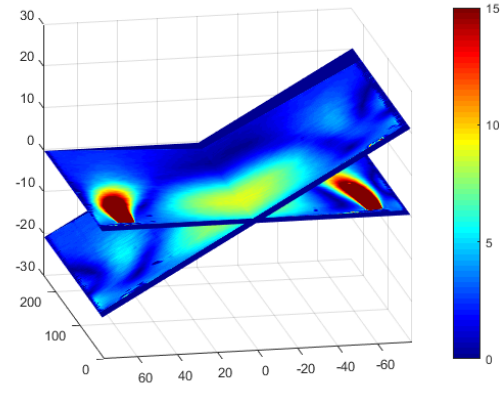

(d) Integration of Plane A + B for d_{nozzle} = 8.45 mm

Figure 6.38: Contourplots showing Plane B for all three different nozzles for U_{jet} = 45 m/s and putting it relative to Plane A. Numbers depict the local velocities in m/s

Figures 6.39a and 6.39b show velocity profiles for the PIV results and the three different CFD cases in plane B at z = 35 and 100 mm. From fig. 6.39a it can be seen that no jet interaction is yet to be seen. Instead, a large recirculation zone can be seen for values up to y = 50mm, after which the air again moves forward closer to the wall. Figure 6.39a shows that indeed the jet have merged at this z-location. The CFD results themselves seem to predict very much the same behaviour. Comparing the CFD results with the PIV results also shows a remarkable agreement in results, considering the differences seen in figs. 6.27a to 6.27d comparing the results in Plane A. Taking into account the spatial and ensemble size errors for the PIV measurement, the differences seen in fig. 6.39b become insignificant.

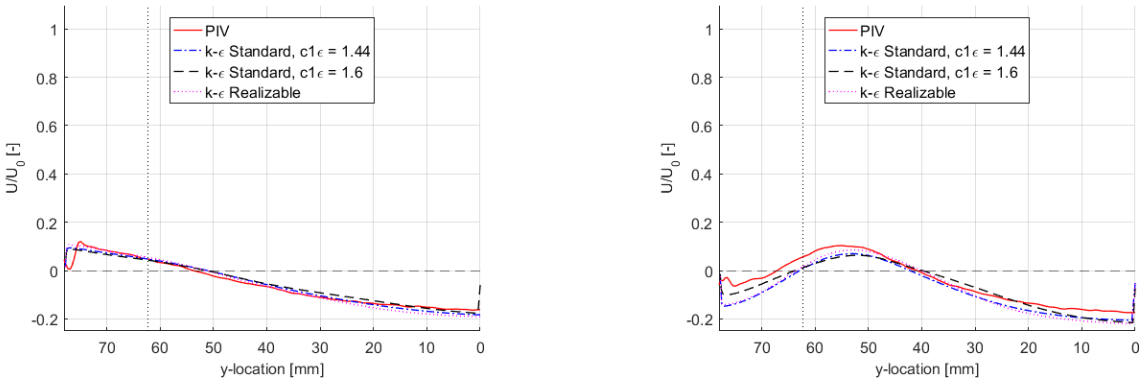

(a) taken at z = 35 mm

(b) taken at z = 100 mm

Figure 6.39: Velocity profiles for the PIV result and the CFD results of the three different turbulence models in Plane B

6.5.2. RECIRCULATION RATIO

Using an L_{cc} of 85 mm and a TI of 13%, the model has been run for multiple velocities. Firstly, fig. 6.40a shows the RR calculated in the same way as it has been done for PIV. This shows a relatively good approximation of the PIV results, although the CFD cases show a second bump at z = 100 mm. Figure 6.40b shows the RR calculated in a more accurate manner, namely by instead of computing the mass flow over only a line, it is calculated over the entire surface at the location of this line. For CFD this meant that a summation was made for all negative mass flows on that surface. For PIV, the results of the summation over a line for Plane A as well as B have been averaged to get an approximation. This shows an increase in RR of more than 20% at z = 100 mm, the location of the PRZ. PIV only shows a small increase at this location, because PIV cannot capture the PRZ well. Both figures show that the RR does not go to zero for PIV. This is due to the way it is calculated, not being able to capture the secondary flows well, which CFD does do in fig. 6.40b. Using the method of summation over one line overestimates the recirculation after z = 150 mm.

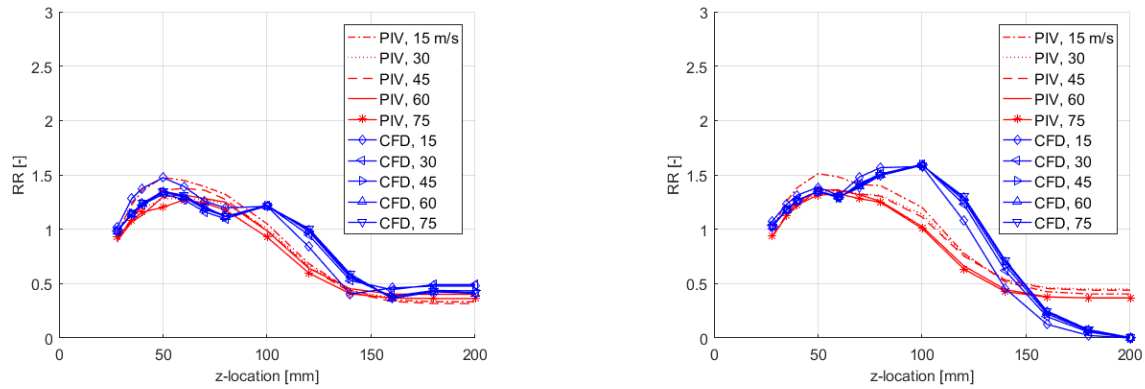

(a) RR calculated over a line running through the jet

(b) RR calculated over a surface

Figure 6.40: Recirculation ratios over z-location from CFD, calculated over a line and over a surface

7

Analysis & Discussion

This chapter analyses what has been seen in the results and discuss this. Firstly, the flow structures are treated in section 7.1. Secondly, recirculation, entrainment and the Reynolds Shear Stress are treated in section 7.2. This is succeeded by analysing the CFD results and discussing the validation with the PIV results in section 7.3. Lastly, the 3D flow structure shall be discussed in section 7.4.

7.1. The Flow Structure

The main point of discussion about the preliminary runs is that the FOV is limited to a spot of only 95 x 70 mm at the position of the end of the RZ. For research at elevated temperatures this means two things. Either a transparent quartz glass cylinder will have to be used in, to maintain the large FOV. Or it a limited FOV is to be accepted and the experimental campaign has to be adjusted to this. Apart from this clear result, the two most prominent results about the flow structure are the size of the recirculation zone and the asymmetry that can be seen for this setup. These are therefore seperately treated.

7.1.1. Size of the recirculation zone

The recirculation zone was shown to be shorter than 1.5D for all cases and to become shorter for larger nozzle diameters. Larger nozzle diameters also decrease the width of this zone increasing its strength. The zone shortens for larger nozzle diameters due to the increased width of the jet, merging earlier than for smaller nozzle diameters. No change in RZ shape or size was found when operating at different velocities for any of the nozzle diameters.

Flameless combustion is known for requiring a relatively large volume compared to conventional combustion. A short recirculation zone, would mean that also a short combustion chamber could be made, decreasing the its volume. It could therefore be worthwile to choose larger nozzle diameters to decrease pressure losses, save space and weight in a gas turbine. For these experiments, the RZ was always shorter than the combustion chamber length. However, using smaller nozzles / shorter combustion chamber, interference could take place mixing aerodynamic and geometry induced recirculation. The effect of this is unknown, but would be worth investigating in the future.

7.1.2. Jet asymmetry

The asymmetry is larger for larger nozzle diameters. Different mass flows do not have an influence on this, because the behaviour is the same for different velocities at a constant nozzle diameter.The upper jet is thought to be stronger than the lower jet due to the air input of the burnerhead being located on the bottom. Here the air enters into a ring to which all the jets are directly connected. This connection is made with a very sharp transition of a pipe being welded on the bottom of the burnerhead. Because of this the airflow entering this ring inside will disrupt the flow on the bottom, creating a lower pressure here. This is most clearly seen for larger nozzle diameters. When the nozzle diameter decreases, it increases the pressure loss over the jets, increasing the pressure in the ring, decreasing the pressure difference between the top and bottom.

The stronger upper jet will have relatively more entrainment. This means that a larger mass flow will be put into the volume by the upper jet causing this jet to be wider, pushing the downstream part of the aerodynamic centreline and frontal SP down. Stronger entrainment causes a stronger inflow to the upper jet near the burnerhead. This shifts aerodynamic centreline near the burnhead up, also moving the lower SP into the same direction.

7.2. RECIRCULATION, ENTRAINMENT AND REYNOLDS SHEAR STRESS

The main observation from the results on recirculation and what causes this is that it is dependent on jet momentum. Increased jet momentum causes more momentum exchange between the y- and z-direction around the jet (higher Reynolds shear stress). The effect of this is increased entrainment and thus also more recirculation. Since it is dependent on jet momentum, this means that both the jet velocity as well as inlet mass flow have an effect on it. This makes optimisation of the combustion chamber configuration a complex task.

Operation of a gas turbine often includes setting it at different power settings. All of these power settings have a certain air and fuel mass flow. Based on the results seen in this research, one would say that using a smaller nozzle diameter is beneficial for a certain air and fuel mass flow setting. A smaller nozzle diameter will lead to increased momentum for the same mass flow, therefore increasing recirculation and allowing to operate at lower equivalence ratios. The increased Reynolds number this brings about would also increase turbulence in the combustion chamber enhancing mixing of all the gases. This again is beneficial for obtaining FC. However, a smaller nozzle diameter and increased turbulence levels will also bring about higher pressure losses. Too much recirculation could also be harmful if the recirculated heat raises the reactants temperature so much that the temperature in the combustion zone exceeds the thermal NO_x threshold. The increased backflow and more distributed pattern of heat also affects the combustion chamber wall which could result in unwanted increased maintenance or material requirements. There could therefore be an optimum for each mass flow combined with a certain nozzle diameter.

Another way of operating with a certain mass flow with an optimum between recirculation and pressure losses is by changing the number of operational nozzles. When lowering the mass flow, one would perhaps want to decrease the nozzle diameter to keep high recirculation at equal pressure losses. This would be something hard to do during operation, but closing certain nozzles is not. This way one can keep comparable jet momentum with decreasing mass flows. The burnerhead could also feature multiple rings of holes / nozzles, that could be opened or closed with certain mass flow settings.

A stronger central recirculation zone has been shown to increase stability of the FC regime, which is the case for a larger nozzle diameter at equal mass flow. To achieve this strong central recirculation zone for smaller nozzle diameters, one could also put the nozzles radially closer to each other. From the results from this research it would be expected to be beneficial to put smaller nozzle diameter closer to each other. This also increases the available volume for the peripheral recirculation zone to develop. This zone was seen to contribute significantly to the total recirculation. With the increased jet momentum this could show to keep stability while increasing recirculation. This is a design choice worth investigating.

An opportunity that could be seen in future engine designs for FC is the development of inter-turbine combustors and of hybrid distributed propulsion. In an inter-turbine combustor, the flue gases from the first combustion chamber pass through one turbine stage to enter a second combustion chamber. This means that the oxygen concentration is already low and temperatures are high. This way, less recirculation of flue gases is needed within the second combustion chamber, making it easier to achieve FC here. This way pressure losses could be minimised[8]. Hybrid distributed propulsion could be an opportunity, because it uses one centralised gas turbine in the aircraft operating at its design point throughout the flight. This means it requires a much smaller range of operating conditions, making it more suitable for operation in the FC regime.

7.3. CFD MODELLING

The most recommended turbulence models from literature have been investigated to show which one resembles the PIV results best. With the best model it has been tried to model the jet flow most accurately, since this will influence the modelling of the whole flow structure. Without a correct jet modelling, the flow structure inside the combustion chamber cannot be modelled correctly.

7.3.1. TURBULENCE MODEL INVESTIGATION

It was clear from the contour-plots that the standard k-ϵ with c1ϵ = 1.44 model shows the best results with respect to stagnation point accuracy and jet penetration. It performs better than the same model with c1ϵ = 1.6, because increasing this parameter decreases the jet dissipation rate and as such increases its penetration. The increased jet penetration then also influences the RZ shape, causing it to deviate more from the PIV result. Using c1ϵ = 1.3 jet penetration is still overestimated in the beginning, although it gives a wider jet profile to come closer to the PIV results. Afterwards it dissipates too quickly also creating a too short CRZ. This is completely expected since decreasing this parameter increases the dissipation. However, it clearly does not dissipate strongly enough yet in the beginning and too strong in the end, making this model not suited as well.

The Realizable model is supposed to model jet spreading and rotational flows better than the Standard model. For the first part of the chamber it is further behind on the reality than the c1ϵ = 1.44 model, but afterwards predicts stronger jet dissipation (from around z = 100 mm). Perhaps this triggering point can be accelerated and improve the results by decreasing the c2ϵ parameter.

The k-ω SST model shows results completely comparable to the standard k-ϵ with c1ϵ = 1.44 model. This is as expected since it combines the good low Reynolds number performance of the standard k-ω model with the good free stream performance of the k-ϵ model. Since there are not many low Reynolds number regions in the combustion chamber it is expected to produce similar results. It is superior in regions of strong adverse pressure gradients and separation, but these are not present in this case.

The Reynolds Stress Model showed a too far penetration in the beginning and an elongated CRZ. However it predicted a better jet location downstream. The behaviour of the end of the CRZ is more comparable to the PIV results than the other models. It is therefore thought that perhaps with better jet outlet conditions, decreasing the jet penetration, the model has the potential to come close to the PIV results.

It is clear that not one model yet has shown to be the absolute best, since much is still dependent on modelling the jet outlet conditions right. Also, none of the models have been able to capture the flow well and it is thought that perhaps changing from a RANS analysis to an LES analysis would only enable good modelling. The PIV results have shown the flow to be highly unsteady and to have large vortex structures, which are not modelled well by RANS.

7.3.2. BOUNDARY LAYER FIT

As became clear from section 7.3.1, improving the nozzle exit conditions has the first priority in modelling this combustion chamber in CFD. Therefore the exit velocity profile was firstly improved by changing the nozzle length of the model, because it seemed that the boundary layer thickness was behind on the PIV results. The results do show an increase in the maximum velocity obtained in the middle of the profile and this is improved as such using a length of 85 mm. However, the thickness of the boundary does not show any difference. The boundary layer is affected not only by the length of the nozzle, but also by freestream velocity, the near-wall treatment and the roughness of the nozzle wall. The freestream velocity is set per case, and the near-wall treatment was also already shown not to have an influence, it could therefore be tried in the future to change the wall roughness and achieve better results.

Swirl seemed to improve the top-hat behaviour velocity profile from the non-swirl case. Nonetheless, it did not improve the anomaly seen in the width of the velocity profile. This anomaly is something that remains unsolved and perhaps has to do with the turbulence model too.

7.3.3. TURBULENCE INTENSITY INVESTIGATION

With the best results from the nozzle length investigation, the TI at the inlet of the jet has been changed and its development within the jet nozzle has been investigated as well. The PIV results show a factor of 2 higher turbulence levels than the CFD model. The investigation inside the nozzle has shown that within the length of the nozzle, CFD converges to a solution that is too developed. The TI values decrease quickly inside the nozzle and converge to similar levels. These observations explain the similar jet outlet TI conditions for strongly different inlet conditions. It could also be seen that the TI in the center of the jet shows higher TI values for the PIV results, meaning the flow is far from developed. Perhaps increasing the nozzle wall roughness or decreasing the nozzle length to prevend flow development, could improve the results. To conclude, it is thought that this is one of the main reasons for the differences in jet penetration between the different turbulence models and the PIV results.

Something else to take into account is that the PIV TI profile is taken just in front of the nozzle and is not precisely the nozzle exit profile, but it has already interacted with the air in the combustion chamber. However, this should make the TI profile less sharp and as such, the difference between CFD and PIV results would be even larger. It is clear from this investigation that changing this boundary condition alone does not solve the discrepancy between the CFD and PIV results.

7.4. 3D FLOW STRUCTURES

7.4.1. JET INTERACTION & SECONDARY FLOW STRUCTURES

As expected, larger nozzle diameters create stronger jet spreading and will thus merge earlier than smaller nozzle diameters. This also affects the PRZ location, shifting forward or aft together with this merging location. All figures show a difference in starting location of merged jets between the upper and lower jet. This means that the laser sheet was not accurately positioned in between the nozzles. The upper jet is alway stronger the bottom jet by a larger difference than the asymmetry can explain. Therefore, the upper part of the laser sheet must have been a small degree off of the midplane.

7.4.2. RECIRCULATION RATIO

The RR comparison between PIV and CFD shows similarity for the first part, up to around z = 70 mm. After this a major discrepancy can be seen, namely at z = 100 mm. The location matches well with the location of the PRZ, as can be seen in figs. 6.38a to 6.38c, and it is therefore thought to be caused by the PRZ. The PRZ is not captured well by PIV due to the cylindrical distortortion of the outer 7 mm and is therefore not taken into account in the RR calculation. Plane B captures a bit of the PRZ and therefore, when Plane A and B of the PIV results are averaged, a small increase around z = 100 mm can be seen, but this does not account for everything. Just as all previous results have shown, the RR does not differ with changing velocities.

The differences in the two calculation methods, shows that when only using the line in Plane A, the RR is underestimated. The PRZ is much weaker in this plane and is therefore not well represented, whereas the CRZ is well respresented in both planes.

8

Conclusions & Recommendations

8.1. Conclusions

Conclusions that can be drawn from this research are:

- Using the original steel combustion chamber of this setup with quartz glass windows does not allow for optical access of the jet region. The FOV obtained from this is 95 mm in width and 70 mm in height, with 1D as the centrepoint, just capturing the end of the CRZ as such. For investigation of the jet region a fully transparent cylinder has to be used of acrylic or quartz glass for instance.
- The size and shape of the recirculation zone is completely determined aerodynamically by the jet configuration. The jet velocity does not have an influence on this, nor does the combustion chamber length, at least not as long as the end lies beyond the frontal SP. The width of the CRZ is determined by the width of the jet and its spreading, so larger d_{nozzle} causes a narrower CRZ. It also causes a shorter CRZ, because the jets merge more quickly. This potentially creates more stable combustion, but also higher NO_x values, while larger CRZ's create the opposite. A larger nozzle diameter could allow the use of a short combustion chamber, beneficial in terms of volume and weight.
- Reynolds shear stress is quadratically, and entrainment and recirculation are linearly dependent on jet momentum. Increasing either the inlet mass flow or the jet velocity, increases Reynolds shear stress, increasing momentum exchange, increasing entrainment and finally recirculation. For equal mass flows, or power setting, using a smaller nozzle diameter would thus create more recirculation and would therefore be preferred. However, this also increase pressure losses. An optimum nozzle diameter can therefore be sought that balances the right amount of recirculation with the least amount of pressure losses. Changing the nozzle diameter in operation is hard to do, therefore a system closing and opening nozzles could be interesting.
- The PRZ is shown to make a strong contribution to the total amount of recirculated air. It could therefore be beneficial to put nozzles radially closer to each other to increase the strength of this zone. Especially if the central recirculation zone is weak. Thus would thus be a suggestion when operating with smaller nozzle diameters.
- The jet outlet condition is not yet modelled well showing heavily underestimated turbulence levels. It is thought that this is the main reason for the overestimation of jet penetration by the models.
- Of the researched RANS turbulence models, c1ϵ=1.44 of the k-ϵ-model is seen to be superior to c1ϵ=1.3 or 1.6. The k-ω SST model is not thought to improve results. The k-ϵ Realizable model has room for improvement by decreasing the c2ϵ parameter, and the RSM could prove to be accurate using improved nozzle outlet conditions.
- For modelling this setup with CFD, neither the two equation models nor the RSM seem to predict the jet penetration or the turbulence levels well yet. RANS is known not to not to be able to model unsteady and large vortex structures well. Based on this behaviour it could also be the case the

RANS will never model the flow well and one would have to resort to the approach of Large Eddy Simulations (LES).

- The current CFD results do seem to predict the RR well and show that the PRZ has a significant contribution to the RR at their location of over 50%. The PRZ is hard to capture using PIV and it is therefore even more important to create a well validated CFD model to investigate this setup thoroughly.

So to answer the research question:

How can changes in operational variables of the DUT setup improve the applicability of flameless combustion to gas turbines?

This research has indicated that using smaller nozzle diameters increases recirculation, for equal mass flow by increasing jet momentum. The increased flow structure size and feedback of flue gases should improve the chemical mechanism behind reducing NO_x emissions and is therefore beneficial. This will come with extra pressure losses and therefore a different configuration would be optimal for different mass flows. Jet velocity changes or combustion chamber length changes do not have an influence on the applicability.

8.2. RECOMMENDATIONS

Direct recommendations that come from this research focus on the aerodynamics. With respect to experimental investigation, a few recommendations can be made. It would be recommended to perform time-resolved PIV measurements on this system. This will allow for capturing the vortex structures in the shear layer and their development. This creates better insights when setting up and validating the CFD model and give more information to predict what influence of chaning parameters will be for the reactive case. Next to measuring on a plane parallel to the flow, it would be interesting to measure perpendicular to the flow to see how the flow structures are linked. The ultimate experiment would be to perform tomographic PIV, since this creates a full 3D picture of the flow field. However, this is complex to realise and if a validated CFD model can be created this would already give this insight as well.

With respect to the numerical investigation, it is firstly recommended to look into the RANS modelling further. Improving the jet outlet condition has the priority here, concentrating on the outlet velocity profile and the turbulence levels. Changing the latter could be done by changing the wall roughness of the nozzle or decrease the nozzle length to reduce the dissipation time and give a less developed outlet flow. With respect to the different turbulence models, the k-ϵ Realizable model could produce better results using a decreased c2ϵ parameter and the RSM model also seems promising if the jet outlet condition is improved.

If it turns out that RANS is insufficient in modellling this combustion chamber it is recommended to investigate LES. Since this flow is highly unsteady and has large flow structures that can also span for more than the domain that has been modelled now, LES could prove to be necessary for accurate modelling.

A recommendation on the hardware is to modify the burnerhead to take away the asymmetry in the flow. This is now interfering with the results and its influence is also not constant but changes with nozzle diameter. This makes isolation of influences and thus analysis of the results harder. Important in this modification is to ensure a gradual change from the inlet area to the burnerhead volume. it would be best if the input would be centrally placed on the back of the burnerhead. Otherwise a symmetrical placement of an inlet on the other side of the burnerhead would also already improve the symmetry of the nozzle flows.

Once reactive flow can be realised, it is advised to see the influence of the nozzle diameter on the stability and NO_x emissions to see how the CRZ shape and strength and RSS influence this.

BIBLIOGRAPHY

[1] G. J. J. Ruijgrok and D. M. Van Paassen, *Elements of Aircraft Pollution*, 1st ed., edited by M. Schultz, M. Prather, R. Salawitch, and S. Wofsy (Delft University Press, Delft, 2005) p. 381.

[2] M. I. Hegglin, *Figure Q1-2, Twenty Questions and Answers About the Ozone Layer: 2014 Update, Scientific Assessment of Ozone Depletion: 2014, 84 pp.*, Tech. Rep. Report No. 55 (World Meteorological Organization, Geneva, Switzerland, 2015).

[3] S. D. Eastham and S. R. Barrett, *Aviation-attributable ozone as a driver for changes in mortality related to air quality and skin cancer*, Atmospheric Environment **144**, 17 (2016).

[4] A. Gangoli Rao and F. Yin, *A hybrid engine concept for multi-fuel blended wing body, Aircraft Engineering and Aerospace Technology*, **86**, 483 (2014).

[5] A. Wulff and J. Hourmouziadis, *Technology Review of Aeroengine Pollutant Emissions*, Aerospace Science and Technology **1**, 557 (1997).

[6] D. Dewanji, A. G. Rao, M. Pourquie, and J. P. V. Buijitenen, *Investigation of Flow Characteristics in Lean Direct Injection Combustors*, Journal of Propulsion and Power **28**, 181 (2012).

[7] S. Samuelsen, *3.2.1.3-1 Introduction*, in *The Gas Turbine Handbook* (National Energy Technology Laboratory, DOE, Morgantown, WV, 2006) Chap. 3.2.1.3 Ri.

[8] A. A. V. Perpignan, A. Gangoli Rao, and D. J. E. M. Roekaerts, *Flameless Combustion: Towards the application in gas turbines (not yet published)*, (2018).

[9] D. C. Vaz, *Towards the application of flameless combustion to micro gas turbines*, Ph.D. thesis, Universidade Nove de Lisboa (2007).

[10] Y. Levy, V. Sherbaum, and P. Arfi, *Basic thermodynamics of FLOXCOM, the low-NOx gas turbines adiabatic combustor*, Applied Thermal Engineering **24**, 1593 (2004).

[11] Y. Levy, A. G. Rao, and V. Sherbaum, *Preliminary Analysis of a New Methodology for Flameless Combustion in Gas Turbine Combustors*, in *ASME Turbo Expo 2007: Power for Land, Sea and Air*, May (2007).

[12] A. Al-Halbouni, M. Flamme, A. Giese, and M. Brune, *Flameless Oxidation and Continued Staged Air Combustion Systems for Gas Turbines*, International Journal of Energy for a Clean Environment, begell house, inc. **5**, 1 (2004).

[13] L. GmbH, *Product-Manual FlowMaster*, Tech. Rep. (LaVision GmbH, 2016).

[14] M. Raffel, C. Willert, S. T. Wereley, and J. Kompenhans, *Particle Image Velocimetry: A Practical Guide*, 2nd ed. (Springer, Göttingen, 2007) p. 448.

[15] G. Li, E. J. Gutmark, D. Stankovic, N. Overman, M. Cornwell, L. Fuchs, and M. Vladimir, *Experimental study of flameless combustion in gas turbine combustors*, in *ASME Turbo Expo 2006: Power for Land, Sea, and Air*, Vol. 9 (2006) pp. 6619–6633.

[16] F. F. Schrijer and F. Scarano, *Effect of predictor-corrector filtering on the stability and spatial resolution of iterative PIV interrogation*, Experiments in Fluids **45**, 927 (2008).

[17] D. S. Lee, D. W. Fahey, P. M. Forster, P. J. Newton, R. C. N. Wit, L. L. Lim, B. Owen, and R. Sausen, *Aviation and Global Climate Change in the 21st Century*, Atmospheric Environment **43**, 3520 (2009).

[18] P. C. Malte and D. T. Pratt, *Measurement of Atomic Oxygen and Nitrogen Oxides in Jet-Stirred Combustion*, Symposium (International) on Combustion **15**, 1061 (1975).

[19] J. A. Camargo and Á. Alonso, *Ecological and toxicological effects of inorganic nitrogen pollution in aquatic ecosystems: A global assessment*, Environment International **32**, 831 (2006).

[20] K. He, H. Huo, and Q. Zhang, *Urban Air Pollution in China: Current Status, Characteristics, and Progress*, Annual Review of Energy and the Environment **27**, 397 (2002).

[21] H. Johnston, *Reduction of Stratospheric Ozone by Nitrogen Oxide Catalysts from Supersonic Transport Exhaust*, Science **173**, 517 (1971).

[22] M. Gauss, I. S. A. Isaksen, D. S. Lee, and O. A. Søvde, *Impact of aircraft NOx emissions on the atmosphere - Tradeoffs to reduce the impact*, Atmospheric Chemistry and Physics **6**, 1529 (2006).

[23] U. Schumann, *The Impact of Nitrogen Oxides Emissions from Aircraft upon the Atmosphere at Flight Altitudes – Results from the AERONOX Project*, Atmospheric Environment **31**, 1723 (1997).

[24] T. J. Mulder and G. J. J. Ruijgrok, *On the Reduction of NOx-Emission Levels by Performing Low NOx Flights*, in *… of the International Council of the …* (2008) pp. 1–10.

[25] Airbus, *Airbus Global Market Forecast 2016-2035 "Mapping Demand"*, Tech. Rep. (Airbus Group, 2016).

[26] D. C. Vaz, J. P. Van Buijtenen, A. R. J. Borges, and H. Spliethoff, *On the stability range of a cylindrical combustor for operation in the flox regime*, in *ASME Turbo Expo 2004: Power for Land, Sea and Air*, Vol. June (2004) pp. 511–516.

[27] R. Lückerath, W. Meier, and M. Aigner, *FLOX Combustion at High Pressure With Different Fuel Compositions*, Journal of Engineering for Gas Turbines and Power **130** (2008), 10.1115/1.2749280.

[28] C. Duwig, B. Li, Z. S. Li, and M. Aldén, *High Resolution Imaging of Flameless and Distributed Turbulent Combustion*, Combustion and Flame **159**, 306 (2012).

[29] J. A. Miller and C. T. Bowman, *Mechanism and modeling of nitrogen chemistry in combustion*, Progress in Energy and Combustion Science **15**, 287 (1989).

[30] R. Sadanandan, R. Lückerath, W. Meier, and C. Wahl, *Flame Characteristics and Emissions in Flameless Combustion Under Gas Turbine Relevant Conditions*, Journal of Propulsion and Power **27**, 970 (2011).

[31] P. Brimblecombe, *Air Composition and Chemistry*, 2nd ed. (Cambridge University Press, Cambridge, U.K., 1996).

[32] J. Wünning, *Flameless oxidation to reduce thermal no-formation*, Progress in Energy and Combustion Science **23**, 81 (1997).

[33] C. P. Fenimore, *Formation of Nitric Oxide in Premixed Hydrocarbon Flames*, in *13th Symposium (International) on Combustion*, Vol. 13 (1971) pp. 373–380.

[34] D. J. Jacob, *Introduction To Atmospheric Chemistry*, 1st ed., edited by M. Schultz, M. Prather, R. Salawitch, and S. Wofsy, January (Princeton University Press, Princeton, 1999) pp. 1–274.

[35] F. Guethe, M. de la Cruz Garcia, and A. Burdet, *Flue Gas Recirculation in Gas Turbine: Investigation of Combustion Reactivity and NOx emission*, Proceedings of ASME Turbo Expo 2009, June 8-12, 2009, Orlando, Florida, USA , 1 (2009).

[36] G. A. Rao and Y. Levy, *A New Combustion Methodology for Low Emission Gas Turbine Engines*, in *8th HiTACG conference*, July (Poznan, 2010).

[37] M. J. Melo, J. M. M. Sousa, and M. Costa, *Flow and Combustion Characteristics of a Low-NOx Combustor Model for Gas Turbines*, Journal of Propulsion and Power **27** (2011), 10.2514/1.B34033.

[38] Y. Levy, A. G. Rao, and V. Sherbaum, *Chemical Kinetic and Thermodynamics of Flameless Combustion Methodology for Gas Turbine Combustors*, in *43rd AIAA/ASME/SAE/ASEE Joint Propulsion Conference & Exhibit*, July (2007).

[39] A. K. Gupta, *Thermal Characteristics of Gaseous Fuel Flames Using High Temperature Air*, Journal of Engineering for Gas Turbines and Power **126**, 9 (2004).

[40] A. K. Gupta, *Developments in High Temperature Air Combustion (Flameless Oxidation) and Fuel Reforming*, in *44th AIAA Aerospace Sciences Meeting and Exhibit* (2006).

[41] A. Cavaliere and M. de Joannon, *Mild Combustion*, Progress in Energy and Combustion Science **30**, 329 (2004).

[42] C. Duwig, D. Stankovic, L. Fuchs, G. Li, and E. J. Gutmark, *Experimental and numerical study of flameless combustion in a model gas turbine combustor*, Combustion Science and Technology **180**, 279 (2008).

[43] E. Guillou, M. Cornwell, and E. Gutmark, *Application of Flameless Combustion for Gas Turbine Engines*, in *47th AIAA Aerospace Sciences Meeting Including the New Horizons Forum and Aerospace Exhibition* (2009).

[44] A. E. E. Khalil and A. K. Gupta, *Swirling distributed combustion for clean energy conversion in gas turbine applications*, Applied Energy **88**, 3685 (2011).

[45] A. Rebola, M. Costa, and P. J. Coelho, *Experimental Evaluation of the Performance of a Flameless Combustor*, Applied Thermal Engineering **50**, 805 (2013).

[46] A. S. Veríssimo, A. M. A. Rocha, and M. Costa, *Importance of the inlet air velocity on the establishment of flameless combustion in a laboratory combustor*, Experimental Thermal and Fluid Science **44**, 75 (2013).

[47] S. Kruse, B. Kerschgens, L. Berger, E. Varea, and H. Pitsch, *Experimental and Numerical Study of MILD Combustion for Gas Turbine Applications*, Applied Energy **148**, 456 (2015).

[48] I. B. Özdemir and N. Peters, *Characteristics of the reaction zone in a combustor operating at mild combustion*, Experiments in Fluids **30**, 683 (2001).

[49] M. Flamme, *New combustion systems for gas turbines (NGT)*, Applied Thermal Engineering **24**, 1551 (2004).

[50] V. K. Arghode, A. K. Gupta, and K. M. Bryden, *High Intensity Colorless Distributed Combustion for Ultra Low Emissions and Enhanced Performance*, Applied Energy **92**, 822 (2012).

[51] M. Flamme, *Final Technical Report for NGT Project*, Tech. Rep. (2005).

[52] I. E. Idel'chik, *Handbook of Hydraulic Resistance*, 1st ed., edited by D. P. E. Grunaer and I. Staff (Israel Program for Scientific Translations, Moscow, 1960) p. 526.

[53] J. Mi, P. Kalt, G. J. Nathan, and C. Y. Wong, *PIV measurements of a turbulent jet issuing from round sharp-edged plate*, Experiments in Fluids **42**, 625 (2007).

[54] F. Scarano, *Experimental Aerodynamics*, Tech. Rep. First edition (Delft University of Technology, Aerospace Engineering Department - Aerodynamics Section, February 2013).

[55] J. Kompenhans, M. Raffel, L. Dieterle, T. Dewhirst, H. Vollmers, K. Ehrenfried, C. Willert, K. Pengel, C. Kähler, A. Schröder, and O. Ronneberger, *Particle Image Velocimetry in Aerodynamics : Technology and Applications in Wind Tunnels*, Journal of Visualization **2**, 229 (2000).

[56] C. Tropea, A. L. Yarin, and J. F. Foss, *Springer handbook of experimental fluid mechanics*, Vol. 53 (2007) pp. 1043–1080.

[57] L. H. Benedict and R. D. Gould, *Towards better uncertainty estimates for turbulence statistics*, Experiments in Fluids **22**, 129 (1996).

[58] Z. Sun, *Micro Ramps in Supersonic Turbulent Boundary Layers: An experimental and numerical study* (2014).

[59] D. Ragni, F. Schrijer, B. W. Van Oudheusden, and F. Scarano, *Particle tracer response across shocks measured by PIV*, Experiments in Fluids **50**, 53 (2011).

[60] A. Melling, *Tracer particles and seeding for particle image velocimetry*, Measurement Science and Technology **8**, 1406 (1997).

[61] J. D. J. Anderson, *Fundamentals of Aerodynamics*, 5th ed. (McGraw-Hill„ New York, 2011) p. 1098.

[62] S. B. Pope, *Turbulent Flows*, Vol. 125 (Cambridge University Press, Cambridge, U.K., Ithaca, 2001) p. 1361–1362.

[63] B. E. Launder and D. B. Spalding, *Lectures in mathematical models of turbulence [by] B. E. Launder and D. B. Spalding* (Academic Press London, New York, 1972) pp. 7, 169 p.

[64] C. D. Wilcox, *Turbulence Modeling for CFD*, 3rd ed. (DCW Industries Inc., 2006) p. 460.

[65] F. P. Ricou and D. B. Spalding, *Measurements of entrainment by axisymmetrical turbulent jets*, Journal of Fluid Mechanics **11**, 21–32 (1961).

[66] S. B. Pope, *An explanation of the turbulent round-jet/plane-jet anomaly*, *AIAA Journal*, **16**, 279 (1978).

[67] A. P. Morse, *Axisymmetric free shear flows with and without swirl*, Ph.D. thesis, Imperial College (1980).

[68] R. Taghavi and S. Farokhi, *NASA Contractor Report 180895*, Tech. Rep. (The University of Kansas Center for Research, Lawrence, Kansas, 1988).

A

Sketch of the DUT Experimental Setup

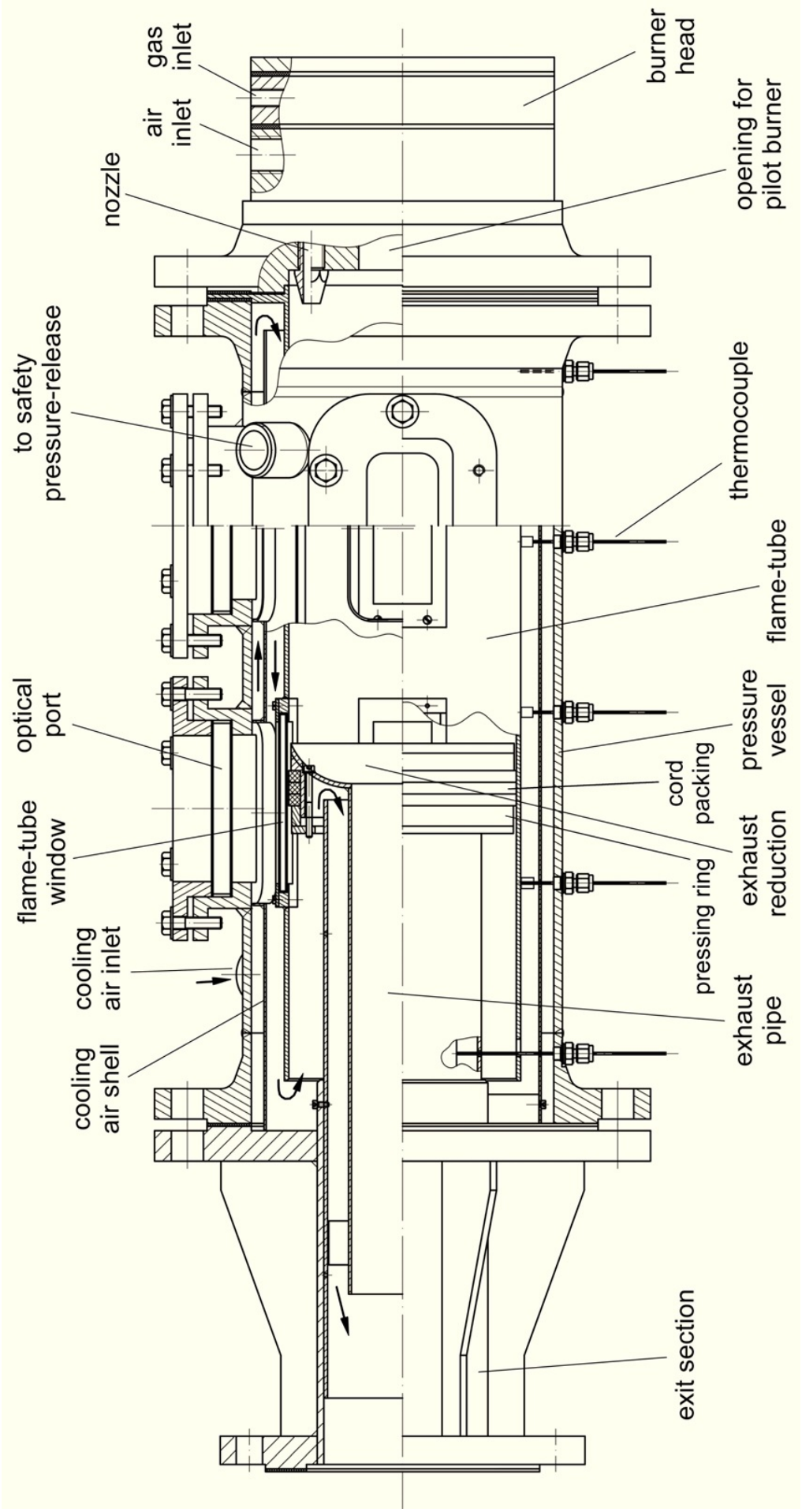

Figure A.1: DUT experimental setup, simplified technical drawing [9]

B

Choice of CFD Solution Method

Table B.1: P-V Scheme solution methods

SIMPLE	SIMPLEC	PISO	COUPLED
Robust solution	Quicker than SIMPLE, can adjust for skewness, less robust	For transient solutions or highly skewed meshes	A little more robust, but much slower

Table B.2: Gradient solution methods

Green-Gauss Cell Based	Green-Gauss Node Based	**Least Squares Cell Based**
Computationally least expensive	Gives best results, specifically when skewed cells are present Least Squares Cell Based is less computationally expensive	

Table B.3: Pressure solution methods

Second Order Upwind	Standard	PRESTO!	Linear Body Force Weighted
May give improvements over Standard	Standard option	When high-swirl/rotating flows are present	When high body forces are present

Table B.4: Momentum, Turbulent Kinetic Energy and Turbulen Dissipation Rate solution methods

First Order Upwind	**Second Order Upwind**	Power Law	QUICK	Third Order MUSCL
High convergence, low accuracy	Less convergence, higher accuracy	Same result as First Order	Both can be interesting for rotating flows	

C

Sensitivity analysis of uncertainty from Pressure and Temperature

Please find a small sensitivity analysis below, showing that errors in these readings do not lead to significant jet speed differences. If pressure has +/- 500 Pa an error of +/- 0.5% can be seen and if temperature has an error of +/- 3 K an error of +/- 1.0% can be seen. Because the readings are assumed to be within these errors, it is estimated that this in itself does not give a significant error.

Table C.1: Sensitivity analysis on the influence of pressure and temperature on the mass flow and jet velocity for minimal nozzle diameter (6.67 mm) and maximum attained mass flow (2980 $lnpm$)

Temperature $[K]$	Pressure $[Pa]$	Mass flow $[lnpm]$	Volume flow $[lpm]$	Jet velocity $[m/s]$	ϵ [%]
275.15	101325	2980	3002	119.3	1
276.15	101325	2980	3013	119.8	0.7
277.15	101325	2980	3024	120.2	0.4
278.15	101325	2980	3035	120.6	0
279.15	101325	2980	3046	121.1	-0.4
280.15	101325	2980	3056	121.5	-0.7
281.15	101325	2980	3067	121.9	-1
278.15	100825	2980	3148	125.1	-0.5
278.15	100925	2980	3145	125.0	-0.4
278.15	101025	2980	3142	124.9	-0.3
278.15	101125	2980	3139	124.8	-0.2
278.15	101225	2980	3136	124.6	-0.1
278.15	101325	2980	3133	124.5	0
278.15	101425	2980	3130	124.4	0.1
278.15	101525	2980	3127	124.3	0.2
278.15	101625	2980	3124	124.2	0.3
278.15	101725	2980	3120	124.0	0.4
278.15	101825	2980	3117	123.9	0.5

D

Pressure Loss of Exhaust Pipe

Using the Darcy-Weisbach equation from the Handbook of Hydraulic Resistance by Idel'chik, the following way has been taken to calculate the pressure loss ΔH inside the exhaust pipe [52]. The Darcy-Weisbach equation can be portrayed by eq. (D.1)

$$\Delta H = \zeta_{sum} \cdot \frac{\gamma \cdot {\omega_o}^2}{2 \cdot g}, \text{ with } \quad \zeta = \lambda \cdot \frac{l}{D_h} \tag{D.1}$$

In these equations, ΔH is the pressure loss, γ the specific gravity, ω_o the mean stream velocity at the inlet, g the gravitational constant and lastly, λ is the friction coefficient of unit relative length and ζ is the total resistance coefficient. The exhaust can then be split up in multiple parts, namely, 2 bends and three straight parts as is shown in appendix D. All parts have a general friction coefficient λ yielding a pressure loss, but the two bends have a local resistance coefficient ζ_{local} and this needs to be calculated seperately using eqs. (D.2), (D.3a), (D.3b) and (D.4).

$$\zeta_{sum} = 2 \cdot \zeta_{local} + \zeta_{bend} + \zeta_{straight} \tag{D.2}$$

$$\zeta_{local} = A \cdot B \cdot C \tag{D.3a}$$

$$A = 1 \text{ for } 90^o \text{ bend}, \quad B = \frac{0.21}{\sqrt{\frac{Re}{D_h}}}, \quad C = 1 \text{ for circular cross-section} \tag{D.3b}$$

$$\zeta_{bend} \text{ or } \zeta_{straight} = \lambda \cdot \frac{l}{D_h} \text{ where } \lambda = 0.027 \tag{D.4}$$

The value for λ and equations for ζ_{local} are both also found in the Handbook of Hydraylic Resitance, for a welded new steel pipe with smooth round corners in a turbulent flow. Using the values of the table below then gives a pressure loss of approximately 90 Pa. For maximum mass flow ΔH is 360 Pa.

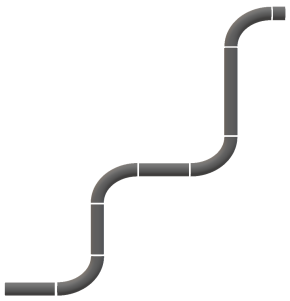

Figure D.1: Schematic drawing of the exhaust pipe of the setup

Quantity	Value	Unit
g	9.81	m/s^2
ρ	1.264	kg/m^3
Re	27050	–
Mass flow	1508	lpm
Total pipe length	7.5	m
Total corner length	0.6	m
Hydraulic diameter	0.11	m
λ	0.027	–

Table D.1: Quantities and values for pressure loss calculation

E

OPTICAL DISTORTION

This appendix gives a clear overview of the optical distortion caused by the acrylic transparent cylinder with a wall thickness of 4 mm, in combination with an f=105 mm lense. It shows that the outer 7 mm is affected by the distortion, but that the distortion is equal horizontally. This is shown by the distortion being similar between the left, middle and right part of the cylinder, displayed in figs. E.1 to E.3.

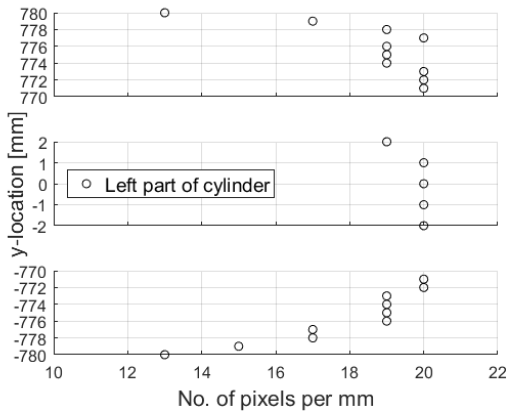

Figure E.1: Optical distortion in the left 10% of the transparent cylinder in number of pixels per mm

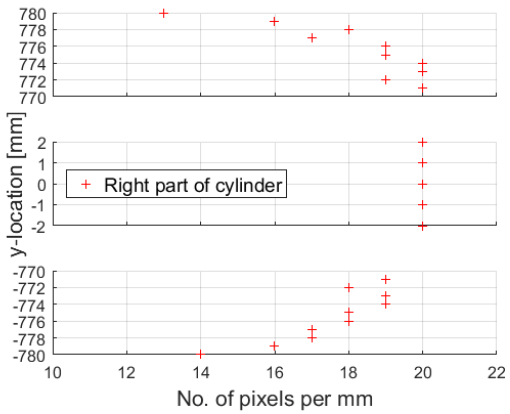

Figure E.2: Optical distortion in the middle of the transparent cylinder in number of pixels per mm

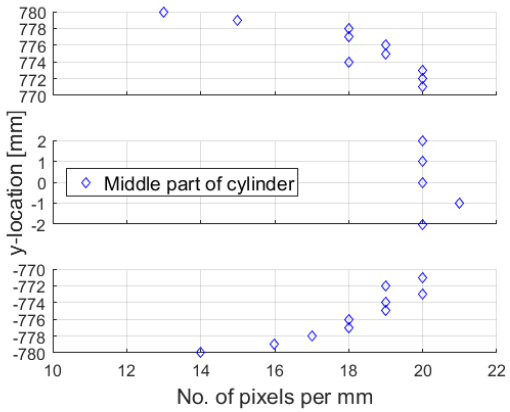

Figure E.3: Optical distortion in the right 10% of the transparent cylinder in number of pixels per mm

F

INVESTIGATION OF THE EFFECTIVE NOZZLE DIAMETER

Table F.1: Overview of the theoretical and effective jet velocities and nozzle diameters

Run	U_{case} $[m/s]$	$d_{theoretical}$ $[mm]$	Volume flow $[lpm]$	$U_{jet,PIV}$ $[m/s]$	$U_{jet,theory}$ $[m/s]$	ΔU	$d_{eff,\Delta}$	d_{eff} $[mm]$
1	15	8.45	511.7	15.8	12.7	24.8%	11.7%	7.46
1	30	8.45	1034.1	32.1	25.6	25.5%	12.0%	7.43
1	45	8.45	1501.6	44.5	37.2	19.8%	9.4%	7.65
1	60	8.45	2083.1	60.2	51.6	16.6%	8.0%	7.78
2	15	8.45	500.5	15.2	12.4	22.3%	10.6%	7.55
2	30	8.45	1026.6	31.1	25.4	22.5%	10.7%	7.55
2	45	8.45	1514.8	45.4	37.5	20.9%	10.0%	7.61
2	60	8.45	2053.1	60.7	50.8	19.4%	9.3%	7.67
2	75	8.45	2547.4	74.1	63.1	17.5%	8.4%	7.74
3	15	6.67	293.1	14.8	11.6	26.7%	12.6%	5.83
3	30	6.67	640.8	31.1	25.5	22.2%	10.5%	5.97
3	45	6.67	934.2	44.7	37.1	20.4%	9.7%	6.02
3	60	6.67	1269.8	59.6	50.5	18.1%	8.7%	6.09
3	75	6.67	1577.9	71.6	62.7	14.1%	6.8%	6.22
3	90	6.67	1902.9	86.3	75.6	14.1%	6.8%	6.21
3	105	6.67	2234.8	100.0	88.8	12.6%	6.1%	6.26
3	120	6.67	2525.6	114.9	100.4	14.4%	7.0%	6.21
3	135	6.67	2807.9	123.1	111.6	10.3%	5.0%	6.34
4	15	11.0	806.3	15.7	11.8	33.6%	15.6%	9.28
4	30	11.0	1692.4	30.9	24.7	25.0%	11.8%	9.70
4	45	11.0	2479.0	45.3	36.2	24.9%	11.8%	9.71
5	15	8.45	503.5	15.2	12.5	21.6%	10.3%	7.58
5	30	8.45	1035.4	31.1	25.6	21.4%	10.2%	7.59
5	45	8.45	1559.7	45.4	38.6	17.4%	8.4%	7.74
5	60	8.45	2000.5	60.7	49.5	22.5%	10.7%	7.55
5	75	8.45	2438.1	74.1	60.4	22.8%	10.8%	7.54
6	15	6.67	291.4	14.8	11.6	27.4%	12.9%	5.81
6	30	6.67	652.0	31.1	25.9	20.1%	9.6%	6.03
6	45	6.67	941.4	44.7	37.4	19.5%	9.3%	6.05
6	60	6.67	1257.1	59.6	50.0	19.3%	9.2%	6.06
6	75	6.67	1545.6	71.6	61.4	16.5%	7.9%	6.14
6	90	6.67	1830.5	86.3	72.8	18.7%	8.9%	6.07
6	105	6.67	2185.6	100.0	86.9	15.1%	7.3%	6.18
7	15	11.0	810.4	15.7	11.8	33.0%	15.3%	9.32
7	30	11.0	1687.1	30.9	24.7	25.4%	12.0%	9.68
7	45	11.0	2516.0	45.3	36.8	23.1%	10.9%	9.80
8	15	8.45	486.0	14.5	12.0	20.2%	9.6%	7.64
8	30	8.45	1033.4	31.5	25.6	23.1%	11.0%	7.52
8	45	8.45	1509.9	43.8	37.4	17.2%	8.3%	7.75
8	60	8.45	2038.1	58.5	50.5	16.0%	7.7%	7.80
8	75	8.45	2533.7	71.1	62.8	13.3%	6.4%	7.91
8	90	8.45	2983.6	81.6	73.9	10.4%	5.1%	8.02